Manganese Dioxides for Oxygen Electrocatalysis in Energy Conversion and Storage Systems over Full pH Range

Mingming Yin[a], He Miao[a,], Ruigan Hu[a], Zixu Sun[b], Hong Li[b,] **

M. Yin[a], Prof. H. Miao[a,] *, R. Hu[a]

[a] Faculty of Maritime and Transportation, Ningbo University, Ningbo 315211, PR China

* Corresponding author:

E-mail: miaohe@nbu.edu.cn (Prof. He Miao)

Dr. Z. Sun[b], Prof. H. Li[b,] *

[b] School of Mechanical and Aerospace Engineering, Nanyang Technological University, Singapore 639798, Singapore

* Corresponding author:

E-mail: ehongli@ntu.edu.sg (Prof. Hong Li)

Abstract:

The oxygen catalytic reactions including the oxygen reduction reaction (ORR) and oxygen evolution reaction (OER) are the basis of many energy transformation and storage devices, e.g., fuel cells, metal-air batteries, and electrolysis cells. Extensive trials have been invested to develop earth-abundant oxygen catalysts to lower the cost and to boost the energy efficiency of these electrochemical devices. Among these oxygen catalysts, manganese dioxide (MnO_2) is attracting ever-increasing interest owing to its high earth-abundance, low cost, and well-balanced activity-stability performances. In this review, the mechanisms of ORR and OER catalysis, methods for activity enhancement, and various applications of MnO_2 oxygen catalysts in energy conversion and storage are summarized and discussed. As the ORR and OER catalysts in the whole pH range, the Mn^{3+} intermediate in MnO_2 is identified as the active center. To optimize the catalytic performance of MnO_2, the strategies of heteroatom doping, morphology tuning, heterostructure forming, conductor supporting, defect engineering, and valence regulating are implemented. Moreover, the applications of MnO_2 in metal-air batteries, fuel cells and water splitting systems are detailed. Lastly, some prospects of MnO_2 oxygen catalysts are proposed for the further development.

Keywords: Manganese dioxides; Oxygen electrocatalysts; Metal-air batteries; Fuel cells; Water splitting

1. Introduction

Recently, the low-cost, efficient, and reliable energy storage and conversion technologies have attracted extensive attentions [1-4]. As the basis of the popular energy storage and conversion technologies such as fuel cells, metal-air batteries and electrolysis cells, oxygen catalytic reactions containing the oxygen reduction reaction (ORR) and oxygen evolution reaction (OER), with favorable thermodynamics and fast kinetics are extremely desirable to lower the overpotential and to decrease Tafel slope, and thus raise the energy efficiency of these electrochemical devices [5-7]. The oxygen catalytic reactions (both ORR and OER) in the whole pH range from alkaline, neutral to acidic are of importance for practical applications. Whereas, there are some basic differences of the ORR or OER reaction mechanisms in the mediums with different pH values.

1.1. ORR mechanisms

ORR in alkaline medium consists of a range of electrochemical reactions involving several electron-transfer steps. In general, the ORR process is completed by either the four-electron transfer pathway or the two-electron transfer pathway (Eq. 2) [8, 9]. In a four-electron pathway, O_2 can be reduced to OH^- directly (Eq. 1). In the two-electron pathway, O_2 is firstly reduced to hydrogen peroxide ions (HO_2^-) in Reaction 2-a followed by Reaction 2-b or by disproportionation of Reaction 2-c. The four-electron transfer pathway is more favourable because of its high energy efficiency. In contrast, the two-electron pathway products the intermediate HO_2^- and increases the overpotential.

$$O_2 + 2H_2O + 4e^- \rightarrow 4OH^- \quad (1)$$

$$O_2 + H_2O + 2e^- \rightarrow HO_2^- + OH^- \quad (2\text{-a})$$

$$HO_2^- + H_2O + 2e^- \rightarrow 3OH^- \quad (2\text{-b})$$

$$2HO_2^- \rightarrow 2OH^- + O_2 \quad (2\text{-c})$$

In acidic and neutral mediums, ORR also could occur through two-electron and four-electron pathways with the same reaction mechanism [10]. In a four-electron pathway, O_2 can be directly reduced to H_2O (Eq. 3). In the two-electron pathway, O_2 is firstly reduced to hydrogen peroxide (H_2O_2) in Reaction 4-a, which is followed by Reaction 4-b or by disproportionation of Reaction 4-c. Similar to ORR in alkaline medium, four-electron transfer pathway is more favourable in acidic and neutral mediums.

$$O_2 + 4H^+ + 4e^- \rightarrow 2H_2O \quad (3)$$

$$O_2 + 2H^+ + 2e^- \rightarrow H_2O_2 \quad (4\text{-a})$$

$$H_2O_2 + 2H^+ + 2e^- \rightarrow 2H_2O \quad (4\text{-b})$$

$$2H_2O_2 \rightarrow 2H_2O + O_2 \quad (4\text{-c})$$

Due to the sluggish intrinsic properties of ORR, the ORR catalysts are indispensable to accelerate the reaction rate. The adsorbate evolution mechanism (AEM) is the conventional catalytic mechanism of the various oxygen catalysts (Fig. 1 a). For the AEM in alkaline conditions, the process includes a $2e^-$ or $4e^-$ pathway. Taking the $4e^-$ pathway as an example, O_2 is first adsorbed on the electrode surface occupied by OH* (* refers to the adsorption site of the catalyst) to form OO*. Then OO* is reduced to OOH* by the combination of protons in solution. Finally, the O–O bond in OOH*

breaks and forms O*, which is then combined with protons to form OH*. During the $4e^-$ pathway, no lattice oxygen directly participates in the formation of the intermediates [11].

Apart from AEM, the lattice-oxygen participated mechanism (LOM) based on the reversible formation of oxygen vacancies (Fig. 1 b) is proposed recently [11]. Generally, LOM is proposed for some special oxygen catalysts in the alkaline media, such as perovskites. LOM indicates that ORR can utilize lattice oxygen in the oxygen catalysts to facilitate the generation of oxygen vacancy and lower activation energy barrier to advantageously form the covalent linkage between oxygen and active sites, thus increasing the oxygen adsorption strength on the catalyst surface [12].

Moreover, dual-site mechanism for ORR is proposed for some oxygen catalysts, such as metal nitrides and hybrid catalysts. Dual-site mechanism is concluded two types: a dual-site $2 \times 2e^-$ ORR mechanism and dual-site cascade ORR mechanism. In acidic medium, for the dual-site $2 \times 2e^-$ mechanism, there are relating two different active sites. HOOH is generated on one site. while on the other site, HOOH reduces to water [13]. For the dual-site cascade mechanism, the first two ORR steps, which generate *OOH and *O intermediates, occur on one site. The generated *O then transfer to adjacent sites driven by cascade adsorption, so that the following reaction steps can take place easily (Fig. 1 c) [14]

1.2. OER mechanisms

OER occurring in different mediums is also a complicated process that consists of several steps. Similar with ORR, OER is also very sluggish, and the OER catalysts are

needed to speed up OER. AEM is frequently used to describe the catalytic mechanism of the OER catalysts. In the alkaline and neutral mediums, OER (Eq. 5) is usually considered to proceed in the following four steps (Eq. 6-a, 6-b, 6-c and 6-d) (Fig. 1 d) [15, 16, 18]:

$$4OH^- \rightarrow O_2 + 2H_2O + 4e^- \quad (5)$$

$$* + OH^- \rightarrow OH^* + e^- \quad (6\text{-a})$$

$$OH^* + OH^- \rightarrow O^* + H_2O + e^- \quad (6\text{-b})$$

$$O^* + OH^- \rightarrow OOH^* + e^- \quad (6\text{-c})$$

$$OOH^* + OH^- \rightarrow O_2 + H_2O + e^- + * \quad (6\text{-d})$$

In the acidic medium, OER (Eq. 7) proceeds in the following four steps (Eq. 8-a, 8-b, 8-c and 8-d):

$$2H_2O \rightarrow O_2 + 4H^+ + 4e^- \quad (7)$$

$$* + 2H_2O \rightarrow OH^* + H_2O + H^+ + e^- \quad (8\text{-a})$$

$$OH^* + H_2O \rightarrow O^* + H_2O + H^+ + e^- \quad (8\text{-b})$$

$$O^* + H_2O \rightarrow OOH^* + H^+ + e^- \quad (8\text{-c})$$

$$OOH^* \rightarrow O_2 + H^+ + e^- + * \quad (8\text{-d})$$

where * refers to active sites on the surface of the catalyst, and the intermediates OH*, O* and OOH* are formed during the four OER steps in the different mediums.

All these four steps are thermodynamically uphill, and the step with the maximum energy barrier is the rate-limiting step of OER. The potential of each step in OER is depending on the binding energies of these intermediates (OH*, O* and OOH*) before and after the charge transfer [17]. To proceed the OH*→ O* (Eq. 6-b or Eq. 8-b) and

O* → OOH* steps (Eq. 6-c or Eq. 8-c), the sum of the required energies is about 3.2 eV. When the energies required in the OH* → O* and O* → OOH* steps are equal, the OER overpotential is smallest. Therefore, the activity of the catalyst is optimized when it can catalyze the OH*→ O* and O* → OOH* steps with similar overpotentials [16].

Activating lattice oxygen can break the key scaling relation of OH* and OOH* intermediates and trigger LOM toward OER [19]. For LOM (Fig. 1 e), two OH* on the metal sites undergo deprotonation, resulting in two metal–oxo species which directly couple to form the O–O bond instead of combining with OH^- to form OOH*. Then, O_2 is released with the two vacant metal centers that are subsequently occupied by OH^-. The OOH* does not appear during the LOM [18]. When the Fermi level is fixed at the top of the O 2p band for highly covalent oxides, the OER on oxygen sites can be triggered, leading to electronic states near the Fermi level with substantial O 2p character, which causes the exchange of electrons with the adsorbates during OER processes [20, 21]. In LOM, the lattice oxygen participation through reversible formation of surface oxygen vacancies is pivotal [22].

In addition, some bimetallic electrocatalysts follow the dual-site mechanism (Fig. 1 f) [19, 23]. In alkaline medium, the dual-site OER mechanism is defined as one or more OER intermediate steps occurring at a given metal site and then transferring to the other metal site for the rest of reaction steps. For instance, *O and *OH intermediates are more easily adsorbed on Fe sites, while the *OOH intermediate prefers the Ni site. Therefore, the first two steps of the OER occur at Fe active site.

When a (Fe)*OOH intermediate forms, it transfers to adjacent Ni site which is the active site for the remaining OER step [23].

1.3. Parameters for ORR and OER

To evaluate and compare the oxygen catalytic properties of different catalysts, well-accepted benchmarking methodologies are required. Herein, some critical parameters for evaluating the oxygen catalysts are summarized as follows.

1.3.1. Potential and overpotential

As is known, the theoretical equilibrium potentials for both ORR and OER are 1.23 V. Therefore, the overpotential (η) is the corresponding potential at a certain current density minus 1.23 V [24]. For ORR, the onset potential and half-wave potential as two crucial potential parameters are usually used to assess and compare the ORR catalytic activities of various oxygen catalysts. The onset potential (E_{onset}) is generally selected at a fixed current density of 0.1 mA cm^{-2} [25]. The half-wave potential ($E_{1/2}$) is the potential corresponding to half of the limiting current density (I_L) [26], where I_L is defined as the maximum current density which is almost unchanged under the negative ORR scanning potential measured in the oxygen saturated solution. For OER, a specific current density of 10 mA cm^{-2} (j=10) is usually adopted for matching the photoelectrochemical water splitting efficiency of 12.3%. Therefore, the potential at a current density of 10 mA cm^{-2} ($E_{j=10}$) is frequently used as a standard to assess the OER catalytic activity of different OER catalysts. Beside $E_{j=10}$, the overpotential at 10 mA cm^{-2} ($\eta_{j=10}$) ($E_{j=10}$ minus 1.23) is also a frequently used parameter to assess the OER catalytic activity. In addition, the OER onset potential (the potential at current density

of 1 mA cm^{-2}) [27] is another important potential parameter. The potential gap between $E_{j=10}$ and $E_{1/2}$ (ΔE) is a crucial parameter to evaluate the bifunctional oxygen catalytic activities toward both ORR and OER, and a smaller ΔE value stands for a better bifunctional oxygen catalytic activity. The above potential parameters can be generally obtained by cyclic voltammetry (CV) or linear sweep voltammetry (LSV).

1.3.2. Tafel slope and exchange current density

Tafel slope is obtained from the Tafel plot (the curve of overpotential versus logarithm value of current density in the LSV curves), and the Tafel plot reflects the electrochemical kinetics correlating an electrochemical reaction rate to the overpotential. Tafel slope is described in the Tafel equation which is an empirical formula and with the mathematical expression of $\eta = \alpha + b \log (j)$, where η denotes overpotential, j represents current density, α is a constant and b is called Tafel slope. Generally, a smaller Tafel slope indicates the faster electrochemical reaction rate and electrocatalytic kinetics. Generally, noble metal catalysts, such as Pt, Ir, Ru-based materials have the smallest Tafel slopes among all oxygen catalysts. For example, the ORR Tafel slope of commercial Pt/C is only 84 mV dec^{-1} in 0.1 M KOH solution [28], and the OER Tafel slope of RuO_2 is as low as 53.5 mV dec^{-1} in 1 M KOH [29].

Exchange current density (j_0) is another pivotal descriptor to estimate the electrocatalytic kinetics, and j_0 is the current density when the overpotential η is zero. In general, j_0 can reflect the charge transfer rate of the oxygen catalytic reaction, and a perfect oxygen catalyst should show a high j_0. j_0 can hardly be measured directly, but it can be calculated from the Tafel equation.

1.3.3. Stability

Stability refers to the change of catalytic activity over time, which can be used to evaluate the ability of oxygen catalysts to maintain their catalytic activity. Two common methods, namely chronoamperometry (CA) and chronopotentiometry (CP), are used to access the stability of oxygen catalysts toward ORR and OER, respectively. CP measures the OER potential versus time at a fixed current density, and the negligible potential change after a long time serves as an evidence of the robust stability. CA measures the ORR current density versus time at a fixed potential, and stability is reflected by the current density loss rate. A smaller current loss rate means a more stable oxygen catalyst toward ORR. Beside CA and CP, cyclic voltammetry (CV) cycling at a somewhat high scan rate is also used to assess the stability of oxygen catalysts. Before and after CV cycling, the potential shifts ($E_{j=10}$ and $E_{1/2}$ are usually used for OER and ORR, respectively.) can be obtained by LSV measurement. A smaller potential shift indicates a better stability toward oxygen catalytic reactions.

1.4. Oxygen catalysts

In fact, both ORR and OER can occur on the carbon electrodes without oxygen catalysts. But both reactions are kinetically sluggish and require very high overpotentials to overcome the energy barriers, resulting in the low energy efficiency. Therefore, it is crucial to obtain effective electrocatalysts to facilitate both ORR and OER by reducing the energy needed to drive these reactions, and then improve the energy efficiencies, dynamic performances and stabilities of fuel cells, metal-air batteries and electrolysis cells [6, 9]. So far, platinum (Pt) and palladium (Pd) are the

most excellent ORR catalysts, and iridium oxide (IrO_2) and ruthenium oxide (RuO_2) are believed to the best OER catalysts [8]. Whereas, the natural scarcity, high cost, and inferior poisoning resistance of these noble metal catalysts limit their commercial applications. Additionally, Pt and Pd exhibit poor OER activity, while IrO_2 and RuO_2 show inferior ORR activity. Therefore, these precious metal catalysts are not able to act as superior bifunctional oxygen catalysts for both OER and ORR, which are essential for rechargeable metal-air batteries and regenerative fuel cells [7, 30]. In these equipments, OER (charging state) and ORR (discharging state) take place in the same electrode, consequently the electrode is identified as “bi-functional”. The catalysts which can accelerate OER and ORR is known as bifunctional oxygen catalysts, that is to say, with catalytic activity for both OER and ORR [30, 31].

To date, extensive efforts have been invested to develop bifunctional oxygen catalysts with high activity, high earth abundance, and low cost; and a series of bifunctional nonprecious catalysts have shown great promise including the nonmetal carbon-based materials [32], metal oxides or hydroxides [33, 34], metal sulfides or phosphides [35, 36], metal or metal-oxide/carbon composites [37] and so on. The bifunctional catalysts of the metal oxides including cobalt oxides, manganese oxides, spinels and perovskites have attracted extensive attentions due to their abundant reserves, affordability, and tunable structures [38]. Despite these advantages of nonprecious metal oxide catalysts, a dilemma of the tradeoff between activity and stability requires intensive effort. Compared with the other 3d metal oxides such as Co_3O_4, NiO and Fe-based oxide, manganese dioxide (MnO_2) has the advantages of

high oxygen storage capacity, rich redox chemistry, self-repairing, and high surface-area utilization owing to different kinds of crystal structures (α-, β- , γ-, σ- and λ-MnO_2) and nanostructures (nanorods, nanowires, nanosheets, nanotubes etc) [39-42]. In addition, MnO_2 can keep stable under low pH [43], which makes it a hopeful candidate for oxygen catalysts in the full pH range. To this end, MnO_2 has received significant interest because of its well-balanced activity-stability performance, diverse crystal structure, and low toxicity.

MnO_2 has been studied extensively as the oxygen catalysts, some reviews on its research progress and applications can be found elsewhere [44-48]. Nevertheless, the catalytic mechanisms and activity origin of MnO_2 have not been clearly defined because it is challenging to detect the reaction intermediates and to benchmark the catalytic performances in the different reports. Additionally, most of these reviews focus on the catalytic activities of MnO_2 in alkaline medium, although MnO_2 can also catalyze ORR and OER in neutral and acidic mediums. In this article, we discuss the recent advances in identifying catalytic mechanisms, developing methods for activity enhancement, and exploring applications of MnO_2 oxygen catalysts in the whole pH range from alkaline, neutral to acidic. Specifically, we will firstly present the crystal structures and catalytic mechanisms of MnO_2 toward ORR/OER in the different mediums. Then, the methods to improve the activity of MnO_2 oxygen catalysts, including heteroatom doping, morphology tuning, heterostructure forming, conductor supporting, defect engineering and valence regulating, are summarized. Moreover, we will emphasize various applications (*e.g.* metal-air batteries, fuel cells and water

splitting) of MnO_2 electrocatalysts in the alkaline, acidic and neutral mediums. Lastly, the challenges and prospects of MnO_2 oxygen catalysts are put forward for further development.

2. MnO_2 Oxygen catalyst

2.1. Microstructures and oxygen catalytic activities

The enrichment of Mn in earth's crust is about 1000 ppm (~0.1 wt%), being the twelfth most earth-abundant element [49]. In addition, as a first-row transition-metal element with five unpaired electrons, Mn is redox-active and exists in several different oxides with distinct crystal forms such as manganese oxyhydroxide (MnOOH), manganese monoxide (MnO), manganese tetroxide (Mn_3O_4), manganese(III) oxide (Mn_2O_3), MnO_2, manganese trioxide (MnO_3), manganese heptoxide (Mn_2O_7), and the new bivalent oxide Mn_5O_8. Associated with a variety of crystal structure, morphology and compositions, manganese oxides (MnO_x) shows a variety of distinct electrochemical properties. Recently, MnO_x have found application in a range of energy storage and conversion devices, such as metal-ion batteries, supercapacitors, metal-air batteries, fuel cells, water electrolyzers [45, 46, 48]. Inspiring by that the $CaMn_4O_x$ cluster is the active centre to catalyze the water oxidization in photosystem II [50], various manganese oxides have been developed as efficient OER catalysts. Also, almost all the manganese oxides exhibit considerable ORR activities [45]. Therefore, MnO_x can act as bifunctional ORR and OER electrocatalysts.

Among various MnO_x, MnO_2 have attracted the most attentions due to its high activity as a bifunctional oxygen catalyst. The oxygen catalytic activity have not been

well understood because of its diverse crystalline structures, morphologies, specific surface areas, electronic structures, manganese valence and defects [44]. Among these factors, the crystalline structures is the most dominant one, which originates from the varying connection modes of the fundamental structure unit ([MnO_6] octahedron, Fig. 2 a), which is composed of Mn^{4+} ions surrounded by six oxygen neighbors. Generally, the crystal structures of MnO_2 can be divided into the following three major categories: 1D tunnel structure (α-, β- and γ-MnO_2), two-dimensional (2D) layered structure (δ-MnO_2), and three-dimensional network structure (λ-MnO_2) [51]. The α-MnO_2 is composed of [MnO_6] octahedron double chains with 2 × 2 tunnels and space group *I4/mmm* (Fig. 2 b). The β-MnO_2 is comprised of [MnO_6] octahedron single chains with [1 × 1] tunnel structure and space group *P42/mnm* (Fig. 2 c). The γ-MnO_2 is constituted of the single and double [MnO_6] octahedron chains with [1 × 2] tunnels and space group *Pmna* (Fig. 2 d). The tunnel structure of α-, β- and γ-MnO_2 can rapidly facilitate the diffusion of O_2, which is beneficial for the oxygen catalytic reaction. The birnessite-type manganese oxide (δ-MnO_2) with the unique lamellar structure consists of Mn octahedral layers in space group *C2/m* (Fig. 2 e). The interlamellar spaces of δ-MnO_2 are always occupied by some heterogeneous atoms (such as the group I cations) to stabilize the layered structure, therefore the valence of some Mn cations in δ-MnO_2 decreases to +3. Generally, the δ-MnO_2 has higher specific surface area than the tunnel α-, β- and γ-MnO_2. The λ-MnO_2 with space group *Fd-3m* shows the cubic phase structure, and the 3-D spinel structure of λ-MnO_2 is favor to intercalate some metal ions, such as Li^+ and Mg^{2+} [52]. The crystalline structure can heavily affect the oxygen

catalytic activity of the different types of MnO_2. For instance, it was reported that the ORR activities of MnO_2 with various crystalline structures in alkaline media followed the order: α-MnO_2 ≈ δ-MnO_2 > γ-MnO_2 > λ-MnO_2 > β-MnO_2 [53]. Whereas, Cheng *et al.* [54] demonstrated that the ORR activity decreases in the sequence of α-MnO_2 > β-MnO_2 > γ-MnO_2. In another report, both OER and ORR activities in alkaline media exhibits a similar structure-determined activity trends following the sequence of α-MnO_2 > amorphous manganese dioxide > β-MnO_2 > δ-MnO_2 [55]. This contradictions among different reports can be ascribed to the different morphologies, specific surface areas, electronic structures, manganese valence and defects of the MnO_2, which can significantly affect the oxygen catalytic activities.

Morphology is another important element that determines the oxygen catalytic activities of MnO_2. It is well known that MnO_2 has a diversity of morphologies, such as nanoballs, nanorods, nanowires, nanotubes, nanoflakes, nanosheets and nanoflowers [54, 56-58]. The ORR catalytic activities of α-MnO_2 with the various morphologies may follow the sequence of nanowire > nanorod > nanotube > nanoparticle > nanoflower [57]. For both OER and ORR activities in the alkaline solution, they were found to follow the sequence of α-MnO_2 nanowires with high crystallinity > α-MnO_2 nanowires with low crystallinity > β-MnO_2 nanorods [58]. In term of oxygen catalytic stability, it was found that α-MnO_2 nanotubes represented much higher ORR stability than α-MnO_2 nanowires or δ-MnO_2 nanosheets [56].

2.2. Oxygen catalytic mechanisms

2.2.1. ORR mechanisms on MnO_2

Although MnO_2 has been investigated intensively as an oxygen catalyst, the catalytic mechanisms still remain uncertain due to the complex chemistry of Mn species, whose evolution can be hardly detected during the reactions. In general, it is commonly believed that both two-electron and four-electron transfer processes occur in the ORR process catalyzed by MnO_2 in alkaline media. The mainstream ORR mechanism on MnO_2 in alkaline medium was summarized as follows [6, 54, 59, 60]. At first, MnO_2 reacts with water (H_2O) and forms the active sites of MnOOH (Eq. 9). Then, the oxygen molecule (O_2) adsorbs onto two (Eq. 10-a) or one (Eq. 10-b) MnOOH, and then is further reduced into OH^- (Eq. 11-a) or HO_2^- (Eq. 11-b), respectively. Eq. 9, 10-a and 11-a indicate the four-electron transfer process of ORR depicted in Eq. 1. Whereas, Eq. 9, 10-b and 11-b indicate the first two-electron transfer reaction process of ORR shown in Eq. 2. In addition, some reports suggest that another four-electron ORR mechanism (Eq. 9, 10-b, 12 and 11-a) could also be realized by optimizing the catalytic activity of MnO_2 toward ORR by, e.g., doping of the low-valence elements such as magnesium, calcium and nickel (Ni) [6, 60].

$$MnO_2 + H_2O + e^- \leftrightarrow MnOOH + OH^- \quad (9)$$

$$2MnOOH + O_2 \leftrightarrow 2(MnOOH\cdots O_{,\,ads}) \quad (10\text{-a})$$

$$2MnOOH + O_2 \leftrightarrow 2MnOOH\cdots O_{2,\,ads} \quad (10\text{-b})$$

$$MnOOH\cdots O_{,\,ads} + e^- \leftrightarrow MnO_2 + OH^- \quad (11\text{-a})$$

$$MnOOH\cdots O_{2,\,ads} + e^- \leftrightarrow MnO_2 + HO_2^- \quad (11\text{-b})$$

$$2MnOOH\cdots O_{2,\,ads} + e^- \leftrightarrow MnOOH\cdots O_{,\,ads} + OH^- + MnO_2 \quad (12)$$

In acidic and neutral mediums, the detail ORR mechanisms on MnO_2 have been

barely reported, but a consensus view is that MnO_2 can accelerate the decomposition of H_2O_2 or HO_2^- [61, 62]. The decomposition of H_2O_2 on the MnO_2 surface follows two processes: (a) chemical regeneration of MnO_x after electro-reduction to Mn^{2+}; (b) chemical disproportionation to O_2 and H_2O on an electrochemically aged manganese oxide surface. The disproportionation reaction of H_2O_2 (Eq. 4-c) can be promoted on the MnO_2 surface, which can be caused by forming certain MnO_x. The possible processes and chemical regenerative reactions are listed in Eq. 13, 14, 15, 16, 17 and 18 [62].

$$MnO_2 + H_2O_2 \rightarrow Mn(OH)_2 + O_2 \quad (13)$$

$$Mn(OH)_2 + H_2O_2 \rightarrow MnO_2 + 2H_2O \quad (14)$$

$$2Mn^{2+} + H_2O_2 + 2H^+ \rightarrow 2Mn^{3+} + 2H_2O \quad (15)$$

$$[Mn(H_2O)_6]^{3+} \leftrightarrow [Mn(H_2O)_5OH]^{2+} + H^+ \quad pKa=0.2 \quad (16)$$

$$[Mn(H_2O)_6]^{2+} \leftrightarrow [Mn(H_2O)_5OH]^{+} + H^+ \quad pKa=10.59 \quad (17)$$

$$[Mn(H_2O)_5OH]^{2+} \rightarrow MnOOH + 2H^+ \quad (18)$$

2.2.2. OER mechanisms on MnO_2

In nature, OER occurs in the green plants, cyanobacteria and algae in the photosystems, which is catalyzed by a $CaMn_4O_5$ cluster center [63]. This inspires the development of the manganese oxides based OER catalysts [64, 65]. The possible mechanisms for OER catalyzed by MnO_2 have been reported, and MnOOH could be the intermediates of the reaction in alkaline medium. As seen from Eq. 19, 20 and 21, the OER mechanism contains the formation of the MnOOH intermediate, which then decomposes to O_2 [55]. Based on this mechanism, the feasible MnO_2-based OER

catalysts should have the advantages of strong adsorption of OH^- group and high charge and ionic transfer rates.

$$MnO_2 + OH^- \leftrightarrow MnOOH\cdots O + e^- \quad (19)$$

$$2(MnOOH\cdots O) \leftrightarrow 2MnOOH + O_2 \quad (20)$$

$$MnOOH + OH^- \leftrightarrow MnO_2 + H_2O + e^- \quad (21)$$

MnO_2 is stable in the full pH range under the appropriate positive potential. Therefore, the OER activity and stability of MnO_2 in neutral and acidic media have drawn intensive attentions. *In situ* OER measurements indicate that Mn^{3+} is formed by electron injection from H_2O to MnO_2, and Mn^{3+} is identified as the active center for OER in the neutral and acidic mediums [66]. The mechanism of MnO_2 catalyzed OER in near-neutral electrolyte is shown in Fig. 3 a [67, 68]. Obviously, the electron injection from water can reduce Mn^{4+} to Mn^{3+}, which undergoes charge disproportionation to form Mn^{4+} and Mn^{2+} ions. The dissolved Mn^{2+} ions become the hydrated Mn^{2+} intermediates, and then undergoes the electrochemical oxidation and deprotonation to form oxygen evolving Mn^{3+} intermediates with the hydroxyl groups. Under low pH, OER catalyzed by MnO_2 was independent of the proton concentrations, and the initial chemical turnover-limiting step corresponded to disproportionation of Mn^{3+} at the catalyst surface (Fig. 3 b) [69]. Whereas, an obvious deterioration of the OER catalytic activity occurred at pH values below 8, and this could be related to that the Mn^{3+} intermediates disproportionate into Mn^{2+} and Mn^{4+} in the form of soluble Mn (II) salts and MnO_2, respectively (Fig. 3 c) [69, 70].

2.3. Improving methods of MnO_2 oxygen catalyst

The oxygen catalytic activities of MnO_2 rely heavily on their preparation methods, and their crystal structures, morphologies, surface chemistries and electronic structures have an important effect on the ORR and OER catalytic activities. The following methods are well regarded to be able to boost the oxygen catalytic activities of MnO_2, and the corresponding electrochemical parameters of ORR and OER were listed in Table 1.

Heteroatom doping: Doping MnO_2 with transition metallic ions such as Ni, iron (Fe) and cobalt (Co) ions can greatly enhance its oxygen catalytic activities [71, 72]. McKendry *et al*. [73] found the OER overpotential at 10 mA cm^{-2} ($\eta_{j=10\ mA/cm^2}$) of Co doped δ-MnO_2 reached 420 mV, being much lower than that in the absence of Co. Zhao *et al*. [74] fabricated ultrathin amorphous cobalt manganese oxide (ACoMnO) nanosheets with a thickness of 0.69 nm by intercalating Co ions into MnO_2. The Co ion intercalation could tailor the structure of A-CoMnO nanosheets at the atomic- and nano-scale, and caused an enhanced OER activity with $\eta_{j=10\ mA/cm^2}$ of 340 mV. In addition, Ni-Fe-doped $K_{0.23}MnO_2$ nanoflowers were prepared by a hydrothermal reaction, and $KNi[Fe(CN)_6]$ (Ni-Fe PBA) nanocubes were in-situ etched by $KMnO_4$ during the reaction [75]. After annealing in argon ambient at 300 ^oC, the defect-rich Ni-Fe-doped $K_{0.23}MnO_2$ cubic nanoflowers (Ni-Fe-$K_{0.23}MnO_2$ CNFs-300) was obtained. This catalyst afforded a low OER overpotential of 270 mV at 10 mA cm^{-2} and a small Tafel slope of 42.3 mV dec^{-1}. Moreover, Zhao et al. [76] synthesized the cobalt ions doped MnO_2 with a great deal of oxygen vacancies *in situ* grown on cobalt and nitrogen co-functionalized carbon nanofibers (Co-MnO_2|O_V). The Co doped MnO_2 with plenty of

oxygen vacancies could decrease the free energy gap and change the OER rate determining step from OH* → O* (pure MnO_2) to the OH* intermediate adsorption (Co-MnO_2|O_V), and then improve the OER kinetics. To reach 10 mA cm^{-2} current density, Co-MnO_2|O_V needed an overpotential of only 279 mV, with Tafel slope of 75 mV dec^{-1}.

Morphology tuning: The oxygen catalytic activities of MnO_2 is also highly dependent on its morphology that determines the activity sites density, specific surface area, charge/ion transportation, and reaction kinetics [77, 78]. Yan *et al*. [79] synthesized the α-MnO_2 nanowires with ultrahigh aspect ratio (>200) via using ionic liquid as the structure-directing agent (Fig. 4 a, b and c). The obtained α-MnO_2 nanowires showed excellent OER activities in alkaline conditions, and the overpotential at the current density of 10 mA cm^{-2} and Tafel slope reached 394 mV and 49 mV dec^{-1}, respectively (Fig. 4 d and e). Zheng *et al*. [80] fabricated two forms of three-dimensional α-MnO_2 (urchin- and dandelion-like) by using two different redox reactions (Fig. 4 f, g, h, i, j and k), and found that the dandelion-like α-MnO_2 had a higher oxygen catalytic activity than urchin-like α-MnO_2, with much lower overpotential (90 mV lower for OER and 20 mV lower for ORR), smaller Tafel slope and higher mass activity (Fig. 4 l, m and n). The more superior activity of dandelion-like α-MnO_2 was due to its fairly larger electrochemical active surface area, higher Mn^{3+} content, more defects and less charge transfer resistance than those in urchin-like α-MnO_2. By using unique solvent free method, the mesoporous α-MnO_2 nanosheets with the layer structure were successfully synthesized, and possessed ultrahigh specific

surface area of 339 m^2 g^{-1} with mesoscale pore size of 6 nm [77]. These α-MnO_2 nanosheets exhibited ORR activity comparable to the commercial Pt/C.

Heterostructure forming: Heterostructured hybrids usually show the enhanced electrical and chemical properties comparing with their individual constituents. Therefore, constructing heterostructures of MnO_2 with other catalysts, *e.g.*, titanium dioxide (TiO_2), nickel oxide (NiO), cobalt oxide (Co_2O_3) and iron oxyhydroxide (FeOOH), has been proved to be a useful tactic to boost oxygen catalytic activities [81-85]. Using first-principles calculations, TiO_2 was demonstrated to be a promising oxide, which can suppress the dissolution of MnO_2 in acidic media at high overpotentials. The electrochemical measurements showed that incorporating TiO_2 into MnO_2 could cause a moderate improvement in stability but only a slight decrease in activity [82]. In addition, Teng *et al* [83] reported a controlled synthesis of ultrathin ferrum manganese oxide hybrid nanosheet via a facile reflux reaction and low-temperature calcination process. The optimized hybrid nanosheet showed a low overpotential of 273 mV at 10 mA cm^{-2}, a small Tafel slope of 63.9 mV dec^{-1}, and excellent durability. The oxygen catalytic activity of this hybrid nanosheet was superior to that of individual MnO_2 and FeOOH. He *et al*. [84] developed an unique NiO/MnO_2 composite by using a facile modifying template strategy. After coating with polyaniline, the catalyst of NiO/MnO_2@PANI delivered superior oxygen catalytic activity and stability. A potential gap of 0.75 V was achieved between 10 mA cm^{-2} for OER and -3 mA cm^{-2} for ORR in the alkaline solution. Fang *et al*. [86] synthesized amorphous metal (oxy)hydroxide on Ni-doped MnO_2 ultrathin nanosheet arrays (ammo@MnO_2) by a

two-step process, including *in-situ* growth of Ni-MnO_2 nanosheet arrays on NF and then a short-term immersion treatment in $FeSO_4$ aqueous solution to deposit amorphous (Ni, Fe) mixed oxyhydroxides on the surface of Ni-MnO_2 nanosheet arrays. The ammo@MnO_2 composite could serve as an efficient OER catalyst with a low $E_{j=10}$ of 232 mV and a small Tafel slope of 36.0 mV dec^{-1} in 1 M KOH.

Conductor supporting: MnO_2 generally has low electric conductivity, therefore depositing MnO_2 nanoparticles on conductive supports, such as carbon materials and nickle foam, can further enhance its oxygen catalytic activity. Among them, MnO_2 deposited on carbon fiber have been reported as a promising oxygen catalyst. Melder *et al*. [87] studied the activity and stability of MnO_2 coated carbon fibre paper (MnO_x/CFP) over a diverse pH range (from pH 1 to 14). At overpotential ranging from 350 to 500 mV, the obtained current densities are all greater than 1 mA cm^{-2} at all pH values, which are decent current densities for the OER catalysts made of earth-abundant elements in the mildly acidic pH regime (pH 2~6). In addition, the current density of 2 mA cm^{-2} could be kept at all measured pHs for at least 24-h successive run, indicating the good stability of MnO_x/CFP. Our group developed a cost-effective oxygen catalyst of MnO_2 nanowires supported on nitrogen-doped reduced graphene oxide (MnO_2/$NRGO_{-Urea}$) by utilizing a simple one-pot approach [88]. The MnO_2/$NRGO_{-Urea}$ showed greatly enhanced ORR and OER activities comparing with MnO_2/C, and the ΔE between $E_{j=10}$ (OER) and $E_{1/2}$ (ORR) is only 0.89 V. Besides carbon materials, the nickel foam was also reported to be employed as an excellent support for MnO_2. Zhao *et al*. [89] developed a novel oxygen catalyst containing two monolayer thick δ-

MnO_2 nanosheet arrays coated on the nickel foam. This catalyst exposed numerous active sites for oxygen catalytic reactions, and thus showed excellent OER activity, attributed to the abundant oxygen vacancies and formation of Mn^{3+} active sites.

Defect engineering: Defects such as oxygen vacancies are well regarded as an excellent active site for oxygen catalytic reaction [90, 91]. Therefore, increasing defects in MnO_2 is an effective strategy to improve its catalytic activity. Applying density functional theory (DFT) calculation, the formation energies of oxygen vacancy in β-MnO_2 were found to be much lower than that of TiO_2 with comparable structures, which suggests easier defect engineering of MnO_2 than TiO_2 [92]. Lee *et al*. [93] reported an efficient ORR electrocatalyst of highly crystalline λ-MnO_2 via the electrochemical removal of lithium from $LiMn_2O_4$. By raising the calcination temperature of $LiMn_2O_4$, the oxygen vacancies were introduced in λ-MnO_2 and the ORR activity was further enhanced. λ-MnO_2 rich of oxygen vacancies exhibited high limited diffusion current density (5.5 mA cm^{-2}) and great transferred electrons numbers (3.8). The oxygen vacancies in α-MnO_2 nanorods could be induced by thermal treatment in air, and increased in density with increasing temperature [59]. The heat-treated sample at 400 °C showed the best ORR activity and stability in alkaline solution, which is ascribed to the moderate oxygen vacancies density as well as coexistence of Mn^{4+} and Mn^{3+} species.

Valence regulating: In MnO_2, Mn^{3+} with single e_g occupation is believed to favor the oxygen catalytic activity of MnO_2 [80, 94]. Therefore, properly increasing the Mn^{3+} content is an available strategy to boost the ORR and OER activities of MnO_2 [95]. A

hybrid catalyst of α-MnO_2 nanotube modified by silver nanoparticles (Ag/MnO_2-3) with large specific surface area and ultrahigh ratio of Mn^{3+}/ Mn^{4+} on the surface was synthesized by Xu *et al*. [96]. The as-synthesized Ag/MnO_2-3 displayed a prominent ORR catalytic activity with very positive onset potential of 0.996 V and half-wave potential of 0.870 V. Gupta e*t al*. [97] researched the OER activity of MnO_2 with various polymorphs to decouple the role of the Mn oxidation state. They found that a lower Mn oxidation state could cause a higher OER activity. Among them, δ/NN_3-MnO_2 (the non-native layered-structure MnO_2 with low stability) was discovered to display the highest specific OER activity because of the lowest Mn oxidation state (+3.5). In δ/NN_3-MnO_2, NN, 3 and δ represent the non-native (NN) structure in MnO_2 polymorphs, stability order of different MnO_2 polymorphs and layered structure of MnO_2, respectively. A novel α-MnO_2 nanowires (MnO_2-$IL_{0.5}$, where IL means the ionic liquid, with the addition of IL, β-MnO_2 nanorods gradually transform to α-MnO_2 nanowires) with high bifunctional oxygen catalytic activity was synthesized with ionic liquid as the structure-directing agent [58]. The prepared MnO_2-$IL_{0.5}$ showed a positive half-wave potential of 0.83 V as well as a low overpotential of only 394 mV at 10 mA cm^{-2}. The excellent OER and ORR activities of MnO_2-$IL_{0.5}$ was ascribed to the high Mn^{3+} content accompanied with the numerous oxygen vacancies. Besides these reports, some important results from the recent works involving MnO_2 or optimized MnO_2 as the oxygen electrocatalysts are also presented in Table 1 [98-119].

3. Applications

Oxygen catalysts play a pivotal role in metal-air batteries (MABs), fuel cells (FCs)

and water splitting systems (WSSs) with aqueous electrolytes. Next, the applications of MnO_2 in the various MABs, FCs and WSSs with different electrolytes will be comprehensively elaborated, as shown in Fig. 5. Specifically, MABs include zinc (Zn)-air batteries (ZABs) with alkaline and neutral electrolytes, aluminum (Al)-air batteries (AABs) with alkaline electrolyte, and magnesium-air batteries (MgABs) with neutral electrolyte. FCs conclude alkaline fuel cells (AFCs) and direct methanol fuel cells (DMFCs) with alkaline electrolytes, microbial fuel cells (MFCs) with neutral electrolyte, and proton exchange membrane fuel cells (PEMFC) with acidic electrolyte. Additionally, WSSs cover the water electrolysis in the alkaline, neutral and acidic electrolytes.

3.1. Metal-air batteries

Lithium-ion batteries (LIBs) have insufficient energy density (< 200 Wh kg^{-1}) for large-scale energy storage [120]. Thus, metal-air batteries (MABs) with high energy density (oxygen from ambient air as the cathode source significantly reduces battery weight.), high safety level (aqueous alkaline or salt electrolytes eliminate the potential danger of combustion or explosion.) and low cost (both cathode source (oxygen) and anode (Mg, Al or Zn) are earth-abundant and cost-effective) have gained great attentions [121]. Nevertheless, MABs also suffer from a series of scientific and technological challenges including sluggish kinetics of cathodic reaction (ORR and OER) and low utilization efficiency of anode, which causes the limited power and energy density [122]. MAB is composed of the metal anode, air electrode, and neutral or alkaline electrolyte. Fundamentally, MABs can be classified into two types based on

the kind of electrolytes. One is aqueous MABs with an aqueous electrolyte (such as ZABs, MgABs and AABs), and the other is organic MABs with an organic electrolyte (lithium-air batteries (LABs) and sodium-air batteries (SABs)) [6, 123, 124].

For aqueous MABs, metals such as Mg, Al and Zn can violently react with acidic solution and evolute hydrogen, resulting in severe anode corrosion. In addition, few oxygen catalysts can remain stable in strongly acidic electrolytes. Therefore, it is believed that the acidic electrolyte is inappropriate for the MABs [123]. Thus, alkaline and neutral electrolytes have been extensively used in MABs. It is noted that both alkaline solutions (such as potassium hydroxide (KOH)) and neutral electrolytes (such as some chloride solutions) can be used in AABs and ZABs, while only neutral electrolyte (such as sodium chloride (NaCl) solution or seawater) can be used in MgABs. Among the various MABs, ZABs are rechargeable, while AABs and MgABs can barely undergo recharge because the electrodeposition of Al or Mg in aqueous solutions is thermodynamically unfeasible. During discharge process (for ZABs, AABs and MgABs), the oxidation reaction takes places on the metal anode, which delivers electrons to the external circuit. Simultaneously, the air cathode accepts the electrons from the anode and ORR occurs. While during the charge process (for ZABs), OER happens at the cathode with metal plating on the anode. The electrode reactions of ZABs, AABs and MgABs are summarized in Table 2. One can see that oxygen catalysts for ORR and OER play a critical role in determining the energy density, power density, and energy efficiency of MABs. MnO_2 has been widely used in MABs as one of the most popular oxygen catalysts. Next, we detailed the MnO_2-based oxygen catalysts in

the aqueous MABs, particularly ZABs, MgABs and AABs.

3.1.1. Metal-air batteries with alkaline electrolyte

3.1.1.1. Zn-air batteries

Owing to its low cost, low negative environmental impact and high theoretical energy density (1086 Wh kg^{-1}), ZABs have been considered as one of the most promising candidates [125]. ZAB comprises a zinc electrode, an air electrode, a membrane separator and alkaline electrolyte [126] (see Table 2 for the electrode reactions). Upon the discharge of ZAB, the oxidation of Zn occurs in the Zn anode, generating the soluble zincate ion $Zn(OH)_4)^{2-}$, which undergoes spontaneous decomposition to form an insoluble zinc oxide (ZnO), while ORR takes place at the air cathode [127]. For rechargeable ZABs, Zn metal plates on the Zn anode while OER takes place at the air electrode during charge of ZAB [128]. The rechargeable ZABs require bifunctional oxygen catalysts with high activity to speed up the sluggish reactions of both ORR and OER [129, 130].

MnO_2 with high ORR but unsatisfactory OER catalytic activity has been used as the oxygen catalyst of primary ZAB in the early work. It was reported that ZABs containing α-MnO_2 and δ-MnO_2 had similar discharge behaviors, but both exhibited better performance than γ-MnO_2, which was ascribed to the higher ORR catalytic activity of α-MnO_2 and δ-MnO_2 than γ-MnO_2 [131]. However, α-MnO_2 and δ-MnO_2 suffered from the low electric conductivity, and thus it is challenging to further improve their oxygen catalytic activities. To improve its electric conductivity, α-MnO_2 was fixed to carbon black powders (XC-72) by the reflux method, and the ORR activity of such

catalysts was optimized when the XC-72/α-MnO_2 ratio is equal to 1 [132]. With such improved ORR catalyst, the ZAB showed a high maximum power density (P_{max}, 67.5 mW cm^{-2}) with the specific capacity of 750 mAh g^{-1} at 1 V under in air ambient. Shortly afterwards, the ORR electrocatalytic activities of α-, β-, γ-, δ-MnO_2 phases mixed with XC-72 were systematically compared in ZAB. The P_{max} of ZAB with α-MnO_2/XC-72 was 102 mW cm^{-2} in oxygen atmosphere, which was the higher than those of ZABs using β-, γ-, and δ-MnO_2 catalysts [133].

Despite many advantages of the rechargeable ZAB, it suffers from short cycling lifetimes, which can be greatly improved by enhancing the stability and bifunctional catalytic activity of oxygen catalysts. Manganese oxide with various valence states and morphologies were synthetized and their catalytic properties were investigated. α-MnO_2 was deemed as one of the best bifunctional oxygen catalyst, and ZAB using the engineered α-MnO_2 catalyst presented a round efficiency of 53% and capacity retention about 95% after 200 charge-discharge cycles over 30 hours [134].

Compared with those comprising MnO_2 coated on carbon paper or carbon cloth, ZAB with MnO_2 directly grown on the carbon paper exhibited the improvement in performance due to the decreased contact resistance (Fig. 6 a, b and c), resulting in P_{max} as high as 108 mW cm^{-2}, and cycling stability up to 500 cycles during continuous discharge-charge tests without replacing the zinc anode or replenishing the electrolyte [135]. To increase the active catalyst load of MnO_2 per unit volume grown on the carbon cloth, while keeping the mechanical and electrical integrity of the air cathode, graphene flakes were coated on the pretreated carbon cloth to form a dense, cross-linked,

and conductive carbon network (Fig. 6 d and e). Flexible ZAB with such air cathode and oxygen catalyst afforded a high P_{max} of 32 mW cm^{-2} and outstanding cycling stability after 110 charge-discharge cycles (Fig. 6 f) [136]. To further improve the bifunctional oxygen catalytic activities, the crystalline structure of MnO_2 grown on carbon cloth (CC) was modulated via thermally driven phase transformation, leading to part of δ-MnO_2 transferring to spinel Mn_3O_4 (Fig. 6 g and h) [137]. The resultant MnO_x-CC showed excellent bifunctional activities comparable to that of Pt/C-RuO_2-CC. More importantly, the flexible ZAB with MnO_x-CC-400 cathode showed low charge-discharge potential and steady operation for 45 h with a round-trip efficiency of 62.4% after 120 cycles (Fig. 6 i).

Although there have been many reports on using MnO_2 as the bifunctional oxygen catalysts, its stability and OER catalytic activity need improvement. Therefore, the air electrode containing MnO_2 ORR catalyst and other efficient OER catalysts is a desirable configuration for rechargeable ZABs. A unique air electrode, carbon paper/α-MnO_2@XC-72/Ti/$Fe_{0.1}Ni_{0.9}Co_2O_4$, in which the α-MnO_2@XC-72 and $Fe_{0.1}Ni_{0.9}Co_2O_4$ exerted the catalytic activities in ORR and OER, respectively, for rechargeable ZABs was successfully demonstrated with P_{max} up to 88.8 mW cm^{-2}, and the voltages between charge and discharge of 0.3 V after 100 charge-discharge cycles in alkaline electrolyte [138]. Similarly, α-MnO_2 film with ORR activity and Co-Fe solid solution layer with OER activity were deposited onto gas-diffusion layer (GDL) substrates step by step to prepare bifunctional oxygen catalysts for rechargeable ZABs. The MnO_x/Co-Fe catalysts showed higher ORR and OER activity than that of MnO_x

or Co-Fe alone, which was ascribed to the reduced Mn oxidation state, low charge transfer resistance and high surface area. A ZAB with MnO_x/Co-Fe catalysts demonstrated high charge-discharge property, excellent stability and cycling efficiency of 59.6% [139].

Doping with hetero cations and hybrid with other oxygen catalysts are also able to improve the OER activity and stability of MnO_2. Fe can offer active redox sites and tolerance towards the oxidative conditions of MnO_2 for ORR and OER. Therefore, to improve the oxygen catalytic activity of α-MnO_2, Fe was doped into the α-MnO_2 nanorods, and significant enhancement in oxygen catalytic activities was observed. The rechargeable ZAB with 0.022FeMn oxygen catalyst displayed superior charge-discharge performance, favorable stability for 3h and high power density [72]. In addition, iron oxides have several oxidation states (such as FeO, Fe_2O_3 and Fe_3O_4) which can be used as the bifunctional catalysts when they are compositing with MnO_x. A novel oxygen catalyst of α-MnO_2 nanotubes-supported Fe_2O_3 nanospheres functionalized with carbon nanotubes ($(Fe_2O_3/MnO_2)_{3/4}$-$(CNTs)_{1/4}$, named FMC) was applied as a robust three-dimensional (3D) clam-shaped bifunctional cathode catalyst for rechargeable ZABs. ZAB assembled with FMC achieved a high P_{max} of 349 mW cm^{-2} and a long cycling life as well [140]. Currently, MnO_2 and cobalt tetraoxide (Co_3O_4) were regarded as the cost-effective ORR and OER catalysts in alkaline electrolytes for ZABs, respectively. A novel Co_3O_4/MnO_2/porous carbon (PQ-7) bifunctional electrocatalysts for aqueous and flexible all-solid-state ZABs were developed and exhibited comparable performances to the commercial 20% Pt/C,

ascribed to tight coupling between Co_3O_4 nanoparticles and MnO_2 nanotubes supported on porous carbon. More importantly, the flexible ZAB based on Co_3O_4/MnO_2/porous carbon air electrodes exhibited a high P_{max} (45 mW cm^{-2}) as well as a long circular life (2.5 h@5 mA cm^{-2}) [85]. So far, significant progress have been achieved on single atom electrocatalysts (SAECs), and MnO_2 with moderate bifunctional activity could be the supports of SAECs. By a facile hydrothermal method, single Ag atoms were incorporated into crystalline α-MnO_2 nanowire (Ag-MnO_2). It was found that Ag not only improved the electrical conductivity of the MnO_2 nanowires by 20 times, but also caused distortions in the MnO_2 crystal lattices and enriched oxygen vacancies, being favorable to bifunctional oxygen electrocatalysis. ZAB with Ag-MnO_2 displayed a high P_{max} of 273.2 mW cm^{-2} and an energy density of 915.4 Wh kg_{Zn}^{-1}, as well as stable operation up to 3200 charge-discharge cycles [141].

3.1.1.2. Al-air batteries

AAB is a promising metal-air battery owing to its high theoretical energy density of 8140 Wh kg^{-1}, much higher than that of lithium-ion battery [142], along with its very negative thermodynamic electrode potential (2.4 V vs. Hg/HgO in alkaline electrolyte), geological abundance, recyclable reaction product of $Al(OH)_3$, and rapid mechanical rechargeability. AABs are primary energy storage systems because the electrodeposition of Al in alkaline electrolyte is not thermodynamically feasible due to its negative standard potential that causes hydrogen evolution before Al deposition [143]. As a non-rechargeable battery, AAB can generate electricity until aluminum anode is consumed in electrolytes and transforms into hydrated aluminum oxide.

Similar to ZAB, AAB includes an Al anode and an air cathode in contact with the aqueous electrolyte, typically KOH solution. The air cathode including GDL, current collector and ORR catalysts is of crucial importance for AABs. The overall anodic reaction of ABB involves the oxidation of Al to aluminate ions, while the cathodic reaction reduce molecular oxygen to hydroxyl ion on air electrode that comprises a porous carbon-based structure to bring oxygen and electrolyte into contact with the ORR catalyst (Table 2). The slow ORR kinetics is a critical limitation of the power density, and thus hinders the practical application of AAB as a power battery. Hence, it is necessary to obtain efficient and cost-effective ORR catalysts to enhance the power density of AAB [144].

Manganese dioxides, especially α-MnO_2 and δ-MnO_2 hold great promise as the nonprecious metal ORR catalysts of AABs. To improve the electrical conductivities of α-MnO_2 and δ-MnO_2, Ag can be employed to form Ag-MnO_2 composite, which can synergistically improve the ORR activity. A 50%Ag-α-MnO_2 composite catalysts, which was composed of Ag nanoparticles anchoring on α-MnO_2 nanorods synthesized by a facile silver ammonia solution reaction, showed much higher ORR catalytic activity than Ag or α-MnO_2 alone. The P_{max} of the AAB with 50%Ag-α-MnO_2 catalyst attained 204 mW cm^{-2} [145]. Besides of α-MnO_2 nanorods, α-MnO_2 nanotubes with the best atomic ratios of Mn^{3+}/Mn^{4+} and highest specific surface (52.9 m^2 g^{-1}) were also employed in the Ag/MnO_2 catalysts. The resultant Ag/MnO_2 catalyst showed superior ORR activities because its nanotube structures facilitate ions diffusion in addition to the synergetic effect between Ag and α-MnO_2. This catalyst guaranteed the AAB with

a high specific capacity of 2835 mA h g^{-1} and a high P_{max} of 77.3 mW cm^{-2} [96].

Another important work incorporated Ag atoms on a plate-like manganese oxide through a metal seed-mediated growth approach [146]. Comparing with the pristine manganese oxide (mixed α-Mn_2O_3 and β-MnO_2), a striped silver manganate structure (SMNp) with a large number of surface dislocations led to increased electron transfer rate and ORR catalytic activity. The aluminum-air flow battery (AAFB) with SMNp exhibited high gravimetric and volumetric energy densities of ~2507 Wh kg_{Al}^{-1} and ~6890 Wh L_{Al}^{-1}, respectively, offering a cost-efficient and safe system for next-generation energy conversion. Doping or intercalating Ag can also improve the ORR catalytic activity of δ-MnO_2. More specifically, 17%Ag-MnO_2/C catalyst (with 17% Ag doping into δ-MnO_2) showed enhanced ORR activity (half-wave potential about 0.8 V,) compared to Ag/C or MnO_2/C alone. Furthermore, the P_{max} of the AAB with 17% Ag-MnO_2/C reached 315 mW cm^{-2} [147]. Besides Ag intercalation, cerium (Ce) ion intercalation could also enhance ORR activity. Among all the Ce intercalated δ-MnO_2 catalysts, 4.8%Ce/MnO_2/C with the knitting-wool-ball-like morphology showed the best ORR activity. The resultant AAB showed the highest P_{max} of 348.8 mW cm^{-2} in a 4 M KOH solution, and the lowest degradation rate of 2% per 100 h [148].

3.1.2. Metal-air batteries with neutral electrolyte

3.1.2.1. Zn-air batteries

For ZABs, KOH has been widely used as the electrolyte as a result of its high ionic conductivity, excellent oxygen diffusion coefficient, low viscosity, as well as fine activity for both Zn anode and air cathode. Unfortunately, KOH electrolyte faces

challenges too. Besides the environmental and corrosion issues, the parasitic formation of carbonates (CO_3^{2-}) can be caused by the absorption of CO_2 from air, which results in the consumption of electrolyte and reduction of electrolyte conductivity. Carbonate will eventually precipitate out and block the pores of the air cathode, which causes the gradual degradation of ZABs. Therefore, the lifetimes of alkaline ZABs and AABs were shorten by several weeks of continuing exposure to air [149]. Thus, replacing the traditional alkaline KOH electrolyte with neutral electrolytes such as zinc chloride ($ZnCl_2$) and ammonium chloride (NH_4Cl) has been considered. Applying chloride-based electrolyte with high conductivity and absence of electrolyte carbonation can effectively extend the cycle life of ZABs. Therefore, for rechargeable ZABs, the near-neutral chloride electrolyte offers a much safer and more robust substitute for the conventional alkaline KOH electrolyte. Whereas, the charge and discharge overpotentials of such ZAB are much higher than those with KOH electrolyte, and the bifunctional oxygen catalysts with high activity in the neutral electrolyte are challenging to be developed.

Manganese oxides are the attractive catalysts among neutral chloride-based electrolyte because of its high selectivity towards OER rather than chlorine evolution reaction [150]. Even so, limited studies on the oxygen catalytic activity of manganese oxides have been carried out in neutral medium. In contrast to α-MnO_2, which is considered as the most promising catalyst among various manganese dioxides for alkaline ZABs, γ-MnO_2 shows great promise for neutral ZAB with chloride-based electrolyte. The air cathode including 20 wt% γ-MnO_2, 70 wt% carbon nanotubes (CNT)

and 10 wt% PTFE exhibited a low discharge-charge cycling stability over 400 h with an overpotential lower than 1.1 V [151]. Comprising near-neutral chloride electrolyte of $ZnCl_2$ or NH_4Cl in the presence of polyethylene and air cathode catalyst of MnO_2 mixing with conductive carbon black, the prototyped ZAB sustained more than 1,000 hours and hundreds of discharge-charge cycles without zinc dendrite and carbonate formation [152]. Notably, neutral ZAB with chloride-based electrolyte and MnO_2 catalyst directly grown on carbon paper air cathode demonstrated excellent cycling stability and satisfactory charge/discharge voltage at low current density, which was due to the suppressed carbon corrosion of air cathode and reduced carbonation of the neutral electrolyte [153]. The performance of neutral ZAB can be further boosted by introducing high-activity oxygen catalysts, and by adjusting the capabilities of neutral electrolyte.

The application of near-neutral chloride electrolytes could effectively enhance the life of ZAB. Whereas, theoretical simulations forecast that such electrolytes are susceptible to other challenges, such as unstable pH and precipitation of mixed zinc hydroxide chloride [149, 154], which should be handled by material and battery design. The thermodynamic analysis showed that the electrolyte composition is complex and sensitive to variation of zinc concentration, pH value, and total chloride concentration. A new kind of framework for modeling the cell-level performance of ZAB with neutral electrolytes confirmed that the electrolyte became strongly acidic during charge/discharge cycling, which was caused by the slow diffusion and low concentration of NH_3 in the electrolyte [149]. Acidic circumstances accelerated the

degradation MnO_2 catalyst, and consequently decreased the lifetime of ZAB.

3.1.2.2. Mg-air batteries

MgABs show high theoretical voltage (3.09 V), specific capacity (2205 mAh g^{-1}), energy density (3910 Wh/kg) in addition to low cost, light weight, environmental friendliness and high earth-abundance [144]. The main components of MgABs are Mg anode, neutral NaCl electrolyte and air cathode. Unlike ZABs and AABs that can use alkaline or neutral electrolyte, MgABs can only use neutral electrolyte such as NaCl, potassium chloride (KCl), ammonium nitrate (NH_4NO_3), potassium bicarbonate ($KHCO_3$), sodium nitrate ($NaNO_3$), sodium sulfate (Na_2SO_4) and magnesium chloride ($MgCl_2$) due to the serious passivation of Mg anode in alkaline electrolyte. Similar to AABs, MgABs cannot be recharged in the aqueous electrolyte due to poor thermodynamics/kinetics performance and insulating properties of magnesium hydroxide [$Mg(OH)_2$] films formed during the discharge process, leading to large overpotential and high polarization [155].

As a primary battery, MgAB generates electricity through redox reaction between Mg and O_2 in air and its electrode reactions are described in Table 2 [156]. The theoretical open cell voltage of MgABs is 3.09 V, but the as-measured values are generally lower than 2 V due to the large polarizations caused by the sluggish cathode reaction and self-corrosion of Mg anode [157]. Also, the practical performances of MgAB, especially power density and energy density are inferior to those of ZAB and AAB. The fundamental scientific challenges for developing high-performance MgABs are threefold: 1) short of efficient and robust ORR electrocatalysts in neutral medium;

2) formation of $Mg(OH)_2$ insulating film that suppresses the anode reaction; and 3) H_2 evolution during Mg self-discharge which causes poor anodic utilization. To solve these vital problems, ORR catalysts with high activity, electrolytes with high ionic conductivity, and Mg anodes with low H_2 evolution rate are needed [158]. Therefore, developing efficient ORR catalysts with high activity and selectivity in neutral medium is crucial for high-performance MgABs.

Various ORR catalysts including MnO_2 have been extensively investigated in MgABs. Among MnO_2 nanorods adsorbed on the different supports (nonsupport, carbon black and multiwall CNT (MWCNT)), MnO_2/MWCNTs showed a parallel, cross and bent intersect structure and high conductivity, which led to the highest ORR activity and stability. The P_{max} of MgAB with MnO_2/MWCNTs reached 70 mW cm^{-2}, much higher than those with MnO_2 or MnO_2/C. Moreover, this MgAB could run for more than 24 h at 20 mA cm^{-2} [159]. Besides the MWCNT support, the hydroxyl carbon nanotubes (CNTs-OH) could not only raise the dispersity of amorphous MnO_2 on its surface but also rivet amorphous particles to CNTs-OH surface firmly. The amorphous MnO_2/CNTs-OH catalyst showed high activity (the half-wave potential was as high as 0.692 V vs. RHE.) and good durability (oxygen reduction current density decreased by 19.69% after 60 h.). Additionally, P_{max} of MgAB with amorphous MnO_2/CNTs-OH reached 79.2 mW cm^{-2}, and the battery can run stably for 15 h at 50 mA cm^{-2} [160].

3.2. Fuel cells

The current combustion-based energy generation technologies rely on the limited and dwindling world supplies of fossil fuels. Even worse, these technologies cause

many global environmental problems, such as greenhouse effect, acidic rains and ozone layer depletion. More environmentally friendly technologies continue to grow in popularity, and fuel cell, as an electrochemical device which transforms the chemical energy in a fuel directly into electrical energy, is one of them [161]. Besides its environment friendliness, fuel cells also offer numerous benefits such as low noise, high power output, and high conversion efficiency. Moreover, fuel cells have good compatibility with renewable sources and modern energy carriers (*i.e*., hydrogen) to achieve sustainable energy development, and inherent modularity nature for simple implementation. Therefore, fuel cells allow a wide field of applications in portable, stationary, and transportation power generation.

Fuel cells can be categorized according to their electrolytes [162]. For different types of fuel cells, their operating temperatures, power outputs, electrical efficiencies and typical applications are distinct. Due to the use oxygen (O_2) as oxidant under discharge mode, the cathode reactions for most of fuel cells are ORR with slight variation in equation (Table 2). Next, we will emphasize the application of MnO_2 as a cost-effective oxygen catalyst for AFCs (in alkaline medium), DMFCs (in alkaline medium), MFCs (in neutral medium), and PEMFC (in acidic medium).

3.2.1. Fuel cells with alkaline electrolyte

3.2.1.1. AFC

As the energy supply devices of the Gemini and Apollo spacecraft, alkaline fuel cells (AFCs) with KOH solution as the electrolyte have shown great success since 1960s [163]. During the working process of AFCs, the conducting ion in the electrolyte

is hydroxyl (OH^-) which moves from cathode to anode, as shown in the electrode reactions in Table 2. One of the major factors preventing the commercialization of AFCs is their alkaline liquid electrolyte. In general, hydroxide ions in the liquid electrolyte can react with carbon dioxide and form metal carbonate, which potentially reduces the concentration of hydroxide ions and blocks the pores of the porous electrode [164]. Also, the air electrode can be flooded or dried if the liquid electrolyte is not governed appropriately. Alkaline anion exchange membrane fuel cells (AAEMFCs) employing AAEM solid electrolyte have received extensive attentions to avoid the application of liquid electrolytes and related issues of carbonation and leakages [165-167]. For both AFCs and AAEMFCs, alkaline electrolyte provides the possibility of enhancing material stability and eliminating the precious metal catalysts.

By combining AFCs with alkaline electrolyzer into one unit, the rechargeable alkaline fuel cell (RAFC) can be developed [168, 169]. RAFC can operate in two different modes, namely the fuel cell mode and electrolyzer mode. In fuel cell mode, RAFCs transform the chemical energy in H_2 and O_2 into electricity, similar to the discharging process of a battery. In electrolyzer mode, RAFCs split H_2O into H_2 and O_2, similar to the charging process of a battery, where electricity is stored in chemical bonds (Table 2), which will be detailed in the following section 3.3. Transition metals or metal oxides that are stable at high pH can serve as stable catalysts with satisfied activity for the fuel cell with alkaline electrolyte [170, 171].

The ORR activity of manganese oxides have been intensively researched in low temperature AFCs [61]. In alkaline medium, the oxygen catalytic activities of various

MnO_2 (α-, β-, δ-MnO_2 and amorphous) depended strongly on their crystal structures and followed the order: α-MnO_2 > amorphous MnO_2 > β-MnO_2 > δ-MnO_2 [55]. For α-MnO_2 with different morphologies, nanowire showed better oxygen catalytic activity than nanotube and nanoparticle [172]. Depositing Ni nanoparticles on α-MnO_2 nanowires and introducing oxygen vacancy in α-MnO_2 nanowires by merely heating it in argon or air ambient could further enhance its oxygen catalytic activity [91]. As mentioned above, amorphous MnO_2 is another promising oxygen catalysts in alkaline electrolyte. A reduced graphene oxide (RGO) supported CoO/amorphous MnO_2 nano-hybrids from Co, Mn-containing layered double hydroxides (Co_3Mn-CO_3-LDH) was synthesized by calcination in nitrogen (N_2) atmosphere. The resultant catalyst exhibited superior ORR catalytic activity and outstanding durability, which was ascribed to the synergistic effect between CoO and amorphous MnO_2, suggesting that this catalyst holds great promise as low-cost oxygen catalyst for AFCs and AAEMFCs [173].

3.2.1.2. Direct methanol fuel cells

DMFCs, which converts chemical energy in liquid methanol fuels to electricity, generates electricity based on the oxidation of methanol (MOR) and ORR at the anode and cathode, respectively [174-176]. The schematic and chemical descriptions of MOR, ORR and overall cell reaction are summarized in Table 2. DMFCs have the advantages of the environmental friendliness and high energy density [177]. However, further improvement of DMFCs is hindered by their high cost (10000~5000 US dollar per kW), unsatisfied reliability, low power density and low energy efficiency (5~15% lower than that of PEMFCs) [174]. One of the main reasons for these disadvantages is that the

state-of-the-art DMFCs use nanostructured precious metals (*i.e.*, Pt or its alloys) as MOR and ORR catalysts [178].

Manganese oxides have been successfully used as both ORR and MOR catalysts, because of their low cost, easy preparation, intrinsic versatility and high methanol tolerance [179-181]. Considering the much higher activity and stability of manganese dioxides in alkaline medium, we emphasize the applications of manganese dioxides as the ORR catalysts of DMFCs with alkaline electrolyte in this section. To improve the activity of MnO_2, conductive carbon supports such as Vulcan XC-72, graphene, carbon nanotubes, and Super P were employed [182]. The birnessite δ-MnO_2 was directly grown on RGO to form a composite catalyst (RGO-MnO_2) by a chelation-mediated aqueous method [183]. The direct growth of δ-MnO_2 on RGO sheets with the excellent conductive network could effectively reduce the contact resistance, as shown in Fig. 7 a, b and c. And δ-MnO_2 clusters and RGO sheets worked synergistically to offer the superior catalytic activities (as seen in Fig. 7 d). Moreover, the oxygen reduction current of RGO/MnO_2 exhibited a decrease with the addition of methanol in the electrolyte, suggesting that RGO/MnO_2 could hardly catalyze the oxidation of the crossover methanol and thus had a high selectivity toward ORR (as seen in Fig. 7 e).

The ORR activities of MnO_2 can also be enhanced by tuning their micromorphology, such as nanowires, nanospheres, and nanoflakes [184]. Microspheres assembled with potassium-doped manganese dioxide (KMO) nanorods were prepared by using a simple template-free, single-step hydrothermal approach [185]. The KMO-100 catalyst exhibited excellent ORR activity in alkaline medium,

and no apparent oxidation peak could be observed when methanol was added in the electrolyte, which suggested that KMO-100 was inert towards MOR and thus had superior methanol tolerance. Moreover, the peak power densities of the DMFC employing KMO-100 as ORR catalyst achieved 43.3 mW cm^{-2} and 153.9 mW cm^{-2} at 25 ^{o}C and 70 ^{o}C, respectively.

As discussed earlier, introducing oxygen vacancies on MnO_2 surface can improve its conductivity and ORR activity [93, 186]. Generally, oxygen vacancies can be introduced on the metal oxides by various methods such as physical plasma engraving, partial reduction by chemical reducing agents, and heat treatment in inert or reducing atmospheres [91, 187, 188]. Oxygen vacancies can also generate on the surface of MnO_2 by high power proton beam irradiation (Fig. 7 f) [189]. Compared to the pristine MnO_2, the proton-beam-irradiated MnO_2 has much more positive half-wave potential ($E_{1/2}$) and higher limiting current (I_L), implying that proton beam irradiation could effectively improve the ORR activity of MnO_2 owing to the formation of numerous oxygen vacancies on MnO_2 surface (Fig. 7 g). When methanol was added to the 0.1 M KOH electrolyte, the ORR current of proton-irradiated MnO_2 was almost maintained, indicating its high resistance to methanol poisoning (Fig. 7 h).

3.2.2. Fuel cells with neutral electrolyte

Similar to traditional fuel cells, the anode of MFCs oxidizes organic substrates and releases electron (by microorganisms as biocatalysts), and the released electrons transport to cathode through an external circuit for ORR (see Table 2 for the electrode reactions of MFCs) [190-194]. The major differences between MFCs and the traditional

low-temperature fuel cells (DMFC and PEMFC) are threefold: 1) utilization of complex biomass and microorganisms as anodic fuel and electrocatalysts, respectively; 2) the working temperature is close to that of ambient environment; and 3) neutral working conditions [195-197]. Currently, MFCs not only can generate electric energy with a highest power density of several W m^{-2} and a cell potential of 0.5~0.8 V, but also have the potential for waste and wastewater treatment [192, 198, 199]. Therefore, MFCs can replace the traditional fossil for the electricity power generation, and then achieve the sustainability of water resources and environment.

Nevertheless, the practical usage of MFCs is still hindered by their low power densities and high costs and maintenance of the reaction cell. A potential avenue to enhance the output power density of MFCs is accelerating ORR occurring at MFC cathode [197]. Therefore, a cost-effective catalyst with high ORR activity is still needed for MFC cathode though Pt-based ORR catalysts are widely used in MFCs at present [200]. As a promising cost-effective ORR catalyst, MnO_2 have been successfully used as the ORR catalysts in MFC. It is well regarded that the particle sizes, crystal structures, synthesis methods, and the supporting materials greatly affect the catalytic activity of MnO_2 used in MFCs. As a useful way to enhance the ORR catalytic activity, MnO_2 can be incorporated into conductive supports, such as carbonaceous materials and conducting polymers.

Two-dimensional graphene, which exhibits large surface area, high electrical conductivity, and superior chemical stability, can be utilized as an excellent carbon support for anchoring/growing different MnO_2 nanostructures [201-203]. It was

reported that the nanoparticles of graphene nanosheet (GNS)-δ-MnO_2 composite synthesized by using a direct redox reaction under microwave irradiation exhibited high ORR activity due to superior electrical conductivity of GNS and unique structure of GNS-MnO_2 composite [201]. The P_{max} of MFC with GNS-MnO_2 catalyst with a loading of 5.0 mg cm^{-2} is 2,084 mW m^{-2}, which is much higher than that of MnO_2 catalyst (1,470 mW m^{-2}), and even higher than that of Pt/C with a loading of 0.5 mg cm^{-2} (1,714 mW m^{-2}). It is well accepted that nitrogen doping in graphene can increase its electrical conductivity [32]. Therefore, the nitrogen-doped graphene can be a promising support for MnO_2 ORR electrocatalyst used in MFC [202]. The α-MnO_2 nanorods supported on nitrogen-doped reduced graphene oxide (MN-NrGO) hybrids were prepared by a simple and feasible hydrothermal method, and MN-NrGO showed excellent ORR activity close to that of Pt/C. The P_{max} of MFCs with MN-NrGO at a very low loading of 0.5 mg cm^{-2} could reach 135.27 mW m^{-2}, suggesting that MN-NrGO electrocatalysts could be an effective and economical cathode catalyst for MFCs. The nanocomposites of manganese oxides and functionalized CNT (f-CNT-MnO_2) exhibited a positive onset potential of 0.11 V, and P_{max} of 520 mW m^{-2} [204].

Conducting polymers, such as polyaniline (PANI), polypyrrole (PPY)-modified MnO_2 nanocomposites have also been studied as effective ORR catalysts. Among various conducting polymers, PANI is deemed as a promising one due to its high electrical conductivity, easy synthesis, good stability and controllable doping chemistry [205, 206]. Ansari *et al*. [205] synthesized the fibrous PANI-MnO_2 nanocomposite by a facile and scalable *in situ* chemical oxidative polymerization method, and the catalytic

activity of this PANI/MnO_2 nanocomposite was studied in a MFC, which exhibited a higher power output than that with pure PANI. Additionally, by using *in situ* chemical oxidative polymerization method, PANI was successfully loaded on the surface of β-MnO_2 nanorods [206]. Thanks to the interaction between β-MnO_2 and PANI that facilitated the electron transfer, the as-synthesized PANI-β-MnO_2 showed much higher ORR activity than β-MnO_2 or mixture of PANI and β-MnO_2. Moreover, the P_{max} of MFC with PANI-β-MnO_2 was 1.4 times as high as that of MFC with β-MnO_2, and the cathode resistance of MFC with PANI-β-MnO_2 was about half of that with β-MnO_2, suggesting that PANI-β-MnO_2 hold great promise as ORR catalyst in MFC applications.

3.2.3. Fuel cells with acidic electrolyte

Among various fuel cells, PEMFC is considered as one of the most attractive one due to its high power density, quiet operation, high efficiency, zero CO_2 emissions, fast start-up, easy scale-up, and low operating temperatures [207, 208]. Therefore, PEMFCs have many potential applications, especially in vehicles, backup power systems, portable devices, and stationary applications [209]. In past decades, PEMFCs have advanced tremendously, and the cruise ranges of electric vehicles powered by PEMFCs have reached 650 km [210]. PEMFC typically possesses a multi-layered architecture, which consists of the anode and cathode bipolar plates, current collector plates, gaskets, and membrane-electrode assembly (MEA) [211].

In PEMFCs, H_2 is oxidized on the anode via hydrogen oxidation reaction (HOR) to release electrons and H^+ (protons), as depicted in Table 2. The electrons can generate electricity at the external circuit, and the protons migrate through the proton exchange

membrane (*i.e.*, the solid electrolyte) and react with oxygen to produce water on the cathode (ORR). The reverse of the electrode reactions (Table 2) to generate hydrogen fuel by water electrolysis is also feasible by using the device called proton exchange membrane electrolysis cell (PEMECs), which was proposed almost at the same period with PEMFCs [212, 213]. The regenerative proton exchange membrane fuel cell (RPEMFC) comprises PEMFC combined with PEMEC into a single system can be considered as an energy storage device like a rechargeable battery with H_2 as the storage medium. As an energy storage device, the round-trip energy conversion efficiency of RPEMFC still needs to be enhanced by optimizing bifunctional catalysts, which can accelerate both ORR during fuel cell mode and OER during electrolyzer mode.

High cost and low durability are the two primary obstacles for PEMFC commercialization [214]. The high cost of PEMFCs mainly comes from use of Pt catalysts, which accounts for about 55% of the PEMFC costs [215]. Moreover, Pt is readily poisoned and poor in OER activity, which causes quick degradation of PEMFCs, and low round-trip energy conversion efficiency of RPEMFCs, respectively. Therefore, one of the important issues of the development of PEMFCs is reducing the loading of Pt catalysts or replacing Pt with nonprecious metals [216]. Among various nonprecious metal catalysts, transition metal and nitrogen co-doped carbons (M-N-C, where M is Fe, Co, or/and Mn) represent one of the most promising ORR catalysts in acidic medium due to their high activity and decent stability [210, 216]. Recently, Pt/C-MnO_2 electrocatalyst, which was synthesized by impregnation chemical reduction utilizing

ethylene glycol as the reducing agent and chloroplatinic acid (H_2PtCl_6) as the Pt precursor, exhibited higher ORR activity and better stability than those of Pt/C alone [217]. According to polarization experiment of a single cell, the power density and durability of the PEMFC were also obviously improved by introduction of MnO_2, indicating that the Pt/C-MnO_2 catalyst can be a substitute of the commercial Pt/C.

Regarding the low durability of PEMFCs, one of the most serious issues is the deterioration of the PEM solid electrolyte, which is attributed to the generation of $HO^{\bullet}$ and $HO_2^{\bullet}$ radicals produced by hydrogen peroxide at the electrode and in electrolyte [218, 219]. Hydrogen peroxide with yield as high as 15% on Pt/C can be generated during the working conditions of PEMFC by the following methods: (a) two electron electrochemical reduction of oxygen on the cathode; and (b) chemical combination of the crossover oxygen and hydrogen on the electrodes. Two methods can be used to minimize the effect of $HO^{\bullet}$ and $HO_2^{\bullet}$ radicals on PEMFC, namely using the dispersed peroxide decomposition catalysts and free radical scavengers. It was reported that MnO_2 can effectively improve the durability of PEM solid electrolyte by serving as both the dispersed peroxide decomposition catalysts and free radical scavengers [218, 219]. The Pt/C-MnO_2 hybrid catalyst prepared by a wet chemical method could be used as an efficient peroxide decomposition catalyst, and introducing 5 wt% MnO_2 into Pt/C (Pt/C-5 wt% MnO_2) could produce 50% less hydrogen peroxide than the pristine Pt/C electrocatalyst [218]. When Pt/C-1 wt% MnO_2 was employed as the ORR catalyst of PEMFC, the percentage of H_2O_2 and concentration of F^- in the anode condensate were reduced by 20~25% and 3~4 times after 24 h operation, respectively. MnO_2 were also

proposed to be the radical scavengers to suppress the degradation of membrane electrode assembly (MEA) in PEMFCs [219]. Introducing MnO_2 as a radical scavenger in the cathode catalyst layer is a valid method that minimize the radical degradation in PEMFCs at open circuit voltage condition. Moreover, single cells with MnO_2 nanotubes and nanowires as the cathode catalysts and radical scavengers showed a P_{max} of 599.3 and 536.8 mW cm^{-2}, respectively, at 75 RH% humidify levels.

Water as the cathodic product of PEMFCs can cause electrode flooding if it is not removed timely and accumulated at the cathode; resulting in oxygen starvation, which may cause the proton (H^+) reduction reaction (PRR) instead of ORR. Wei *et al*. found that the electrochemical reduction of MnO_2 in the composite catalyst of Pt/C-MnO_2 had almost the same potential as ORR [220]. Therefore, in the situation of oxygen starvation, the electrochemical reduction of MnO_2 could serve as a substitute for ORR and limit the voltage reversal effect to a certain extent. In the N_2-saturated sulfuric acid (H_2SO_4) electrolyte, the current density of the Pt/C electrode was too low to be detected, while that of Pt/C-MnO_2 electrode reached 10 mA cm^{-2}. In the situation of oxygen-rich conditions, MnO_2 could also play a synergistic role with Pt/C to improve the ORR activity.

3.3. Water splitting

Hydrogen energy is one of the most ideal substitute for conventional fossil fuels thanks to its high mass energy density and clean nature. Nowadays, hydrogen gas (H_2) is mainly produced by the steam reforming of natural gas that discharges a large amount of CO_2 [221]. The electrochemical splitting of water to hydrogen and oxygen (H_2O →

H_2 + O_2) was discovered in 1800, and it was recognized as one of the most hopeful routes to convert renewable energy (such as wind and solar power) into hydrogen sustainably in the quest for zero carbon emissions [222, 223]. Water splitting composes of two half reactions of hydrogen evolution reaction (HER) and OER. Water splitting reaction is mainly hindered by OER due to its sluggish reaction kinetics associated with the breaking of O-H bond and consequent formation of O=O bond, as well as the four-electron-proton coupled process. Therefore, it is essential to develop effective and stable OER electrocatalysts to enhance the performances of water splitting, particularly in acidic medium (*i.e.*, PEMEC). Presently, iridium/ruthenium oxides are thought to be the best OER electrocatalysts in acidic medium [224]. Whereas, these noble electrocatalysts are costly and scarce, limiting their extensive application in water splitting. Therefore, earth-abundant nonprecious OER electrocatalyst with high activity and stability becomes indispensable for cost-effective and efficient water splitting in acidic medium. To date, most nonprecious OER electrocatalysts can perform well in alkaline medium, but they are unstable in acid medium especially at high potential [224]. In this section, we will emphasize the application of MnO_2 as cost-effective OER catalysts for the alkaline, neutral and acidic water splitting.

3.3.1. Water splitting in alkaline medium

The commercial alkaline water electrolyzer needs an input voltage of 1.8~2.0 V, which are much larger than the theoretical onset voltage of water splitting (1.23 V) [224]. Till now, enormous efforts have been made to discover the HER and OER mechanisms and develop efficient HER and OER electrocatalysts in alkaline medium.

The electrode reactions of water splitting in alkaline medium are summarized in Table 2. It is well accepted that OER, which involves a four-electron transfer process and thereby needs high overpotential to overcome the kinetic energy barriers, is the rate-determining step (RDS) of water splitting [225].

Many earth-abundant materials with high activity, such as metal oxides, carbides, nitrides, chalcogenides and phosphides have been extensively reported [226]. By tuning the morphological features, compositions, and chemical states of these earth-abundant electrocatalysts, highly efficient water splitting with low cell voltage (<1.5 V) and high stability (>500 h) can be achieved [227, 228]. Motivated by the Photosystem II system catalyzed by $CaMn_4O_5$ cluster as the core of its catalytic center, the low-cost and earth-abundant manganese oxides, especially MnO_2 have been deemed as the high-performance and robust catalyst for water splitting [229]. MnO_2 with various phases (α-, β- and δ-phase) show excellent OER activity for water splitting. Comparison of the electrochemical properties of different manganese dioxides as OER catalysts for water splitting in alkaline electrolyte is depicted in Table 1.

Vertically aligned α-MnO_2 nanorods with the diameter of 40~50 nm supported on the surface of functional carbon spheres with a diameter around 1.5 mm (CS-MnO_2) was prepared, and then Pd nanoparticles with diameters of 8~15 nm were dispersed on the surface of α-MnO_2 nanorods (Pd-CS-MnO_2). Pd-CS-MnO_2 showed outstanding OER catalytic activity, owing to the synergistic effect between Pd and α-MnO_2, and to the formation of the OER active centers such as MnOOH-O [230]. Also, cryptomelane-type α-(K)MnO_2 is one of the manganese dioxides with promising OER electrocatalytic

activity for water splitting [231]. The thermal treatment at 300 °C in helium (He) or H_2O/He could make $E_{j=10}$ of α-(K)MnO_2 shift negatively by up to 60 mV. This could be attributed to the three structural features: (1) more Mn^{3+} sites; (2) mono- and dim-oxo bridges; and (3) more structural defects. Simple heat treatment in argon atmosphere could also introduce numerous oxygen defects of rutile-type β-MnO_2 at 350 °C for 2.5 h, and then enhance the OER activity of β-MnO_2 without any modifications by foreign additives [91].

Besides α-MnO_2 and β-MnO_2, layered birnessite type δ-MnO_2 has been investigated for OER catalysts for water splitting. A unique graphene supported MnO_2 nanowire (G/MnO_2 NW) was synthesized by a polymer-mediated self-assembly method in aqueous solution [232]. At 0.7 V (vs. SCE), G-MnO_2 NW produced a current density of 5.9 mA cm^{-2}, being 8.4 times as much as that of Pt/C in alkaline solution, and displayed high turnover frequency (TOF). In addition, extremely thin δ-MnO_2 nanosheet arrays with only 1.4 nm thickness were successfully synthesized via a novel one-step hydrothermal method on the Ni foam surface (denoted as NS-MnO_2, Fig. 8 a, b and c) [89]. NS-MnO_2 with the excellent electrical conductivity exposed numerous Mn^{3+} active sites for electrocatalytic reactions, resulting in high activities and stabilities toward OER (Fig. 8 d, e and f). This could be ascribed to that the δ-MnO_2 nanosheets contained plentiful oxygen vacancies, which resulted in half-metallicity properties and strong H_2O adsorption. This work highlighted the 2D intercalated layer MnO_2 and defect engineering in the optimization of overall water splitting.

Some studies indicated that the interlayer cations also had a significant effect on

OER activity of δ-MnO_2 by providing more active sites, enhancing out-of-plane electrical conductivity and creating geometric frustration [233]. Through a solution phase preparation method, five different alkali cations, *i.e.*, Li^+, Na^+, K^+, rubidium ion (Rb^+), and Caesium ion (Cs^+) were individually incorporated between the 2D-layers of edge-sharing manganese octahedra (MnO_6) nanosheets [234]. The interlayer spacing of nanosheets correlated with the radius of the alkali cations: $Cs^+ > Rb^+ > K^+ > Na^+ > Li^+$. The OER electrocatalytic activities of these δ-MnO_2 catalysts showed a heavy dependence on the intercalated alkali metals, and Cs^+-intercalated nanosheets exhibited the lowest overpotential (η) of 0.45 V, while Li^+-intercalated nanosheets showed the highest η (0.68 V) at a current density of 1 mA cm^{-2}. Intercalation of the first-row transition metal cations (such as Co, Ni and Fe) in the interlayer can also effectively boost the OER activity of δ-MnO_2. The effect on the OER electrocatalytic activity of Co incorporation into δ-MnO_2 was investigated, and it found that the Co: Mn ratio of 1/2 led to the most active catalyst [73]. The OER overpotential ($E_{j=10}$) reached 420 mV, significantly lower than that of δ-MnO_2 in the absence of Co, which was attributed the increase of the valence band edge and occupation of that edge by holes with improved mobility. By intercalating Ni^{2+} ions into the interlayer, the OER activity of δ-MnO_2 could also be enhanced effectively, and $E_{j=10}$ of 7.7 at.% Ni-intercalated δ-MnO_2 was as low as 400 mV [235]. The improved activity in Ni^{2+}-birnessite could be ascribed to the constrained interlayer environment and the resulting improvement in orientational ordering of interlayer water which promoted the redox reactions. The defect-rich Ni-Fe-doped $K_{0.23}MnO_2$ cubic nanoflowers (Ni-Fe-$K_{0.23}MnO_2$ CNFs-300) synthesized by

using a controllable prussian-blue-analogue-sacrificed way followed by annealing (Fig. 8 g, h, i and j) showed one of the best electrocatalytic activities toward OER and HER among the reported manganese oxides catalyst [75]. Benefiting from the abundant defects, unique morphology and doping effect, the overpotentials of Ni-Fe-$K_{0.23}MnO_2$ CNFs-300 for OER and HER were 270 mV and 116 mV at 10 mA cm^{-2} (Fig. 8 k and l), respectively. Moreover, Ni-Fe-$K_{0.23}MnO_2$ CNFs-300 exhibited a very low cell voltage of 1.62 V at 10 mA cm^{-2} (Fig. 8 m) and prominent durability for overall water splitting with a lower cell voltage than that of Pt/C-IrO_2 cell at high current densities.

3.3.2. Water splitting in neutral medium

Water splitting in the ecosystem occurs in the cell sap with pH near neutral [66]. The most abundance water source on earth, seawater with pH around 8 is a naturally available neutral electrolyte [236]. In contrast, no water electrolysis system with neutral electrolyte is commercially available to date. The commercial electrolyzer with alkaline and acidic electrolytes still face challenges such as highly corrosive environments, and lack of earth-abundant OER/HER electrocatalysts and stable membranes [68, 237, 238]. These challenges could be effectively mitigated in neutral electrolyte. The electrode reactions of water splitting in neutral medium are the same as that of the electrolyzer mode of AFCs, where the electrolyte can be some buffer solutions such as phosphate (pH ≈ 7), sulfate (pH ≈ 7), and borate solution (pH ≈ 8.5). However, comparing with alkaline and acidic mediums, the OER and HER kinetics are much slower in a neutral medium due to the larger Ohmic loss and low proton concentration [239]. As a result, much larger voltage is required to accomplish the same current density in neutral

medium.

Since the report of cobalt phosphate deposited on indium tin oxide (ITO) electrode with a moderate overpotential and high TOF for OER in near neutral solution [240], extensive effort has been put into the earth-abundant OER electrocatalysts for neutral medium. Among them, manganese oxide catalysts such as Mn_3O_4 [241-243], Mn_2O_3 [241], MnO [244, 245], Mn_5O_8 [246] and MnO_2 [70] have received considerable interest. By *in situ* UV-vis absorption spectroscopy, the water oxidation mechanism of MnO_2 was studied at various pH values, suggesting that Mn^{3+} species on the surface of MnO_2 electrocatalyst induced by water oxidation showed a different coordination environment at different pH [67]. Formation of deprotonated Mn^{3+} free from charge disproportionation was important for efficient manganese oxide OER electrocatalysts at neutral pH. Whereas, Mn^{3+} was unstable at low pH (< 9) due to the disproportionation reaction (Mn^{3+} — Mn^{2+} + Mn^{4+}) [247]. Consequently, the low OER activity of MnO_2 for water splitting under neutral mediums could be due to the inherent instability of Mn^{3+}. Therefore, controlling the disproportionation reaction of Mn^{3+} is crucial for the development of MnO_2 OER electrocatalysts at neutral pH.

The surface modification of δ-MnO_2 with poly(allylamine hydrochloride) (PAH) was found to be an effective method to suppress the disproportionation reaction of Mn^{3+}, thanks to the formation of N-Mn bonds through the coordination of amine groups of PAH to the Mn sites of δ-MnO_2 [70]. This method caused the OER onset potential shift negatively as large as about 500 mV at neutral pH. Generally, the generation and accumulation of Mn^{3+} at the surface of MnO_2 can be related to the electrochemical

oxidation of Mn^{2+} [247]. As a critical factor of the efficient energy conversion by photosystem II, the concerted proton-electron transfer (PCET) could promote the electrooxidation of Mn^{2+} to Mn^{3+}. It was reported that pyridine and its derivatives with pKa values between the water ligand bound to Mn (II) and Mn (III) could be used as PCET [248]. The regulation of pyridine and its derivatives as PCET was a useful way to improve the OER activity of α-MnO_2 at neutral pH. Additionally, δ-MnO_2 nanostructures directly synthesized on pristine graphene (G-MnO_2 NW) showed much more significant improvement of the OER activity compared to commercial Pt/C in neutral medium, and the TOF value of G-MnO_2 NW was as high as 0.0073 S^{-1} at 0.73 V vs. SCE in neutral solution [232].

3.3.3. Water splitting in acidic medium

Comparing with neutral and alkaline electrolytes, electrocatalysts in acidic electrolytes can accelerate HER and OER much more efficiently, and reduce the overpotential of the two half-cell reactions significantly [249]. PEM water electrolyzer (PEMWE) employing fast H^+ conducting polymers (such as Nafion film) has been intensively studied due to its low gas crossover, high current density, high voltage efficiency and effective operational costs [66, 250]. Additionally, a rapid system response of the PEM electrolyzer is of great advantage for employing the intermittent renewable energies storage, such as the wind and solar power. Whereas, both cell and catalysts in the acidic water splitting systems require acidic corrosion-resistant materials.

The electrode reactions of water splitting in acidic medium are same as those of

the electrolyzer mode of PEMFCs, as summarized in Table 2. During operation, water decomposes into electrons, protons and oxygen gas on the anode, then the protons passes through the polymer electrolyte and transports to the cathode compartment. While the generated electrons travels from anode to cathode along the external circuit, they combine with the protons into hydrogen gas on the cathode [66]. HER rate is high in acidic electrolyte due to the favorable conversion of a proton to hydrogen gas [251, 252]. An electrical potential >1.8 V is usually required for overcoming the sluggish OER kinetics to obtain the operational current density ~2.0 A cm^{-2} [250]. Therefore, it is considerable to develop efficient OER catalysts for higher energy efficiency. Whereas, stable noble-metal-free electrocatalysts for OER in acidic electrolytes are very scarce, and only some noble-metal oxides such as IrO_2 and RuO_2 are efficient acidic OER catalysts [253]. Therefore, the lack of cheap substitutes for noble-metal oxides is the main bottleneck in the acidic water electrolysis.

As the low-cost OER catalyst, most of transition metal oxides tend to dissolve in strongly acidic solutions especially at a high potential, which is detrimental for developing reliable acidic OER catalysts. Although the OER activities of manganese oxides are not as high as the late first-row transition metal oxides, such as Co and Ni oxides/ hydroxide, manganese oxides are the few noble-metal-free catalysts that are moderately stable at acid OER conditions [254], thanks to their increased inertness and self-healing ability in acidic solutions [255]. It was suggested that an initial chemical turnover-limiting step could be assigned to surface Mn^{3+} disproportionation in acidic mediums, which could be inferred from a quasi-infinite Tafel slope and lack of proton

dependence [255]. Also, Mn^{3+} was stabilized kinetically in tetrahedral sites and its presence strained the oxide lattice, causing a favorable distribution of oxide based vs. metal-based energy levels that favored the OER activity [95]. Therefore, the OER activity of manganese oxides could be greatly improved by the introduction of Mn^{3+}. Mn^{3+} could be introduced into MnO_2 by an electrochemically induced comproportionation reaction with Mn^{2+} in acidic solution [95].

Electrodeposited manganese oxide film is one of the promising acidic OER catalysts. OER activity of electrodeposited MnO_2 films could be improved by changing the deposition protocol from a constant anodic potential to a voltage cycling routine (alternating between positive and negative potentials) [256]. After voltage cycling activation, the Tafel slope of manganese oxide decreased from 650 to 90 mV/decade in acidic solutions, and the current density of the activated manganese oxide film at overpotential of 600 mV was about 2 orders of magnitude higher than that of the original sample, approaching that of RuO_2 and IrO_2. This was attributed to the original birnessite-like δ-MnO_2 transformed to hausmannite-like intermediate (α-Mn_3O_4) by comproportionation with cathodically generated $Mn(OH)_2$, and then the anodic conditioning from voltage cycling or water oxidation synthesized a disordered δ-MnO_2 phase, which was highly active for oxygen evolution in acid medium. Besides the poor OER catalytic activity, the inferior stability of MnO_2 in acid is another big challenge. The overpotential of the electrodeposited δ-MnO_2 obviously increased in a short time under a low current density (< 1 mA cm^{-2}) [255]. The stability of MnO_2 could be greatly improved just by controlling the potential windows in which OER can be catalyzed

efficiently without the corrosion of MnO_2 [257]. γ-MnO_2 prepared by thermal decomposition of manganese nitrate in air at 220 ºC has a stable potential window (1.6~1.75 V), where γ-MnO_2 can catalyze OER at 10 mA cm^{-2} for over 8,000 h in acidic electrolyte (pH = 2) without noticeable degradation.

To enhance the activated MnO_x, a design principle that could introduce various co-interacting metals to fulfill specific roles was proposed. Mixed metal oxides ($CoMnO_x$) had been constructed with Co and Mn as the catalytic and stable metals, respectively, and $CoMnO_x$ showed similar OER activity to cobalt oxide (CoO_x) with Tafel slopes of about 83 mV dec^{-1} in acidic acid (pH = 2.5) [258]. $CoMnO_x$ kept intact and stable during continuous operation for over 12 h, while CoO_x fully dissolved in the acid electrolyte within only 3 h when it worked at 0.1 mA cm^{-2}. Inspired by natural OER catalyst of Mn_4CaO_5 complex, a nano-layered manganese calcium oxides (Ca-Mn-O) were developed and showed a low overpotential for water splitting in acid medium [259]. The exchange current density of Ca-Mn-O was about one order of magnitude higher than that of the bare glassy carbon (GC) electrode and slightly lower than that of Pt.

Hybridizing with other metal oxides is another effective method to improve the OER activity and stability of MnO_2. The anodic dissolution of MnO_2 in acidic medium proceeds by the formation of higher oxide of MnO_4^-, and the dissolution of undercoordinated sites of MnO_2 is favored over the dissolution of active OER terrace sites. Using DFT calculations, it was found that TiO_2-terminated MnO_2 could improve the stability of MnO_2 because the undercoordinated sites were successfully covered

with TiO_2 [82]. Then, this prediction was experimentally verified by investigating the OER activities and stabilities of the sputter-deposited MnO_2 and Ti-MnO_2 films. The results demonstrated that small amounts of TiO_2 incorporated into MnO_2 caused an obvious improvement of the OER stability, with only a slight decrease in activity. MnO_2 was also found application in splitting acidic saline water, where the competition between OER and chlorine evolution reaction (CER) is very important. Using diffusion barriers is an effective method to improve the selectivity of OER and CER. It was found that the deposition of MnO_x film on the glassy carbon-supported IrO_x obviously decreased the CER catalytic activity and then shifted the selectivity from CER to OER [254]. As a diffusion barrier, the deposited MnO_x layer was catalytically inactive toward CER, and could prevented Cl^- from reacting on the IrO_x catalyst underneath. But the deposited MnO_x layer still could facilitate the transport of protons, O_2 and water between the IrO_x catalyst and electrolyte that was indispensable for OER.

4. Summary and outlook

To improve the energy efficiency of fuel cells, metal-air batteries and electrolysis cells, oxygen catalytic reactions (ORR and OER) with fast kinetics are highly desirable. Therefore, developing efficient and inexpensive oxygen catalysts is one of the most crucial challenges for these energy storage and conversion technologies. Among the various oxygen catalysts, MnO_2 has attracted significant interest owing to its high earth abundance, low cost, low toxicity, diverse crystal structure and well-balanced activity-stability in the full pH range. Whereas, MnO_2 suffers from the low electric conductivity, unsatisfactory OER catalytic activity and stability, and thus numerous works have

focused on the development and improvement of MnO_2 or MnO_2-based oxygen catalysts. This review primarily introduced the catalytic mechanisms, improving methods, and applications of MnO_2 oxygen catalysts in the alkaline, neutral and acidic mediums. Firstly, the crystal structures and morphologies of MnO_2 were introduced, and the relations between the microstructures and oxygen catalytic activity of MnO_2 were summarized, and α- and δ-MnO_2 with high specific surface showed high catalytic activity. The catalytic mechanisms of MnO_2 toward ORR and OER in different mediums were discussed, and the intermediate of Mn^{3+} was believed to facilitate the oxygen catalytic activity of MnO_2. In addition, the oxygen catalytic activity of MnO_2 is greatly dependent on their crystal structures, morphologies, surface chemistries, and electronic structures. We summarized the major improving methods of MnO_2 oxygen catalysts in different mediums such as heteroatom doping, morphology tuning, heterostructure forming, conductor supporting, defect engineering and valence regulating. All these methods could effectively improve the oxygen catalytic activity, and the mechanisms were usually composed of multiple factors. At last, the recent application status of MnO_2 oxygen catalysts in metal-air batteries (alkaline and neutral electrolytes), fuel cells (alkaline, neutral and acidic electrolytes) and water splitting systems (alkaline, neutral and acidic electrolytes) were introduced. The optimized MnO_2 with high activity and stability can be successfully used as a promising cost-effective oxygen catalyst in the MABs, FCs and WSSs over full pH range.

Although great achievement of MnO_2 oxygen catalysts has been made to date, there was still far to go towards its practical applications in the fields of metal-air

batteries, fuel cells and water splitting systems. Accordingly, we propose the prospects as follows.

(1) The ORR and OER catalytic mechanisms of MnO_2, particularly in neutral and acidic electrolytes, should be further clarified by detecting the intermediates with *in situ*/operando characterization tools. Then, the active sites for oxygen catalysis of MnO_2 can be identified, which can guide the reasonable design and development of MnO_2 oxygen catalytic catalysts with the improved activity and stability.

(2) The correlations between oxygen catalytic properties and structure or morphology of MnO_2 should be further clarified, which is beneficial for optimizing and designing the MnO_2-based oxygen catalysts. Though some works attempt to discover these correlations, but ambiguous conclusions even contradictions among different reports still exist, which can be ascribed to the different morphologies, specific surface areas, electronic structures, manganese valences, and defects of the MnO_2. Therefore, eliminating or reducing these interfering factors and then making a sound conclusion is in urgent need.

(3) The oxygen catalytic activity of MnO_2, especially OER activity in neutral and acidic electrolytes should be further enhanced. Several methods for improving MnO_2 catalyst were proposed and employed. However, they are usually implemented individually. Only few report demonstrated combined approach of two or more methods, which shows great synergy between different methods [58, 89]. Therefore, in the future work, combined methods for improving the activity of MnO_2 catalyst should be adopted for maximized synergy.

(4) The stability of MnO_2 ORR and OER catalyst in acidic and alkaline mediums should be further improved. Some reports showed that heterostructure forming, such as hybridization TiO_2 [82] or nitrogen-doped graphene [88] with MnO_2 could be the effective method to enhance stability in acidic and alkaline mediums. Accordingly, further development of heterostructure of MnO_2 catalyst should be a facile but effective route for improving its stability.

(5) Lastly, MnO_2 oxygen catalysts may find new applications in emerging energy storage devices. For instance, ORR and OER catalysts are indispensable in metal-air batteries including lithium-air and sodium-air batteries. In the new concept of seawater battery, ORR and OER occur on its cathode during the discharge and charge processes, respectively [260]. MnO_2 oxygen catalysts could play a role in these new batteries.

Acknowledgements

M. Yin, H. Miao and R. Hu are grateful for the financial supports from the National Natural Science Foundation of China (Grant No. 51871126), Ningbo major special projects of the Plan “Science and Technology Innovation 2025” (2019B10043 and 2020Z107), Zhejiang Provincial Natural Science Foundation of China Grant (Grant No. LY21E010002) and K.C. Wong Magna Fund in Ningbo University. Part of this work was conducted within the Delta-NTU Corporate Lab for Cyber-Physical Systems with funding support from Delta Electronics Inc. and the National Research Foundation (NRF) Singapore under the Corp Lab@University Scheme.

References

[1] H. Zhang, L. Lin, B. Wu, N. Hu, Vertical carbon skeleton introduced three-dimensional MnO_2 nanostructured composite electrodes for high-performance asymmetric supercapacitors, J. Power Sources 476 (2020) 228527.

[2] Q. Hu, M. Tang, M. He, N. Jiang, C. Xu, D. Lin, Q. Zheng, Core-shell MnO_2@CoS nanosheets with oxygen vacancies for high-performance supercapattery, J. Power Sources 446 (2020) 227335.

[3] S. Lindberg, S. Jeschke, P. Jankowski, M. Abdelhamid, T. Brousse, J. Le Bideau, P. Johansson, A. Matic, Charge storage mechanism of α-MnO_2 in protic and aprotic ionic liquid electrolytes, J. Power Sources 460 (2020) 228111.

[4] L. Cao, D. Li, T. Deng, Q. Li, C. Wang, Hydrophobic organic-electrolyte-protected zinc anodes for aqueous zinc batteries, Angew. Chem. Int. Ed. 59 (2020) 19292-19296.

[5] H.F. Wang, L.Y. Chen, H. Pang, S. Kaskel, Q. Xu, MOF-derived electrocatalysts for oxygen reduction, oxygen evolution and hydrogen evolution reactions, Chem. Soc. Rev. 49 (2020) 1414-1448.

[6] R. Cao, J. Lee, M. Liu, J. Cho, Recent progress in non-precious catalysts for metal-air batteries, Adv. Energy Mater. 2 (2012) 816-829.

[7] J. Liu, H. Zhang, M. Qiu, Z. Peng, M.K.H. Leung, W. Lin, J. Xuan, A review of non-precious metal single atom confined nanomaterials in different structural dimensions (1D–3D) as highly active oxygen redox reaction electrocatalysts, J. Mater. Chem. A 8 (2020) 2222-2245.

[8] H. Wang, M. Zhou, P. Choudhury, H. Luo, Perovskite oxides as bifunctional oxygen electrocatalysts for oxygen evolution/reduction reactions – A mini review, Appl. Mater. Today. 16 (2019) 56-71.

[9] H. Osgood, S.V. Devaguptapu, H. Xu, J. Cho, G. Wu, Transition metal (Fe, Co, Ni, and Mn) oxides for oxygen reduction and evolution bifunctional catalysts in alkaline media, Nano Today 11 (2016) 601-625.

[10] A.B. Anderson, T.V. Albu, Ab initio determination of reversible potentials and activation energies for outer-sphere oxygen reduction to water and the reverse oxidation reaction, J. Am. Chem. Soc. 121 (1999) 11855-11863.

[11] L. Wang, H. Li, J. Liu, X. Lang, W. Wang, Labile oxygen participant adsorbate evolving mechanism to enhance oxygen reduction in $SmMn_2O_5$ with double-coordinated crystal fields, J. Mater. Chem. A 9 (2021) 380-389.

[12] Y. Dai, H. Li, Y. Wang, K. Zhong, H. Zhang, J. Yu, Z. Huang, J. Yan, L. Huang, X. Liu, Y. Lu, T. Xu, M. Su, Zn-doped $CaFeO_3$ perovskite-derived high performed catalyst on oxygen reduction reaction in microbial fuel cells, J. Power Sources 489 (2021) 229498.

[13] X. Sun, K. Li, C. Yin, Y. Wang, M. Jiao, F. He, X. Bai, H. Tang, Z. Wu, Dual-site oxygen reduction reaction mechanism on CoN_4 and CoN_2 embedded graphene: Theoretical insights, Carbon 108 (2016) 541-550.

[14] X. Shen, T. Nagai, F. Yang, L.Q. Zhou, Y. Pan, L. Yao, D. Wu, Y.-S. Liu, J. Feng, J. Guo, H. Jia, Z. Peng, Dual-site cascade oxygen reduction mechanism on SnOx/Pt–Cu–Ni for promoting reaction kinetics, J. Am. Chem. Soc. 141 (2019) 9463-9467.

[15] N. Suen, S. Hung, Q. Quan, N. Zhang, Y. Xu, H.M. Chen, Electrocatalysis for the oxygen evolution reaction: recent development and future perspectives, Chem. Soc. Rev. 46 (2017) 337-365.

[16] J.S. Kim, B. Kim, H.A. Kim, K. Kang, Recent progress on multimetal oxide catalysts for the oxygen evolution reaction, Adv. Energy Mater. 8 (2018) 1702774.

[17] C. Han, W. Li, H. Liu, S.X. Dou, J. Wang, Design strategies for developing non-precious metal based bi-functional catalysts for alkaline electrolyte based Zinc–air batteries, Mater. Horiz. 6 (2019) 1812-1827.

[18] J. Song, C. Wei, Z.-F. Huang, C. Liu, L. Zeng, X. Wang, Z.J. Xu, A review on fundamentals for designing oxygen evolution electrocatalysts, Chem. Soc. Rev. 49 (2020) 2196-2214.

[19] W.-H. Huang, Q.-H. Li, D.-Y. Yu, Y.-H. Tang, D.-Y. Lin, F. Wang, J. Zhang, Hybrid zeolitic imidazolate frameworks for promoting electrocatalytic oxygen evolution via a dual-site relay mechanism, lnorg. Chem. (2021).

[20] A. Grimaud, O. Diaz-Morales, B. Han, W.T. Hong, Y.-L. Lee, L. Giordano, K.A. Stoerzinger, M.T.M. Koper, Y. Shao-Horn, Activating lattice oxygen redox reactions in metal oxides to catalyse oxygen evolution, Nat. Chem. 9 (2017) 457-465.

[21] D.A. Agyeman, Y. Zheng, T.-H. Lee, M. Park, W. Tamakloe, G.-H. Lee, H.W. Jang, K. Cho, Y.-M. Kang, Synergistic catalysis of the lattice oxygen and transition metal facilitating ORR and OER in perovskite catalysts for Li–O_2 batteries, ACS Catal. 11 (2021) 424-434.

[22] X. Rong, J. Parolin, A.M. Kolpak, A fundamental relationship between reaction mechanism and stability in metal oxide catalysts for oxygen evolution, ACS Catal. 6 (2016) 1153-1158.

[23] M. Schoen, N. Randell, O. Calderon, S.J. Villegas, K. Daly, R. Chernikov, S. Trudel, Local structural changes in polyamorphous (Ni,Fe)Ox electrocatalysts suggest a dual-site oxygen evolution reaction mechanism, ChemRxiv (2020).

[24] Z.-P. Wu, X.F. Lu, S.-Q. Zang, X.W. Lou, Non-noble-metal-based electrocatalysts toward the oxygen evolution reaction, Adv. Funct. Mater. 30 (2020) 1910274.

[25] H. Zhao, C. Sun, Z. Jin, D.-W. Wang, X. Yan, Z. Chen, G. Zhu, X. Yao, Carbon for the oxygen reduction reaction: a defect mechanism, J. Mater. Chem. A 3 (2015) 11736-11739.

[26] Q. Zhao, Z. Yan, C. Chen, J. Chen, Spinels: Controlled preparation, oxygen reduction/evolution reaction application, and beyond, Chem. Rev. 117 (2017) 10121-10211.

[27] D. Xiong, X. Wang, W. Li, L. Liu, Facile synthesis of iron phosphide nanorods for efficient and durable electrochemical oxygen evolution, Chem. Commun. 52 (2016) 8711-8714.

[28] F. Li, G.-F. Han, H.-J. Noh, S.-J. Kim, Y. Lu, H.Y. Jeong, Z. Fu, J.-B. Baek, Boosting oxygen reduction catalysis with abundant copper single atom active sites, Energ. Environ. Sci. 11 (2018) 2263-2269.

[29] Z. Wang, B. Xiao, Z. Lin, S. Shen, A. Xu, Z. Du, Y. Chen, W. Zhong, In-situ surface decoration of RuO_2 nanoparticles by laser ablation for improved oxygen evolution reaction activity in both acid and alkali solutions, J. Energy Chem. 54 (2021) 510-518.

[30] X. Wu, C. Tang, Y. Cheng, X. Min, S.P. Jiang, S. Wang, Bifunctional catalysts for reversible oxygen evolution reaction and oxygen reduction reaction, Chem-Eur. J. 26 (2020) 3906-3929.

[31] M.A. Kirsanova, V.D. Okatenko, D.A. Aksyonov, R.P. Forslund, J.T. Mefford, K.J. Stevenson, Artem M. Abakumov, Bifunctional OER/ORR catalytic activity in the tetrahedral $YBaCo_4O_{7.3}$ oxide, J. Mater. Chem. A 7 (2019) 330-341.

[32] H. Miao, S. Li, Z. Wang, S. Sun, M. Kuang, Z. Liu, J. Yuan, Enhancing the pyridinic N content of Nitrogen-doped graphene and improving its catalytic activity for oxygen reduction reaction, Int. J. Hydrogen Energ. 42 (2017) 28298-28308.

[33] H. Miao, X. Wu, B. Chen, Q. Wang, F. Wang, J. Wang, C. Zhang, H. Zhang, J. Yuan, Q. Zhang,

A-site deficient/excessive effects of $LaMnO_3$ perovskite as bifunctional oxygen catalyst for Zinc-air batteries, Electrochim. Acta 333 (2020) 135566.

[34] H.-F. Wang, C. Tang, B. Wang, B.-Q. Li, Q. Zhang, Bifunctional transition metal hydroxysulfides: Room-temperature sulfurization and their applications in Zn–air batteries, Adv. Mater. 29 (2017) 1702327.

[35] A. Pendashteh, J.S. Sanchez, J. Palma, M. Anderson, R. Marcilla, Anchored $NiCoMnS_4$ nanoparticles on N-doped rGO: High-performance bifunctional electrocatalysts for rechargeable Zn-Air batteries, Energy Storage Mater. 20 (2019) 216-224.

[36] A. Parra-Puerto, K.L. Ng, K. Fahy, A.E. Goode, M.P. Ryan, A. Kucernak, Supported transition metal phosphides: Activity survey for HER, ORR, OER, and corrosion resistance in acid and alkaline electrolytes, ACS Catal. 9 (2019) 11515-11529.

[37] P. Li, R. Ma, Y. Zhou, Y. Chen, Q. Liu, G. Peng, Z. Liang, J. Wang, Spinel nickel ferrite nanoparticles strongly cross-linked with multiwalled carbon nanotubes as a bi-efficient electrocatalyst for oxygen reduction and oxygen evolution, RSC Adv. 5 (2015) 73834-73841.

[38] S. Zhao, L. Yan, H. Luo, W.E. Mustain, H. Xu, Recent progress and perspectives of bifunctional oxygen reduction/evolution catalyst development for regenerative anion exchange membrane fuel cells, Nano Energy 47 (2018) 172-198.

[39] R. Craciun, B. Nentwick, K. Hadjiivanov, H. Knözinger, Structure and redox properties of MnOx/Yttrium-stabilized zirconia (YSZ) catalyst and its used in CO and CH_4 oxidation, Appl. Catal. A: Gen. 243 (2003) 67-79.

[40] W. Tang, M. Yao, Y. Deng, X. Li, N. Han, X. Wu, Y. Chen, Decoration of one-dimensional MnO_2 with Co_3O_4 nanoparticles: A heterogeneous interface for remarkably promoting catalytic oxidation activity, Chem. Eng. J. 306 (2016) 709-718.

[41] D. Yu, J. Yao, L. Qiu, Y. Wang, X. Zhang, Y. Feng, H. Wang, In situ growth of Co_3O_4 nanoparticles on α-MnO_2 nanotubes: a new hybrid for high-performance supercapacitors, J. Mater. Chem. A 2 (2014) 8465-8471.

[42] M.M. Najafpour, M. Kompany-Zareh, A. Zahraei, D. Jafarian Sedigh, H. Jaccard, M. Khoshkam, R.D. Britt, W.H. Casey, Mechanism, decomposition pathway and new evidence for self-healing of manganese oxides as efficient water oxidizing catalysts: new insights, Dalton Trans. 42 (2013) 14603-14611.

[43] B.M. Hunter, H.B. Gray, A.M. Müller, Earth-abundant heterogeneous water oxidation catalysts, Chem. Rev. 116 (2016) 14120-14136.

[44] K.A. Stoerzinger, M. Risch, B. Han, Y. Shao-horn, Recent insights into manganese oxides in catalyzing oxygen reduction kinetics, ACS Catal. 5 (2015) 6021-6031.

[45] K. Zhang, X. Han, Z. Hu, X. Zhang, Z. Tao, J. Chen, Nanostructured Mn-based oxides for electrochemical energy storage and conversion, Chem. Soc. Rev. 44 (2015) 699-728.

[46] Y. Hu, Y. Wu, J. Wang, Manganese-oxide-based electrode materials for energy storage applications: How close are we to the theoretical capacitance?, Adv. Mater. 30 (2018) 1802569.

[47] Y. Tang, S. Zheng, Y. Xu, X. Xiao, H. Xue, H. Pang, Advanced batteries based on manganese dioxide and its composites, Energy Storage Mater. 12 (2018) 284-309.

[48] Y. Dessie, S. Tadesse, R. Eswaramoorthy, B. Abebe, Recent developments in manganese oxide based nanomaterials with oxygen reduction reaction functionalities for energy conversion and storage applications: A review, J. Sci. Adv. Mater. Devices 4 (2019) 353-369.

[49] J. Emsley, Nature's building blocks: an AZ guide to the elements, Oxford, UK, Oxford University

Press, 2011.

[50] Y. Umena, K. Kawakami, J.-R. Shen, N. Kamiya, Crystal structure of oxygen-evolving photosystem II at a resolution of 1.9 Å, Nature 473 (2011) 55-60.

[51] B. Liu, Y. Sun, L. Liu, S. Xu, X. Yan, Advances in manganese-based oxides cathodic electrocatalysts for Li–air batteries, Adv. Funct. Mater. 28 (2018) 1704973.

[52] Z.Y. Leong, H.Y. Yang, A study of MnO_2 with different crystalline forms for pseudocapacitive desalination, ACS Appl. Mater. Inter. 11 (2019) 13176-13184.

[53] Y.L. Cao, H.X. Yang, X.P. Ai, L.F. Xiao, The mechanism of oxygen reduction on MnO_2-catalyzed air cathode in alkaline solution, J. Electroanal. Chem. 557 (2003) 127-134.

[54] F. Cheng, Y. Su, J. Liang, Z. Tao, J. Chen, MnO_2-based nanostructures as catalysts for electrochemical oxygen reduction in alkaline media†, Chem. Mater. 22 (2010) 898-905.

[55] Y. Meng, W. Song, H. Huang, Z. Ren, S.-Y. Chen, S.L. Suib, Structure-property relationship of bifunctional MnO_2 nanostructures: Highly efficient, ultra-stable electrochemical water oxidation and oxygen reduction reaction catalysts identified in alkaline media, J. Am. Chem. Soc. 136 (2014) 11452-11464.

[56] T.T. Truong, Y. Liu, Y. Ren, L. Trahey, Y. Sun, Morphological and crystalline evolution of nanostructured MnO_2 and its application in Lithium–air batteries, ACS Nano 6 (2012) 8067-8077.

[57] K. Selvakumar, S.M.S. Kumar, R. Thangamuthu, K. Ganesan, P. Murugan, P. Rajput, S.N. Jha, D. Bhattacharyya, Physiochemical investigation of shape-designed MnO_2 nanostructures and their influence on oxygen reduction reaction activity in alkaline solution, J. Phys. Chem. C 119 (2015) 6604-6618.

[58] Y. Gu, G. Yan, Y. Lian, P. Qi, Q. Mu, C. Zhang, Z. Deng, Y. Peng, MnIII-enriched α-MnO_2 nanowires as efficient bifunctional oxygen catalysts for rechargeable Zn-air batteries, Energy Storage Mater. 23 (2019) 252-260.

[59] X. Shi, H. Zheng, A.M. Kannan, K.Y. Perezsalcedo, B. Escobar, Effect of thermally induced oxygen vacancy of α-MnO_2 nanorods toward oxygen reduction reaction, lnorg. Chem. 58 (2019) 5335-5344.

[60] J. Shin, J.K. Seo, R. Yaylian, A. Huang, Y.S. Meng, A review on mechanistic understanding of MnO_2 in aqueous electrolyte for electrical energy storage systems, Int. Mater. Rev. 65 (2020) 356-387.

[61] Z. Zhang, J. Liu, J. Gu, L. Su, L. Cheng, An overview of metal oxide materials as electrocatalysts and supports for polymer electrolyte fuel cells, Energ. Environ. Sci. 7 (2014) 2535-2558.

[62] R. Burkitt, T.R. Whiffen, E.H. Yu, Iron phthalocyanine and MnOx composite catalysts for microbial fuel cell applications, Appl. Catal. B-Environ. 181 (2016) 279-288.

[63] K.N. Ferreira, T.M. Iverson, K. Maghlaoui, J. Barber, S. Iwata, Architecture of the photosynthetic oxygen-evolving center, Science 303 (2004) 1831-1838.

[64] X. Cai, L. Lai, J. Lin, Z. Shen, Recent advances in air electrodes for Zn–air batteries: electrocatalysis and structural design, Mater. Horiz. 4 (2017) 945-976.

[65] M.M. Najafpour, G. Renger, M. Holynska, A.N. Moghaddam, E.M. Aro, R. Carpentier, H. Nishihara, J.J. Eaton-Rye, J.R. Shen, S.I. Allakhverdiev, Manganese compounds as water-oxidizing catalysts: From the natural water-oxidizing complex to nanosized manganese oxide structures, Chem. Rev. 116 (2016) 2886-2936.

[66] A. Li, Y. Sun, T. Yao, H. Han, Earth-abundant transition-metal-based electrocatalysts for water electrolysis to produce renewable hydrogen, Chem-Eur. J. 24 (2018) 18334-18355.

[67] T. Takashima, A. Yamaguchi, K. Hashimoto, H. Irie, R. Nakamura, In situ UV-Vis absorption spectra of intermediate species for oxygen-evolution reaction on the surface of MnO_2 in neutral and alkaline media, Electrochemistry 82 (2014) 325-327.

[68] S. Anantharaj, V. Aravindan, Developments and perspectives in 3D transition-metal-based electrocatalysts for neutral and near-neutral water electrolysis, Adv. Energy Mater. 10 (2020) 1902666.

[69] I. Roger, M.D. Symes, First row transition metal catalysts for solar-driven water oxidation produced by electrodeposition, J. Mater. Chem. A 4 (2016) 6724-6741.

[70] T. Takashima, K. Hashimoto, R. Nakamura, Inhibition of charge disproportionation of MnO_2 electrocatalysts for efficient water oxidation under neutral conditions, J. Am. Chem. Soc. 134 (2012) 18153-18156.

[71] V. Tripkovic, H.A. Hansen, T. Vegge, Computational screening of doped alpha-MnO_2 catalysts for the oxygen evolution reaction, ChemSusChem 11 (2018) 629-637.

[72] A. Mathur, A. Halder, One-step synthesis of bifunctional iron-doped manganese oxide nanorods for rechargeable Zinc–air batteries, Catal. Sci. Technol. 9 (2019) 1245-1254.

[73] I.G. Mckendry, A.C. Thenuwara, S.L. Shumlas, H. Peng, Y.V. Aulin, P.R. Chinnam, E. Borguet, D.R. Strongin, M.J. Zdilla, Systematic doping of cobalt into layered manganese oxide sheets substantially enhances water oxidation catalysis, lnorg. Chem. 57 (2018) 557-564.

[74] C. Zhao, C. Yu, H. Huang, X. Han, Z. Liu, J. Qiu, Co ion-intercalation amorphous and ultrathin microstructure for high-rate oxygen evolution, Energy Storage Mater. 10 (2018) 291-296.

[75] H. Liao, X. Guo, Y. Hou, H. Liang, Z. Zhou, H. Yang, Construction of defect-rich Ni-Fe-doped $K_{0.23}MnO_2$ cubic nanoflowers via etching prussian blue analogue for efficient overall water splitting, Small 16 (2020) 1905223.

[76] Y. Zhao, J. Zhang, W. Wu, X. Guo, P. Xiong, H. Liu, G. Wang, Cobalt-doped MnO_2 ultrathin nanosheets with abundant oxygen vacancies supported on functionalized carbon nanofibers for efficient oxygen evolution, Nano Energy 54 (2018) 129-137.

[77] S. Zhang, W. Su, Y. Wei, J. Liu, K. Li, Mesoporous MnO_2 structured by ultrathin nanosheet as electrocatalyst for oxygen reduction reaction in air-cathode microbial fuel cell, J. Power Sources 401 (2018) 158-164.

[78] G. Cabello, R.A. Davoglio, Inorganic frameworks based on bimetallic nanoparticles encapsulated in hollow MnO_2 structures, Appl. Catal. B-Environ. 218 (2017) 192-198.

[79] G. Yan, Y. Lian, Y. Gu, C. Yang, H. Sun, Q. Mu, Q. Li, W. Zhu, X. Zheng, M. Chen, Phase and morphology transformation of MnO_2 induced by ionic liquids toward efficient water oxidation, ACS Catal. 8 (2018) 10137-10147.

[80] X. Zheng, L. Yu, B. Lan, G. Cheng, T. Lin, B. He, W. Ye, M. Sun, F. Ye, Three-dimensional radial α-MnO_2 synthesized from different redox potential for bifunctional oxygen electrocatalytic activities, J. Power Sources 362 (2017) 332-341.

[81] X. Li, M. Zhang, Y. Zhang, C. Yu, W. Qi, J. Cui, Y. Wang, Y. Qin, J. Liu, X. Shu, Y. Chen, T. Xie, Y. Wu, Controlled synthesis of MnO_2@TiO_2 hybrid nanotube arrays with enhanced oxygen evolution reaction performance, Int. J. Hydrogen Energ. 43 (2018) 14369-14378.

[82] R. Frydendal, E.A. Paoli, I. Chorkendorff, J. Rossmeisl, I.E.L. Stephens, Toward an active and stable catalyst for oxygen evolution in acidic media: Ti-stabilized MnO_2, Adv. Energy Mater. 5 (2015) 1500991.

[83] Y. Teng, X. Wang, J. Liao, W. Li, H. Chen, Y. Dong, D. Kuang, Atomically thin defect-rich Fe–

Mn–O hybrid nanosheets as high efficient electrocatalyst for water oxidation, Adv. Funct. Mater. 28 (2018) 1802463.

[84] J. He, M. Wang, W. Wang, R. Miao, W. Zhong, S.-Y. Chen, S. Poges, T. Jafari, W. Song, J. Liu, S.L. Suib, Hierarchical mesoporous NiO/MnO_2@PANI core shell microspheres, highly efficient and stable bifunctional electrocatalysts for oxygen evolution and reduction reactions, ACS Appl. Mater. Inter. 9 (2017) 42676-42687.

[85] X. Li, F. Dong, N. Xu, T. Zhang, K. Li, J. Qiao, Co_3O_4/MnO_2/hierarchically porous carbon as superior bifunctional electrodes for liquid and all-solid-state rechargeable Zinc–air batteries, ACS Appl. Mater. Inter. 10 (2018) 15591-15601.

[86] M. Fang, D. Han, W.-B. Xu, Y. Shen, Y. Lu, P. Cao, S. Han, W. Xu, D. Zhu, W. Liu, J.C. Ho, Surface-guided formation of amorphous mixed-metal oxyhydroxides on ultrathin MnO_2 nanosheet arrays for efficient electrocatalytic oxygen evolution, Adv. Energy Mater. 10 (2020) 2001059.

[87] J. Melder, S. Mebs, P. Heizmann, R. Lang, H. Dau, P. Kurz, Carbon fibre paper coated by a layered manganese oxide: a nano-structured electrocatalyst for water-oxidation with high activity over a very wide pH range, J. Mater. Chem. A 7 (2019) 25333-25346.

[88] H. Miao, B. Chen, S. Li, X. Wu, Q. Wang, C. Zhang, Z. Sun, H. Li, All-solid-state flexible Zinc-air battery with polyacrylamide alkaline gel electrolyte, J. Power Sources 450 (2020) 227653.

[89] Y. Zhao, C. Chang, F. Teng, Y. Zhao, G. Chen, R. Shi, G.I.N. Waterhouse, W. Huang, T. Zhang, Defect-engineered ultrathin δ-MnO_2 nanosheet arrays as bifunctional electrodes for efficient overall water splitting, Adv. Energy Mater. 7 (2017) 1700005.

[90] B. Lan, X. Zheng, G. Cheng, J. Han, W. Li, M. Sun, L. Yu, The art of balance: Engineering of structure defects and electrical conductivity of α-MnO_2 for oxygen reduction reaction, Electrochim. Acta 283 (2018) 459-466.

[91] F.Y. Cheng, T.R. Zhang, Y. Zhang, J. Du, X.P. Han, J. Chen, Enhancing electrocatalytic oxygen reduction on MnO_2 with vacancies, Angew. Chem. Int. Edit. 52 (2013) 2474-2477.

[92] D.A. Tompsett, S.C. Parker, M.S. Islam, Rutile (β-)MnO_2 surfaces and vacancy formation for high electrochemical and catalytic performance, J. Am. Chem. Soc. 136 (2014) 1418-1426.

[93] S. Lee, G. Nam, J. Sun, J. Lee, H. Lee, W. Chen, J. Cho, Y. Cui, Enhanced intrinsic catalytic activity of λ-MnO_2 by electrochemical tuning and oxygen vacancy generation, Angew. Chem. Int. Edit. 55 (2016) 8599-8604.

[94] T. Zhang, F. Cheng, J. Du, Y. Hu, J. Chen, Efficiently enhancing oxygen reduction electrocatalytic activity of MnO_2 using facile hydrogenation, Adv. Energy Mater. 5 (2015) 1400654.

[95] Z. Morgan Chan, D.A. Kitchaev, J. Nelson Weker, C. Schnedermann, K. Lim, G. Ceder, W. Tumas, M.F. Toney, D.G. Nocera, Electrochemical trapping of metastable Mn(3+) ions for activation of MnO_2 oxygen evolution catalysts, P. Natl. Acad. Sci. USA 115 (2018) E5261-E5268.

[96] B. Xu, H. Lu, W. Cai, Y. Cao, Y. Deng, W. Yang, Synergistically enhanced oxygen reduction reaction composites of specific surface area and manganese valence controlled α-MnO_2 nanotube decorated by silver nanoparticles in Al-air batteries, Electrochim. Acta 305 (2019) 360-369.

[97] P.K. Gupta, A. Bhandari, S. Saha, J. Bhattacharya, R.G.S. Pala, Modulating oxygen evolution reactivity in MnO_2 through polymorphic engineering, J. Phys. Chem. C. 123 (2019) 22345-22357.

[98] G. Gupta, K. Selvakumar, N. Lakshminarasimhan, S.M. Senthil Kumar, M. Mamlouk, The effects of morphology, microstructure and mixed-valent states of MnO_2 on the oxygen evolution reaction activity in alkaline anion exchange membrane water electrolysis, J. Power Sources 461 (2020)

228131.

[99] L. Tian, X. Zhai, X. Wang, X. Pang, J. Li, Z. Li, Morphology and phase transformation of α-MnO_2/MnOOH modulated by N-CDs for efficient electrocatalytic oxygen evolution reaction in alkaline medium, Electrochim. Acta 337 (2020) 135823.

[100] G. Elmacı, A.S. Ertürk, M. Sevim, Ö. Metin, MnO_2 nanowires anchored on mesoporous graphitic carbon nitride (MnO_2@mpg-C_3N_4) as a highly efficient electrocatalyst for the oxygen evolution reaction, Int. J. Hydrogen Energ. 44 (2019) 17995-18006.

[101] Y. Han, Y. Yu, L. Zhang, L. Huang, J. Zhai, S. Dong, Facile synthesis of Ni based metal-organic frameworks wrapped MnO_2 nanowires with high performance toward electrochemical oxygen evolution reaction, Talanta 186 (2018) 154-161.

[102] K. Fujimoto, T. Okada, M. Nakayama, Enhanced oxygen evolution reaction activity of co ions isolated in the interlayer space of buserite MnO_2, J. Phys. Chem. C. 122 (2018) 8406-8413.

[103] X. Xiong, Y. Ji, M. Xie, C. You, L. Yang, Z. Liu, A.M. Asiri, X. Sun, MnO_2-CoP_3 nanowires array: An efficient electrocatalyst for alkaline oxygen evolution reaction with enhanced activity, Electrochem. Commun. 86 (2018) 161-165.

[104] K.-L. Yan, X. Shang, W.-K. Gao, B. Dong, X. Li, J.-Q. Chi, Y.-R. Liu, Y.-M. Chai, C.-G. Liu, Ternary MnO_2/$NiCo_2O_4$/NF with hierarchical structure and synergistic interaction as efficient electrocatalysts for oxygen evolution reaction, J. Alloys Compd. 719 (2017) 314-321.

[105] Z. Ye, T. Li, G. Ma, Y. Dong, X. Zhou, Metal-ion (Fe, V, Co, and Ni)-doped MnO_2 ultrathin nanosheets supported on carbon fiber paper for the oxygen evolution reaction, Adv. Funct. Mater. 27 (2017) 1704083.

[106] W. Sun, Z. Zhou, W.Q. Zaman, L.-m. Cao, J. Yang, Rational manipulation of IrO_2 lattice strain on α-MnO_2 nanorods as a highly efficient water-splitting catalyst, ACS Appl. Mater. Inter. 9 (2017) 41855-41862.

[107] M. Nakayama, Y. Fujii, K. Fujimoto, M. Yoshimoto, A. Kaide, T. Saeki, H. Asada, Electrochemical synthesis of a nanohybrid film consisting of stacked graphene sheets and manganese oxide as oxygen evolution reaction catalyst, RSC Adv. 6 (2016) 23377-23382.

[108] J. Kim, J.S. Kim, H. Baik, K. Kang, K. Lee, Porous β-MnO_2 nanoplates derived from $MnCO_3$ nanoplates as highly efficient electrocatalysts toward oxygen evolution reaction, RSC Adv. 6 (2016) 26535-26539.

[109] H.S. Jeon, S.J. Ahn, M.S. Jee, S.S. Yoon, Y.J. Hwang, B.K. Min, Water oxidation by manganese oxide electrocatalytic films synthesized by chemical solution deposition method, J. Electrochem. Soc. 163 (2016) F3113-F3118.

[110] C. Xiong, Q. Yang, W. Dang, M. Li, B. Li, J. Su, Y. Liu, W. Zhao, C. Duan, L. Dai, Y. Xu, Y. Ni, Fabrication of eco-friendly carbon microtubes @ nitrogen-doped reduced graphene oxide hybrid as an excellent carbonaceous scaffold to load MnO_2 nanowall (PANI nanorod) as bifunctional material for high-performance supercapacitor and oxygen reduction reaction catalyst, J. Power Sources 447 (2020) 227387.

[111] C. Cui, G. Du, K. Zhang, T. An, B. Li, X. Liu, Z. Liu, Co_3O_4 nanoparticles anchored in MnO_2 nanorods as efficient oxygen reduction reaction catalyst for metal-air batteries, J. Alloys Compd. 814 (2020) 152239.

[112] J.-X. Zhang, L.-N. Zhou, J. Cheng, X. Yin, W.-T. Kuang, Y.-J. Li, CoII-catalyzed room-temperature growth of MnO_2 on the skeleton of carbonized zeolitic imidazolate framework-67 crystals for boosting oxygen reduction reaction, J. Mater. Chem. A 7 (2019) 4699-4704.

[113] H. Begum, M.S. Ahmed, S. Jeon, δ-MnO_2 nanoflowers on sulfonated graphene sheets for stable oxygen reduction and hydrogen evolution reaction, Electrochim. Acta 296 (2019) 235-242.

[114] J.A. Vigil, T.N. Lambert, J. Duay, C.J. Delker, T.E. Beechem, B.S. Swartzentruber, Nanoscale carbon modified α-MnO_2 nanowires: Highly active and stable oxygen reduction electrocatalysts with low carbon content, ACS Appl. Mater. Inter. 10 (2018) 2040-2050.

[115] T.N. Lambert, J.A. Vigil, S.E. White, C.J. Delker, D.J. Davis, M. Kelly, M.T. Brumbach, M.A. Rodriguez, B.S. Swartzentruber, Understanding the effects of cationic dopants on α-MnO_2 oxygen reduction reaction electrocatalysis, J. Phys. Chem. C. 121 (2017) 2789-2797.

[116] G. Cheng, S. Xie, B. Lan, X. Zheng, F. Ye, M. Sun, X. Lu, L. Yu, Phase controllable synthesis of three-dimensional star-like MnO_2 hierarchical architectures as highly efficient and stable oxygen reduction electrocatalysts, J. Mater. Chem. A 4 (2016) 16462-16468.

[117] G. Chen, J. Sunarso, Y. Zhu, J. Yu, Y. Zhong, W. Zhou, Z. Shao, Highly active carbon/α-MnO_2 hybrid oxygen reduction reaction electrocatalysts, ChemElectroChem 3 (2016) 1760-1767.

[118] Q. Yu, J. Xu, C. Wu, J. Zhang, L. Guan, MnO_2 nanofilms on nitrogen-doped hollow graphene spheres as a high-performance electrocatalyst for oxygen reduction reaction, ACS Appl. Mater. Inter. 8 (2016) 35264-35269.

[119] H. Wang, F. Yin, B. Chen, G. Li, Synthesis of an ε-MnO_2/metal–organic-framework composite and its electrocatalysis towards oxygen reduction reaction in an alkaline electrolyte, J. Mater. Chem. A 3 (2015) 16168-16176.

[120] M.A. Pellow, C.J.M. Emmott, C.J. Barnhart, S.M. Benson, Hydrogen or batteries for grid storage? A net energy analysis, Energ. Environ. Sci. 8 (2015) 1938-1952.

[121] C. Wang, Y. Yu, J. Niu, Y. Liu, D. Bridges, X. Liu, J. Pooran, Y. Zhang, A. Hu, Recent progress of metal–air batteries—a mini review, Appl. Sci-Basel 9 (2019) 2787.

[122] F. Cheng, J. Chen, Metal–air batteries: from oxygen reduction electrochemistry to cathode catalysts, Chem. Soc. Rev. 41 (2012) 2172-2192.

[123] Z. Wang, D. Xu, J. Xu, X. Zhang, Oxygen electrocatalysts in metal–air batteries: from aqueous to nonaqueous electrolytes, Chem. Soc. Rev. 43 (2014) 7746-7786.

[124] N. Chawla, Recent advances in air-battery chemistries, Mater. Today Chem. 12 (2019) 324-331.

[125] Y. Li, H. Dai, Recent advances in zinc–air batteries, Chem. Soc. Rev. 43 (2014) 5257-5275.

[126] P. Gu, M. Zheng, Q. Zhao, X. Xiao, H. Xue, H. Pang, Rechargeable zinc–air batteries: a promising way to green energy, J. Mater. Chem. A 5 (2017) 7651-7666.

[127] A.R. Mainar, E. Iruin, L.C. Colmenares, A. Kvasha, I. de Meatza, M. Bengoechea, O. Leonet, I. Boyano, Z.C. Zhang, J.A. Blazquez, An overview of progress in electrolytes for secondary Zinc-air batteries and other storage systems based on zinc, J. Energy Storage 15 (2018) 304-328.

[128] C. Li, M. Wu, R.J.A.C.B.-e. Liu, High-performance bifunctional oxygen electrocatalysts for Zinc-air batteries over mesoporous Fe/Co-N-C nanofibers with embedding FeCo alloy nanoparticles, Appl. Catal. B-Environ. 244 (2019) 150-158.

[129] A. Kulkarni, S. Siahrostami, A. Patel, J.K. Norskov, Understanding catalytic activity trends in the oxygen reduction reaction, Chem. Rev. 118 (2018) 2302-2312.

[130] J. Pan, Y. Xu, H. Yang, Z. Dong, H. Liu, B.Y. Xia, Advanced architectures and relatives of air electrodes in Zn-air batteries, Adv. Sci. 5 (2018) 1700691-1700691.

[131] Y. Huang, Y. Lin, W. Li, Controllable syntheses of α- and δ-MnO_2 as cathode catalysts for Zinc-air battery, Electrochim. Acta 99 (2013) 161-165.

[132] P. Li, C. Hu, T. Lee, W. Chang, T.H. Wang, Synthesis and characterization of carbon

black/manganese oxide air cathodes for Zinc-air batteries, J. Power Sources 269 (2014) 88-97.

[133] P. Li, C. Hu, H. Noda, H. Habazaki, Synthesis and characterization of carbon black/manganese oxide air cathodes for Zinc–air batteries: Effects of the crystalline structure of manganese oxides, J. Power Sources 298 (2015) 102-113.

[134] A.R. Mainar, L.C. Colmenares, O. Leonet, F. Alcaide, J.J. Iruin, S. Weinberger, V. Hacker, E. Iruin, I. Urdanpilleta, J.A. Blazquez, Manganese oxide catalysts for secondary Zinc air batteries: from electrocatalytic activity to bifunctional air electrode performance, Electrochim. Acta 217 (2016) 80-91.

[135] A. Sumboja, X. Ge, F.W.T. Goh, B. Li, D. Geng, T.S.A. Hor, Y. Zong, Z. Liu, Manganese oxide catalyst grown on carbon paper as an air cathode for high-performance rechargeable Zinc–air batteries, ChemPlusChem 80 (2015) 1341-1346.

[136] A. Sumboja, M. Lubke, Y. Wang, T. An, Y. Zong, Z. Liu, All-solid-state, foldable, and rechargeable Zn-air batteries based on manganese oxide grown on graphene-coated carbon cloth air cathode, Adv. Energy Mater. 7 (2017) 1700927.

[137] S. Chen, X. Shu, H. Wang, J. Zhang, Thermally driven phase transition of manganese oxide on carbon cloth for enhancing the performance of flexible all-solid-state Zinc–air batteries, J. Mater. Chem. A 7 (2019) 19719-19727.

[138] P. Li, Y. Chien, C. Hu, Novel configuration of bifunctional air electrodes for rechargeable Zinc–air batteries, J. Power Sources 313 (2016) 37-45.

[139] M. Xiong, D.G. Ivey, Sequentially electrodeposited MnOx/Co-Fe as bifunctional electrocatalysts for rechargeable Zinc-air batteries, J. Electrochem. Soc. 164 (2017) A1012-A1021.

[140] N. Xu, X. Li, H. Li, Y. Wei, J. Qiao, A novel composite (FMC) to serve as a durable 3D-clam-shaped bifunctional cathode catalyst for both primary and rechargeable Zinc-air batteries, Sci. Bull. 62 (2017) 1216-1226.

[141] S. Ni, H. Zhang, Y. Zhao, X. Li, Y. Sun, J. Qian, Q. Xu, P. Gao, D. Wu, K. Kato, Single atomic Ag enhances the bifunctional activity and cycling stability of MnO_2, Chem. Eng. J. 366 (2019) 631-638.

[142] M. Mokhtar, M.Z.M. Talib, E.H. Majlan, S.M. Tasirin, W. Ramli, W.R.W. Daud, J. Sahari, Recent developments in materials for Aluminum–air batteries: A review, J. Ind. Eng. Chem. 32 (2015) 1-20.

[143] D.R. Egan, C.P. de Leon, R.J.K. Wood, R.L. Jones, K.R. Stokes, F.C. Walsh, Developments in electrode materials and electrolytes for Aluminium-air batteries, J. Power Sources 236 (2013) 293-310.

[144] M.A. Rahman, X. Wang, C. Wen, High energy density metal-air batteries: A review, J. Electrochem. Soc. 160 (2013) A1759-A1771.

[145] S. Sun, H. Miao, Y. Xue, Q. Wang, S. Li, Z. Liu, Oxygen reduction reaction catalysts of manganese oxide decorated by silver nanoparticles for Aluminum-air batteries, Electrochim. Acta 214 (2016) 49-55.

[146] J. Ryu, H. Jang, J. Park, Y. Yoo, M. Park, J. Cho, Seed-mediated atomic-scale reconstruction of silver manganate nanoplates for oxygen reduction towards high-energy Aluminum-air flow batteries, Nat. Commun. 9 (2018) 3715.

[147] S. Sun, H. Miao, Y. Xue, Q. Wang, Q. Zhang, Z. Dong, S. Li, H. Huang, Z. Liu, High electrocatalytic activity of silver-doped manganese dioxide toward oxygen reduction reaction in Aluminum-air battery, J. Electrochem. Soc. 164 (2017) F768-F774.

[148] S. Sun, Y. Xue, Q. Wang, H. Huang, H. Miao, Z. Liu, Cerium ion intercalated MnO_2 nanospheres with high catalytic activity toward oxygen reduction reaction for Aluminum-air batteries, Electrochim. Acta 263 (2018) 544-554.

[149] S. Clark, A.R. Mainar, E. Iruin, L.C. Colmenares, J.A. Blazquez, J.R. Tolchard, A. Latz, B. Horstmann, Towards rechargeable Zinc–air batteries with aqueous chloride electrolytes, J. Mater. Chem. A 7 (2019) 11387-11399.

[150] K. Izumiya, E. Akiyama, H. Habazaki, N. Kumagai, A. Kawashima, K. Hashimoto, Anodically deposited manganese oxide and manganese–tungsten oxide electrodes for oxygen evolution from seawater, Electrochim. Acta 43 (1998) 3303-3312.

[151] E. Iruin, A.R. Mainar, M. Enterria, N. Ortizvitoriano, J.A. Blazquez, L.C. Colmenares, T. Rojo, S. Clark, B. Horstmann, Designing a manganese oxide bifunctional air electrode for aqueous chloride-based electrolytes in secondary Zinc-air batteries, Electrochim. Acta 320 (2019) 134557.

[152] F.W.T. Goh, Z. Liu, T.S.A. Hor, J. Zhang, X. Ge, Y. Zong, A. Yu, W. Khoo, A near-neutral chloride electrolyte for electrically rechargeable Zinc-air batteries, J. Electrochem. Soc. 161 (2014) A2080-A2086.

[153] A. Sumboja, X. Ge, G. Zheng, F.W.T. Goh, T.S.A. Hor, Y. Zong, Z. Liu, Durable rechargeable Zinc-air batteries with neutral electrolyte and manganese oxide catalyst, J. Power Sources 332 (2016) 330-336.

[154] S. Clark, A. Latz, B. Horstmann, Rational development of neutral aqueous electrolytes for Zinc-air batteries, ChemSusChem 10 (2017) 4735-4747.

[155] C. Li, Y. Sun, F.A. Gebert, S. Chou, Current progress on rechargeable Magnesium–air battery, Adv. Energy Mater. 7 (2017) 1700869.

[156] Y. Xue, H. Miao, S. Sun, Q. Wang, S. Li, Z. Liu, Template-directed fabrication of porous gas diffusion layer for Magnesium air batteries, J. Power Sources 297 (2015) 202-207.

[157] Y. Li, X. Zhang, H. Li, H.D. Yoo, X. Chi, Q. An, J. Liu, M. Yu, W. Wang, Y. Yao, Mixed-phase mullite electrocatalyst for pH-neutral oxygen reduction in Magnesium-air batteries, Nano Energy 27 (2016) 8-16.

[158] C.-S. Li, Y. Sun, W.-H. Lai, J.-Z. Wang, S.-L. Chou, Ultrafine Mn_3O_4 nanowires/three-dimensional graphene/single-walled carbon nanotube composites: Superior electrocatalysts for oxygen reduction and enhanced Mg/air batteries, ACS Appl. Mater. Inter. 8 (2016) 27710-27719.

[159] P. Yue, Z. Li, S. Wang, Y. Wang, MnO_2 nanorod catalysts for Magnesium–air fuel cells: Influence of different supports, Int. J. Hydrogen Energ. 40 (2015) 6809-6817.

[160] Z. Zhang, Z. Li, C. Sun, T. Zhang, S. Wang, Preparation and properties of an amorphous MnO_2/CNTs-OH catalyst with high dispersion and durability for Magnesium-air fuel cells, Catal. Today 298 (2017) 241-249.

[161] P.Y. You, S.K. Kamarudin, Recent progress of carbonaceous" materials in fuel cell applications: An overview, Chem. Eng. J. 309 (2017) 489-502.

[162] O.Z. Sharaf, M.F. Orhan, An overview of fuel cell technology: Fundamentals and applications, Renew. Sust. Energ. Rev. 32 (2014) 810-853.

[163] Z.F. Pan, L. An, T.S. Zhao, Z.K. Tang, Advances and challenges in alkaline anion exchange membrane fuel cells, Prog. Energ. Combust. 66 (2018) 141-175.

[164] Y. Wang, J. Qiao, R. Baker, J. Zhang, Alkaline polymer electrolyte membranes for fuel cell applications, Chem. Soc. Rev. 42 (2013) 5768-5787.

[165] C. Lafforgue, A. Zadick, L. Dubau, F. Maillard, M. Chatenet, Selected review of the degradation

of Pt and Pd-based carbon-supported electrocatalysts for alkaline fuel cells: Towards mechanisms of degradation, Fuel Cells 18 (2018) 229-238.

[166] N. Ramaswamy, S. Mukerjee, Alkaline anion-exchange membrane fuel cells: Challenges in electrocatalysis and interfacial charge transfer, Chem. Rev. 119 (2019) 11945-11979.

[167] J. Pan, C. Chen, L. Zhuang, J. Lu, Designing advanced alkaline polymer electrolytes for fuel cell applications, Acc. Chem. Res. 45 (2012) 473-481.

[168] Y. Wang, D.Y.C. Leung, J. Xuan, H. Wang, A review on unitized regenerative fuel cell technologies, part B: Unitized regenerative alkaline fuel cell, solid oxide fuel cell, and microfluidic fuel cell, Renew. Sust. Energ. Rev. 75 (2017) 775-795.

[169] M. Chen, L. Wang, H. Yang, S. Zhao, H. Xu, G. Wu, Nanocarbon/oxide composite catalysts for bifunctional oxygen reduction and evolution in reversible alkaline fuel cells: A mini review, J. Power Sources 375 (2018) 277-290.

[170] L. An, T. Zhao, An alkaline direct ethanol fuel cell with a cation exchange membrane, Energ. Environ. Sci. 4 (2011) 2213-2217.

[171] L. An, T. Zhao, Y. Li, Q. Wu, Charge carriers in alkaline direct oxidation fuel cells, Energ. Environ. Sci. 5 (2012) 7536-7538.

[172] K. Selvakumar, S. Kumar, R. Thangamuthu, G. Kruthika, P. Murugan, Development of shape-engineered α-MnO_2 materials as bi-functional catalysts for oxygen evolution reaction and oxygen reduction reaction in alkaline medium, Int. J. Hydrogen Energ. 39 (2014) 21024-21036.

[173] W. Huang, H. Zhong, D. Li, P. Tang, Y. Feng, Reduced graphene oxide supported CoO/MnO_2 electrocatalysts from layered double hydroxides for oxygen reduction reaction, Electrochim. Acta 173 (2015) 575-580.

[174] Z. Xia, X. Zhang, H. Sun, S. Wang, G. Sun, Recent advances in multi-scale design and construction of materials for direct methanol fuel cells, Nano Energy 65 (2019) 104048.

[175] E. Antolini, Photo-assisted methanol oxidation on Pt-TiO_2 catalysts for direct methanol fuel cells: A short review, Appl. Catal. B-Environ. 237 (2018) 491-503.

[176] A.S. Moura, J.L.C. Fajin, M. Mandado, M.N.D.S. Cordeiro, Ruthenium–platinum catalysts and direct methanol fuel cells (DMFC): A review of theoretical and experimental breakthroughs, Catalysts 7 (2017) 47.

[177] L. Gong, Z. Yang, K. Li, W. Xing, C. Liu, J. Ge, Recent development of methanol electrooxidation catalysts for direct methanol fuel cell, J. Energy Chem. 27 (2018) 1618-1628.

[178] J. Zhang, K. Sasaki, E. Sutter, R.R. Adzic, Stabilization of platinum oxygen-reduction electrocatalysts using gold clusters, Science 315 (2007) 220-222.

[179] Y. Tan, C. Xu, G. Chen, X. Fang, N. Zheng, Q. Xie, Facile synthesis of manganese-oxide-containing mesoporous nitrogen-doped carbon for efficient oxygen reduction, Adv. Funct. Mater. 22 (2012) 4584-4591.

[180] M.S. Eldeab, G.H. Elnowihy, A.M. Mohammad, Synergistic enhancement of the electro-oxidation of methanol at tailor-designed nanoparticle-based CoOx/MnOx/Pt ternary catalysts, Electrochim. Acta 165 (2015) 402-409.

[181] J.C. Abregomartinez, Y. Wang, A. Morenozuria, Q. Wei, F.M. Cuevasmuniz, L.G. Arriaga, S. Sun, M. Mohamedi, Nanostructured Mn_2O_3/Pt/CNTs selective electrode for oxygen reduction reaction and methanol tolerance in mixed-reactant membraneless micro-DMFC, Electrochim. Acta 297 (2019) 230-239.

[182] J. Lee, G.S. Park, H.I. Lee, S.T. Kim, R. Cao, M. Liu, J. Cho, Ketjenblack carbon supported

amorphous manganese oxides nanowires as highly efficient electrocatalyst for oxygen reduction reaction in alkaline solutions, Nano Lett. 11 (2011) 5362-5366.

[183] J. Zhang, C.X. Guo, L. Zhang, C.M. Li, Direct growth of flower-like manganese oxide on reduced graphene oxide towards efficient oxygen reduction reaction, Chem. Commun. 49 (2013) 6334-6336.

[184] C. Wei, L. Yu, C. Cui, J. Lin, C. Wei, N. Mathews, F. Huo, T. Sritharan, Z.J. Xu, Ultrathin MnO_2 nanoflakes as efficient catalysts for oxygen reduction reaction, Chem. Commun. 50 (2014) 7885-7888.

[185] Y. Fang, X. Yang, L. Wang, Y. Liu, Microspheres assembled by KMn_8O_{16} nanorods and their catalytic oxygen reduction activity in direct methanol fuel cells, J. Power Sources 267 (2014) 33-38.

[186] J.A. Dawson, H. Chen, I. Tanaka, First-principles calculations of oxygen vacancy formation and metallic behavior at a β-MnO_2 grain boundary, ACS Appl. Mater. Inter. 7 (2015) 1726-1734.

[187] L. Xu, Q. Jiang, Z. Xiao, X. Li, J. Huo, S. Wang, L. Dai, Plasma-engraved Co_3O_4 nanosheets with oxygen vacancies and high surface area for the oxygen evolution reaction, Angew. Chem. Int. Edit. 55 (2016) 5277-5281.

[188] Y. Wang, T. Zhou, K. Jiang, P. Da, Z. Peng, J. Tang, B. Kong, W. Cai, Z. Yang, G. Zheng, Reduced mesoporous Co_3O_4 nanowires as efficient water oxidation electrocatalysts and supercapacitor electrodes, Adv. Energy Mater. 4 (2014) 1400696.

[189] Y. Choi, D. Lim, E. Oh, C. Lim, S.H. Baeck, Effect of proton irradiation on electrocatalytic properties of MnO_2 for oxygen reduction reaction, J. Mater. Chem. A 7 (2019) 11659-11664.

[190] C.A. Ramirezvargas, A. Prado, C.A. Arias, P.N. Carvalho, A. Estevenunez, H. Brix, Microbial electrochemical technologies for wastewater treatment: Principles and evolution from microbial fuel cells to bioelectrochemical-based constructed wetlands, Water 10 (2018) 1128.

[191] A.J. Slate, K.A. Whitehead, D.A.C. Brownson, C.E. Banks, Microbial fuel cells: An overview of current technology, Renew. Sust. Energ. Rev. 101 (2019) 60-81.

[192] Y. Zhang, M. Liu, M. Zhou, H. Yang, L. Liang, T. Gu, Microbial fuel cell hybrid systems for wastewater treatment and bioenergy production: Synergistic effects, mechanisms and challenges, Renew. Sust. Energ. Rev. 103 (2019) 13-29.

[193] S.G.A. Flimban, I.M.I. Ismail, T. Kim, S.E. Oh, Overview of recent advancements in the microbial fuel cell from fundamentals to applications: Design, major elements, and scalability, Energies 12 (2019) 3390.

[194] H. Yuan, Y. Hou, I.M. Abureesh, J. Chen, Z. He, Oxygen reduction reaction catalysts used in microbial fuel cells for energy-efficient wastewater treatment: a review, Mater. Horiz. 3 (2016) 382-401.

[195] C. Santoro, C. Arbizzani, B. Erable, I. Ieropoulos, Microbial fuel cells: From fundamentals to applications. A review, J. Power Sources 356 (2017) 225-244.

[196] Y. Zhang, L. Liu, B.V. Der Bruggen, F. Yang, Nanocarbon based composite electrodes and their application in microbial fuel cells, J. Mater. Chem. A 5 (2017) 12673-12698.

[197] S. Li, C. Cheng, A. Thomas, Carbon-based microbial-fuel-cell electrodes: From conductive supports to active catalysts, Adv. Mater. 29 (2017) 1602547.

[198] S. Mateo, P. Canizares, F.J. Fernandezmorales, M.A. Rodrigo, A critical view of microbial fuel cells: What is the next stage?, ChemSusChem 11 (2018) 4183-4192.

[199] C. Xia, D. Zhang, W. Pedrycz, Y. Zhu, Y. Guo, Models for microbial fuel cells: A critical review,

J. Power Sources 373 (2018) 119-131.

[200] K.B. Liew, W.R.W. Daud, M. Ghasemi, J.X. Leong, S.S. Lim, M. Ismail, Non-Pt catalyst as oxygen reduction reaction in microbial fuel cells: A review, Int. J. Hydrogen Energ. 39 (2014) 4870-4883.

[201] Q. Wen, S. Wang, J. Yan, L. Cong, Z. Pan, Y. Ren, Z. Fan, MnO_2–graphene hybrid as an alternative cathodic catalyst to platinum in microbial fuel cells, J. Power Sources 216 (2012) 187-191.

[202] R.K. Gautam, H. Bhattacharjee, S.V. Mohan, A. Verma, Nitrogen doped graphene supported α-MnO_2 nanorods for efficient ORR in a microbial fuel cell, RSC Adv. 6 (2016) 110091-110101.

[203] A. Tofighi, M. Rahimnejad, M. Ghorbani, Ternary nanotube -MnO_2/GO/AC as an excellent alternative composite modifier for cathode electrode of microbial fuel cell, J. Therm. Anal. Calorim. 135 (2019) 1667-1675.

[204] K.B. Liew, W.R.W. Daud, M. Ghasemi, K.S. Loh, M. Ismail, S.S. Lim, J.X. Leong, Manganese oxide/functionalised carbon nanotubes nanocomposite as catalyst for oxygen reduction reaction in microbial fuel cell, Int. J. Hydrogen Energ. 40 (2015) 11625-11632.

[205] S.A. Ansari, N. Parveen, T.H. Han, M.O. Ansari, M.H. Cho, Fibrous polyaniline@manganese oxide nanocomposites as supercapacitor electrode materials and cathode catalysts for improved power production in microbial fuel cells, Phys. Chem. Chem. Phys. 18 (2016) 9053-9060.

[206] X. Zhou, Y. Xu, X. Mei, N. Du, R. Jv, Z. Hu, S. Chen, Polyaniline/β-MnO_2 nanocomposites as cathode electrocatalyst for oxygen reduction reaction in microbial fuel cells, Chemosphere 198 (2018) 482-491.

[207] D. Qiu, L. Peng, X. Lai, M. Ni, W. Lehnert, Mechanical failure and mitigation strategies for the membrane in a proton exchange membrane fuel cell, Renew. Sust. Energ. Rev. 113 (2019) 109289.

[208] Q. Meyer, Y. Zeng, C. Zhao, In situ and operando characterization of proton exchange membrane fuel cells, Adv. Mater. 31 (2019) 1901900.

[209] E.H. Majlan, D. Rohendi, W.R.W. Daud, T. Husaini, M.A. Haque, Electrode for proton exchange membrane fuel cells: A review, Renew. Sust. Energ. Rev. 89 (2018) 117-134.

[210] X.X. Wang, M.T. Swihart, G. Wu, Achievements, challenges and perspectives on cathode catalysts in proton exchange membrane fuel cells for transportation, Nat. Catal. 2 (2019) 578-589.

[211] C.-Y. Liu, C.-C. Sung, A review of the performance and analysis of proton exchange membrane fuel cell membrane electrode assemblies, J. Power Sources 220 (2012) 348-353.

[212] M. Hunsom, D. Kaewsai, A.M. Kannan, Recent developments in bifunctional air electrodes for unitized regenerative proton exchange membrane fuel cells – A review, Int. J. Hydrogen Energ. 43 (2018) 21478-21501.

[213] Y. Wang, D.Y.C. Leung, J. Xuan, H. Wang, A review on unitized regenerative fuel cell technologies, part-A: Unitized regenerative proton exchange membrane fuel cells, Renew. Sust. Energ. Rev. 65 (2016) 961-977.

[214] Y. Li, J. Yang, J. Song, Structure models and nano energy system design for proton exchange membrane fuel cells in electric energy vehicles, Renew. Sust. Energ. Rev. 67 (2017) 160-172.

[215] C. Qin, J. Wang, D. Yang, B. Li, C. Zhang, Proton exchange membrane fuel cell reversal: A review, Catalysts 6 (2016) 197.

[216] D. Banham, S. Ye, K. Pei, J. Ozaki, T. Kishimoto, Y. Imashiro, A review of the stability and durability of non-precious metal catalysts for the oxygen reduction reaction in proton exchange membrane fuel cells, J. Power Sources 285 (2015) 334-348.

[217] L. Lu, H. Xu, J. Shi, S. Zhu, H. Zhao, G. Wang, Pt-supported C–MnO_2 as a catalyst for polymer

electrolyte membrane fuel cells, J. Appl. Electrochem. 48 (2018) 801-810.

[218] P. Trogadas, V. Ramani, Pt/C/MnO_2 hybrid electrocatalysts for degradation mitigation in polymer electrolyte fuel cells, J. Power Sources 174 (2007) 159-163.

[219] M. Lei, T.Z. Yang, W.J. Wang, K. Huang, Y.C. Zhang, R. Zhang, R.Z. Jiao, X.L. Fu, H.J. Yang, Y.G. Wang, W.H. Tang, One-dimensional manganese oxide nanostructures as radical scavenger to improve membrane electrolyte assembly durability of proton exchange membrane fuel cells, J. Power Sources 230 (2013) 96-100.

[220] Z.D. Wei, M.B. Ji, Y. Hong, C.X. Sun, S.H. Chan, P.K. Shen, MnO_2–Pt/C composite electrodes for preventing voltage reversal effects with polymer electrolyte membrane fuel cells, J. Power Sources 160 (2006) 246-251.

[221] A.L. Goff, V. Artero, B. Jousselme, P.D. Tran, N. Guillet, R. Metaye, A. Fihri, S. Palacin, M. Fontecave, From hydrogenases to noble metal–free catalytic nanomaterials for H_2 production and uptake, Science 326 (2009) 1384-1387.

[222] I. Roger, M.A. Shipman, M.D. Symes, Earth-abundant catalysts for electrochemical and photoelectrochemical water splitting, Nat. Rev. Chem. 1 (2017) 0003.

[223] W. Zhong, Z. Wang, N. Gao, L. Huang, Z. Lin, Y. Liu, F. Meng, J. Deng, S. Jin, Q. Zhang, L. Gu, Coupled vacancy pairs in Ni-Doped CoSe for improved electrocatalytic hydrogen production through topochemical deintercalation, Angew. Chem. Int. Ed. 59 (2020) 22743-22748.

[224] M. Jamesh, X. Sun, Recent progress on earth abundant electrocatalysts for oxygen evolution reaction (OER) in alkaline medium to achieve efficient water splitting – A review, J. Power Sources 400 (2018) 31-68.

[225] C. Hu, L. Zhang, J. Gong, Recent progress made in the mechanism comprehension and design of electrocatalysts for alkaline water splitting, Energ. Environ. Sci. 12 (2019) 2620-2645.

[226] M.I. Jamesh, Recent progress on earth abundant hydrogen evolution reaction and oxygen evolution reaction bifunctional electrocatalyst for overall water splitting in alkaline media, J. Power Sources 333 (2016) 213-236.

[227] F. Jing, Q. Lv, J. Xiao, Q. Wang, S. Wang, Highly active and dual-function self-supported multiphase NiS–NiS_2–Ni_3S_2/NF electrodes for overall water splitting, J. Mater. Chem. A 6 (2018) 14207-14214.

[228] Y. Kuang, M.J. Kenney, Y. Meng, W.H. Hung, Y. Liu, J.E. Huang, R. Prasanna, P. Li, Y. Li, L. Wang, Solar-driven, highly sustained splitting of seawater into hydrogen and oxygen fuels, P. Natl. Acad. Sci. USA 116 (2019) 6624-6629.

[229] C. Kuo, I.M. Mosa, A.S. Poyraz, S. Biswas, A.M. Elsawy, W. Song, Z. Luo, S. Chen, J.F. Rusling, J. He, Robust mesoporous manganese oxide catalysts for water oxidation, ACS Catal. 5 (2015) 1693-1699.

[230] J.H. Zhang, J.Y. Feng, T. Zhu, Z.L. Liu, Q.Y. Li, S.Z. Chen, C.W. Xu, Pd-doped urchin-like MnO_2-carbon sphere three-dimensional (3D) material for oxygen evolution reaction, Electrochim. Acta 196 (2016) 661-669.

[231] H. Antoni, D.M. Morales, J. Bitzer, Q. Fu, Y. Chen, J. Masa, W. Kleist, W. Schuhmann, M. Muhler, Enhancing the water splitting performance of cryptomelane-type α-(K)MnO_2, J. Catal. 374 (2019) 335-344.

[232] W. Yuan, P.K. Shen, S.P. Jiang, Controllable synthesis of graphene supported MnO_2 nanowires via self-assembly for enhanced water oxidation in both alkaline and neutral solutions, J. Mater. Chem. A 2 (2014) 123-129.

[233] M. Wiechen, I. Zaharieva, H. Dau, P. Kurz, Layered manganese oxides for water-oxidation: alkaline earth cations influence catalytic activity in a photosystem II-like fashion, Chem. Sci. 3 (2012) 2330-2339.

[234] Q. Kang, L. Vernisse, R.C. Remsing, A.C. Thenuwara, S.L. Shumlas, I.G. Mckendry, M.L. Klein, E. Borguet, M.J. Zdilla, D.R. Strongin, Effect of interlayer spacing on the activity of layered manganese oxide bilayer catalysts for the oxygen evolution reaction, J. Am. Chem. Soc. 139 (2017) 1863-1870.

[235] A.C. Thenuwara, E.B. Cerkez, S.L. Shumlas, N.H. Attanayake, I.G. Mckendry, L. Frazer, E. Borguet, Q. Kang, R.C. Remsing, M.L. Klein, Nickel confined in the interlayer region of birnessite: An active electrocatalyst for water oxidation, Angew. Chem. Int. Edit. 55 (2016) 10381-10385.

[236] S. Dresp, F. Dionigi, M. Klingenhof, P. Strasser, Direct electrolytic splitting of seawater: Opportunities and challenges, ACS Energy Lett. 4 (2019) 933-942.

[237] P. Li, R. Zhao, H. Chen, H. Wang, P. Wei, H. Huang, Q. Liu, T. Li, X. Shi, Y. Zhang, Recent advances in the development of water oxidation electrocatalysts at mild pH, Small 15 (2019) 1805103.

[238] F. Lyu, Q. Wang, S.M. Choi, Y. Yin, Noble-metal-free electrocatalysts for oxygen evolution, Small 15 (2019) 1804201.

[239] J. Wang, F. Xu, H. Jin, Y. Chen, Y. Wang, Non-noble metal-based carbon composites in hydrogen evolution reaction: Fundamentals to applications, Adv. Mater. 29 (2017) 1605838.

[240] M.W. Kanan, D.G. Nocera, In situ formation of an oxygen-evolving catalyst in neutral water containing phosphate and Co^{2+}, Science 321 (2008) 1072-1075.

[241] A. Ramirez, P. Hillebrand, D. Stellmach, M.M. May, P. Bogdanoff, S. Fiechter, Evaluation of MnOx, Mn_2O_3, and Mn_3O_4 electrodeposited films for the oxygen evolution reaction of water, J. Phys. Chem. C 118 (2014) 14073-14081.

[242] Y.H. Lee, S. Park, K.G. Lee, M.Y. Lee, K.H. Cho, S.J. Kim, K.T. Nam, Methylamine treated Mn_3O_4 nanoparticles as a highly efficient water oxidation catalyst under neutral condition, Chemcatchem 11 (2019) 1665-1672.

[243] K.H. Cho, H. Seo, S. Park, Y.H. Lee, M.Y. Lee, N.H. Cho, K. Nam, Uniform, assembled 4 nm Mn_3O_4 nanoparticles as efficient water oxidation electrocatalysts at neutral pH, Adv. Funct. Mater. 30 (2020) 1910424.

[244] A. Indra, P.W. Menezes, I. Zaharieva, E. Baktash, J. Pfrommer, M. Schwarze, H. Dau, M. Driess, Active mixed-valent MnOx water oxidation catalysts through partial oxidation (corrosion) of nanostructured MnO particles, Angew. Chem. Int. Edit. 52 (2013) 13206-13210.

[245] K. Jin, H. Seo, T. Hayashi, M. Balamurugan, D. Jeong, Y.K. Go, J.S. Hong, K.H. Cho, H. Kakizaki, N. Bonnet-Mercier, M.G. Kim, S.H. Kim, R. Nakamura, K.T. Nam, Mechanistic investigation of water oxidation catalyzed by uniform, assembled MnO nanoparticles, J. Am. Chem. Soc. 139 (2017) 2277-2285.

[246] D. Jeong, K. Jin, S.E. Jerng, H. Seo, D. Kim, S.H. Nahm, S.H. Kim, K. Nam, Mn_5O_8 nanoparticles as efficient water oxidation catalysts at neutral pH, ACS Catal. 5 (2015) 4624-4628.

[247] T. Takashima, K. Hashimoto, R. Nakamura, Mechanisms of pH-dependent activity for water oxidation to molecular oxygen by MnO_2 electrocatalysts, J. Am. Chem. Soc. 134 (2012) 1519-1527.

[248] A. Yamaguchi, R. Inuzuka, T. Takashima, T. Hayashi, K. Hashimoto, R. Nakamura, Regulating

proton-coupled electron transfer for efficient water splitting by manganese oxides at neutral pH, Nat. Commun. 5 (2014) 4256-4256.

[249] H. Jin, J. Joo, N.K. Chaudhari, S.-I. Choi, K. Lee, Recent progress in bifunctional electrocatalysts for overall water splitting under acidic conditions, Chemelectrochem 6 (2019) 3244-3253.

[250] C. Spori, J.T.H. Kwan, A. Bonakdarpour, D.P. Wilkinson, P. Strasser, The stability challenges of oxygen evolving catalysts: Towards a common fundamental understanding and mitigation of catalyst degradation, Angew. Chem. Int. Edit. 56 (2017) 5994-6021.

[251] C. Wei, R.R. Rao, J. Peng, B. Huang, I.E.L. Stephens, M. Risch, Z.J. Xu, Y. Shao-Horn, Recommended practices and benchmark activity for hydrogen and oxygen electrocatalysis in water splitting and fuel cells, Adv. Mater. 31 (2019) e1806296.

[252] J. Zheng, W. Sheng, Z. Zhuang, B. Xu, Y. Yan, Universal dependence of hydrogen oxidation and evolution reaction activity of platinum-group metals on pH and hydrogen binding energy, Sci. Adv. 2 (2016) 1501602.

[253] K. Sardar, E. Petrucco, C.I. Hiley, J.D.B. Sharman, P.P. Wells, A.E. Russell, R.J. Kashtiban, J. Sloan, R.I. Walton, Water-splitting electrocatalysis in acid conditions using ruthenate-iridate pyrochlores, Angew. Chem. Int. Edit. 53 (2014) 10960-10964.

[254] J.G. Vos, T.A. Wezendonk, A.W. Jeremiasse, M.T.M. Koper, MnOx/IrOx as selective oxygen evolution electrocatalyst in acidic chloride solution, J. Am. Chem. Soc. 140 (2018) 10270-10281.

[255] M. Huynh, D.K. Bediako, D.G. Nocera, A functionally stable manganese oxide oxygen evolution catalyst in acid, J. Am. Chem. Soc. 136 (2014) 6002-6010.

[256] M. Huynh, C. Shi, S.J.L. Billinge, D.G. Nocera, Nature of activated manganese oxide for oxygen evolution, J. Am. Chem. Soc. 137 (2015) 14887-14904.

[257] A. Li, H. Ooka, N. Bonnet, T. Hayashi, Y. Sun, Q. Jiang, C. Li, H. Han, R. Nakamura, Stable potential windows for long-term electrocatalysis by manganese oxides under acidic conditions, Angew. Chem. Int. Edit. 58 (2019) 5054-5058.

[258] M. Huynh, T. Ozel, C. Liu, E.C. Lau, D.G. Nocera, Design of template-stabilized active and earth-abundant oxygen evolution catalysts in acid, Chem. Sci. 8 (2017) 4779-4794.

[259] M.M. Najafpour, K.C. Leonard, F.F. Fan, M.A. Tabrizi, A.J. Bard, C.K. Kingondu, S.L. Suib, B. Haghighi, S.I. Allakhverdiev, Nano-size layered manganese–calcium oxide as an efficient and biomimetic catalyst for water oxidation under acidic conditions: comparable to platinum, Dalton Trans. 42 (2013) 5085-5091.

[260] S.M. Hwang, J. Park, Y. Kim, W. Go, J. Han, Y. Kim, Y. Kim, Rechargeable seawater batteries—from concept to applications, Adv. Mater. 31 (2019) 1804936.

Table captions

Table 1: Comparison of electrochemical properties of the different manganese dioxides as oxygen catalysts.

Table 2: Electrode reactions of the various metal-air batteries, fuel cells and water splitting systems.

Figure captions

Figure 1: Oxygen reduction reaction (ORR) mechanisms: a) the adsorbate evolution mechanism (AEM). b) the lattice-oxygen participated mechanism (LOM). Reproduced with permission [11]. Copyright 2021, Royal Society of Chemistry. c) the dual-site mechanism. Reproduced with permission [14]. Copyright 2019, American Chemical Society. Oxygen evolution reaction (OER) mechanisms: d) the adsorbate evolution mechanism (AEM). e) the lattice-oxygen participated mechanism (LOM). Reproduced with permission [18]. Copyright 2020, Royal Society of Chemistry. f) the dual-site mechanism. Reproduced with permission [19]. Copyright 2021, American Chemical Society.

Figure 2: Schematic diagrams of [MnO_6] octahedron and various crystal structures of MnO_2. a) [MnO_6] octahedron, b) α-MnO_2, c) β-MnO_2, d) γ-MnO_2, e) δ-MnO_2, and f) λ-MnO_2, respectively.

Figure 3: a) Mechanism of OER catalyzed by MnO_2 in near-neutral media. Reproduced with permission [68]. Copyright 2020, John Wiley and Sons. b) Mechanism for the OER as mediated by manganese oxides under acidic conditions. DISP=disproportionation. c) Illustration of the current density (j) vs. potential curve for MnO_2 at neutral pH. The surface-associated disproportionation reaction of intermediate Mn^{3+} species. Reproduced with permission [69]. Copyright 2016, Royal Society of Chemistry.

Figure 4: a) Schematic illustration of the synthesis of the α-MnO_2 nanowires by using ionic liquid as the structure-directing agent. b) Field emission scanning electron

microscopy (FESEM) and c) high resolution transmission electron microscopy (HRTEM) of MnO_2-0.5IL. d) Linear sweep voltammetry (LSV) curves for OER at a scan rate of 5 mV s^{-1} in 1 M KOH. e) Tafel plots for OER in 1 M KOH. Reproduced with permission [79]. Copyright 2018, American Chemical Society. f) FESEM image, g) TEM image and h) HRTEM image of dandelion-like α-MnO_2. i) FESEM image, j) TEM image and k) HRTEM image of urchin-like α-MnO_2. l) ORR performances of samples in 0.1 M KOH electrolyte at a scan rate of 5 mV s^{-1} and a rotating speed of 1600 rpm. m) LSVs for OER of dandelion-like and urchin-like α-MnO_2 at a scan rate of 5 mV s^{-1} in 0.1 M KOH and n) the corresponding Tafel plots. Reproduced with permission [80]. Copyright 2017, Elsevier.

Figure 5: The applications of MnO_2 in the various MABs, FCs and WSSs with the different electrolytes.

Figure 6: a)~b) SEM images with different magnification of the manganese oxide grown on the carbon paper. c) Galvanodynamic charge and discharge polarization curves of ZAB with MnO_2 directly grown on the carbon paper. Reproduced with permission [135]. Copyright 2015, John Wiley and Sons. d)~e) SEM images of MnO_x grown on carbon cloth (MnO_x-CC) and graphene-coated on treated carbon cloth (GCC). f) Galvanodynamic discharge and charge polarization curves of ZAB with various carbon cloth-based air cathodes. Reproduced with permission [136]. Copyright 2017, John Wiley and Sons. g) SEM images of MnO_x grown on carbon cloth and subsequently annealed at 400 ^oC for 1 h. h) HR-TEM images of MnO_x-CC-400. i) Galvanodynamic charge and discharge polarization curves of the

ZAB with air cathodes of Pt/C-RuO_2-CC and MnO_x-CC samples. Reproduced with permission [137]. Copyright 2019, Royal Society of Chemistry.

Figure 7: a) SEM image and b)~c) TEM images of RGO-MnO_2 at various magnifications. d) Linear sweep voltammogram (LSV) curves of RGO-MnO_2 in nitrogen- and oxygen-saturated 0.1 M KOH at a scan rate of 0.5 mV s^{-1}. e) Current density-time chronoamperometric responses of Pt/XC-72 and RGO-MnO_2 electrodes at -0.3 V in oxygen-saturated 0.1M KOH. Rotating speed, 2000 rpm. The arrow indicates the addition of methanol into the electrochemical cell. Reproduced with permission [183]. Copyright 2013, Royal Society of Chemistry. f) Schematic illustration of the preparation of oxygen-deficient MnO_2 nanoparticles by proton beam irradiation. g) LSVs of MnO_2 prepared under 14 MeV proton irradiation and different experimental conditions in O_2-saturated 0.1 M KOH at 1600 rpm with a sweep rate of 5 mV s^{-1}. h) Methanol-crossover tests performed by adding methanol into the electrolyte at 2000 s. All measurements were performed at applied voltage of 0.6 V vs. RHE. Reproduced with permission [189]. Copyright 2019, Royal Society of Chemistry.

Figure 8: a) Schematic showing the *in situ* growth of ultrathin δ-MnO_2 nanosheets on an Ni foam (NS-MnO_2). b) SEM image of NS-MnO_2. c) HRTEM image of δ-MnO2 nanosheets (the inset shows the SAED pattern). d) Linear sweep voltammetry (LSV) curves for OER at a scan rate of 5 mV s^{-1} in 1 M KOH. e) Tafel plots for OER in 1 M KOH. f) Current density versus time (I-t) curves of HER and OER for NS-MnO_2. Reproduced with permission [89]. Copyright 2017, John Wiley and Sons. g)

Schematic illustration of the synthetic process of Ni-Fe-K0.23MnO2 CNFs-300. h) FESEM, i) TEM and j) HRTEM images of Ni-Fe-$K_{0.23}MnO_2$ CNFs-300. LSV curves of Ni-Fe-$K_{0.23}MnO_2$ CNFs-300 toward OER k) and HER l). m) Polarization curves of the Ni-Fe-$K_{0.23}MnO_2$ CNFs-300||Ni-Fe-$K_{0.23}MnO_2$ CNFs-300 cell for overall water splitting. Reproduced with permission [75]. Copyright 2020, John Wiley and Sons.

Table 1

Table 1. Comparison of electrochemical properties of the different manganese dioxides as oxygen catalysts.

Part	Samples	Structures	$E_{1/2}$ [V vs. RHE]	ORR Tafel slope [mV dec^{-1}]	$E_{j=10}$ [V vs. RHE]	OER Tafel slope [mV dec^{-1}]	Electrolytes	Ref.
Section 2.3	MnO_2	α-MnO_2	~0.68	--	> 1.96	85	0.1 M KOH	[72]
	0.022 FeMn	α-MnO_2	~0.69	--	1.89	58	0.1 M KOH	[72]
	birnessite	δ-MnO_2	--	--	2.01	240	1 M KOH	[73]
	$K_{0.01}[Co_{0.30}Mn_{0.70}O_2]$	δ-MnO_2	--	--	1.66	81	1.0 M KOH	[73]
	A-CoMnO	Amorphous	--	--	1.57	62	1.0 M KOH	[74]
	Ni-Fe-$K_{0.23}MnO_2$ CNFs-300	δ-MnO_2	--	--	1.50	42.3	1.0 M KOH	[75]
	MnO_2-0IL	β-MnO_2	--	--	1.80	124	1.0 M KOH	[79]
	MnO_2-0.5IL	α-MnO_2	--	--	1.62	49	1.0 M KOH	[79]
	MnO_2-0.5IL	α-MnO_2	--	--	2.17	220	pH = 7.0	[79]
	dandelion-like α-MnO_2	α-MnO_2	0.74	56	1.78	155	0.1 M KOH	[80]
	urchin-like α-MnO_2	α-MnO_2	0.72	59	1.87	210	0.1 M KOH	[80]
	MnO_2	Amorphous	--	--	~1.72	70	1.0 M KOH	[82]
	MnO_2	Amorphous	--	--	>1.80	170	0.05 M H_2SO_4	[82]
	Ti-MnO_2	Amorphous	--	--	>1.80	~70	0.05 M H_2SO_4	[82]
	MnO_2/CC	δ-MnO_2	--	--	~1.76	173	1.0 M KOH	[83]
	Fe-Mn-O NSs/CC	δ-MnO_2	--	--	1.50	64	1.0 M KOH	[83]
	γ-MnO_2	γ-MnO_2	0.68	274	>1.80	152	0.1 M KOH	[84]
	NiO/MnO_2	γ-MnO_2	0.7	197	1.62	51	0.1 M KOH	[84]
	NiO/MnO_2 @PANI	γ-MnO_2	0.83	124	1.58	42	0.1 M KOH	[84]
	Co_3O_4/MnO_2	α-MnO_2	~0.57	--	~1.92	--	0.1 M KOH	[85]
	Co_3O_4/MnO_2/PQ-7	α-MnO_2	~0.88	--	~1.80	--	0.1 M KOH	[85]
	MnO_x/CFP	δ-MnO_2	--	--	~1.80	135	Phosphate, pH =2.5	[87]
	MnO_x/CFP	δ-MnO_2	--	--	~1.77	110	Phosphate, pH =7	[87]
	MnO_x/CFP	δ-MnO_2	--	--	~1.68	55	Phosphate, pH =12	[87]
	MnO_2/C	α, β-MnO_2	0.67	118	1.75	150	0.1 M KOH	[88]
	MnO_2/$NRGO_{-Urea}$	α, β-MnO_2	0.80	78	1.69	95	0.1 M KOH	[88]
	NS-MnO_2	δ-MnO_2	--	--	1.55	40	1.0 M KOH	[89]
	α-MnO_2-80	α-MnO_2	~0.80	--	--	--	0.1 M KOH	[90]
	1050MO	λ-MnO_2	~0.67	120	--	--	0.1 M KOH	[93]
	MO	α-MnO_2	~0.62	79	--	--	1.0 M KOH	[59]
	MO400	α-MnO_2	~0.68	65	--	--	1.0 M KOH	[59]
	MnO_2-3	α-MnO_2	0.83	--	--	--	0.1 M KOH	[96]
	Ag/MnO_2-3	α-MnO_2	0.87	--	--	--	0.1 M KOH	[96]
	MnO_2-IL_0	α-MnO_2	0.74	--	1.62	55	0.1 M KOH	[58]
	MnO_2-$IL_{0.5}$	α-MnO_2	0.83	--	1.80	120	0.1 M KOH	[58]
	α-MnO_2 NWs	α-MnO_2	--	--	1.67	58	0.1 M KOH	[98]
	MnOOH@$CDs_{0.2}$	α-MnO_2	--	--	1.532	51.3	1 M KOH	[99]
	ammo@MnO_2	δ-MnO_2	--	--	1.462	36.0	1 M KOH	[86]
	MnO_2@mpg-C_3N_4	α-MnO_2	--	--	--	90	0.066 M phosphate buffer (pH 7)	[100]
	Ni/DMTD/MnO_2	α-MnO_2	--	--	1.492	69.46	1 M KOH	[101]
	Co-MnO_2|O_V	--	--	--	1.509	75	1 M KOH	[76]

	Co/MnO_2	δ-MnO_2	--	--	--	60	1 M KOH	[102]
	MnO_2-CoP_3/Ti	--	--	--	1.518	65	1 M KOH	[103]
	$MnO_2/NiCo_2O_4$/NF	Amorphous	--	--	1.57	139	1 M KOH	[104]
	metal-ion-doped MnO_2/CFP	γ-MnO_2	--	--	1.62	104.4	1 M KOH	[105]
	IrO_2@Mn-5	α-MnO_2	--	--	1.505	59	0.1 M $HClO_4$	[106]
	MnOx/ GR	--	--	--	--	58	0.1 M KOH	[107]
	PMOP	β-MnO_2	--	--	1.68	78.2	1 M KOH	[108]
	MnOx-450℃	--	--	--	1.617	~70	1 M NaOH	[109]
	CMT@N-RGO/ MnO_2	δ-MnO_2	0.788	--	--	--	0.1 M KOH	[110]
	Co_3O_4/MnO_2	α-MnO_2	0.786	--	--	--	0.1 M KOH	[111]
	MnO_2/CZIF-67	α-MnO_2	0.79	--	--	--	0.1 M KOH	[112]
	δ-MnO_2/SGS	δ-MnO_2	0.8	--	--	--	0.1 M KOH	[113]
	C-MnO_2 NWs	α-MnO_2	0.75	--	--	--	0.1 M KOH	[114]
	$NiMnO_2$-4.9	α-MnO_2	0.70	61	--	--	0.1 M KOH	[115]
	3D MnO_2	α-MnO_2	0.72	--	--	--	0.1 M KOH	[116]
	CNT-graphene-α-MnO_2	α-MnO_2	0.855	67	--	--	0.1 M KOH	[117]
	MnO_2/N-HGSs	--	0.84	--	--	--	0.1 M KOH	[118]
	ε-MnO_2/MOF(Fe)	ε-MnO_2	0.64	117	--	--	0.1 M KOH	[119]
Section 3.3	α-(K)MnO_2 (H_2O/He)	α-MnO_2	--	--	1.677	49.8	1.0 M KOH	[231]
	α-(K)MnO_2 (He)	α-MnO_2	--	--	1.681	55.2	1.0 M KOH	[231]
	NS-MnO_2	δ-MnO_2	--	--	1.550	40.0	1.0 M KOH	[89]
	NS/Cs^+/NS	δ-MnO_2	--	--	1.990	101.3	1.0 M KOH	[234]
	$K_{0.01}[Co_{0.30}Mn_{0.70}O_2]$	δ-MnO_2	--	--	1.655	81.0	1.0 M KOH	[73]
	$K_{0.04}[Co_{0.42}Mn_{0.58}O_2]$	δ-MnO_2	--	--	1.680	110.0	1.0 M KOH	[73]
	7.7% Ni^{2+}/birnessite	δ-MnO_2	--	--	1.630	60.0	1.0 M KOH	[235]
	6.5% Ni^{2+}/birnessite	δ-MnO_2	--	--	1.630	65.0	1.0 M KOH	[235]
	Ni-Fe-$K_{0.23}MnO_2$ CNFs-300	δ-MnO_2	--	--	1.500	42.3	1.0 M KOH	[75]
	Ni-Fe-$K_{0.23}MnO_2$ CNFs	δ-MnO_2	--	--	1.532	54.2	1.0 M KOH	[75]
	$K_{0.23}MnO_2$ NS	δ-MnO_2	--	--	1.585	120.1	1.0 M KOH	[75]
	Activated MnO_x	δ-MnO_2	--	--	--	91.0	0.10 M Pi + 1.90 M KNO_3, PH=2.5	[256]
	constant potential deposited MnO_x	δ-MnO_2	--	--	--	650.0	0.10 M Pi + 1.90 M KNO_3, PH=2.5	[256]
	γ-MnO_2 on FTO	γ-MnO_2	--	--	1.719	79.0	1.0M H_2SO_4	[257]
	γ-MnO_2 on carbon paper	γ-MnO_2	--	--	1.658	80.0	1.0M H_2SO_4	[257]
	$CoMnO_x$	δ-MnO_2	--	--	--	83.0	0.10 M Pi + 1.0 M KNO_3, PH=2.5	[258]
	Ti-MnO_2	amorphous	--	--	--	170.0	0.05 M H_2SO_4	[82]
	MnO_x/IrO_x	δ-MnO_2	--	--	--	43.0	0.5 M Na/$HClO_4$, pH=0.85	[254]

Table 2

Table 2. Electrode reactions of the various metal-air batteries, fuel cells and water splitting systems.

Electrochemical systems	Electrochemical devices	Working mode	Electrode reactions
Metal-air batteries	Zn-air battery (ZABs)	Discharge	**Anode:** $Zn + OH^- = Zn(OH)_4^{2-} + 2e^-$ $Zn(OH)_4^{2-} = ZnO + H_2O + 2OH^-$ **Cathode:** $O_2 + H_2O + 4e^- = 4OH^-$ **Overall:** $2Zn + O_2 = 2ZnO$
		Charge	**Anode:** $4OH^- = O_2 + H_2O + 4e^-$ **Cathode:** $ZnO + H_2O + 2OH^- = Zn(OH)_4^{2-}$ $Zn(OH)_4^{2-} + 2e^- = Zn + OH^-$ **Overall:** $2ZnO = 2Zn + O_2$
	Al-air battery (AABs)	Discharge	**Anode:** $Al + 3OH^- = Al(OH)_3 + 3e^-$ **Cathode:** $O_2 + H_2O + 4e^- = 4OH^-$ **Overall:** $4Al + 3O_2 + 6H_2O = 4\ Al(OH)_3$
	Mg-air battery (MgABs)	Discharge	**Anode:** $2Mg + 4OH^- = 2Mg(OH)_2 + 4e^-$ **Cathode:** $O_2 + H_2O + 4e^- = 4OH^-$ **Overall:** $2Mg + O_2 + 2H_2O = 2Mg(OH)_2$
Fuel cells	Alkaline fuel cells (AFCs)	Fuel cell	**Anode:** $H_2 + 2OH^- = 2H_2O + 2e^-$ **Cathode:** $2H_2O + O_2 + 4e^- = 4OH^-$ **Overall:** $2H_2 + O_2 = H_2O$
		Electrolyzer	**Anode:** $4OH^- = 2H_2O + O_2 + 4e^-$ **Cathode:** $2H_2O + 2e^- = H_2 + 2OH^-$ **Overall:** $H_2O = 2H_2 + O_2$
	Direct methanol fuel cells (DMFCs)	Fuel cell	**Anode:** $CH_3OH + H_2O = CO_2 + 6H^+ + 6e^-$ **Cathode:** $3/2O_2 + 6H^+ + 6e^- = 3H_2O$ **Overall:** $CH_3OH + 3/2O_2 = CO_2 + 2H_2O$
	Microbial fuel cells (MFCs)	Fuel cell	**Anode:** $CH_3COO^- + 4H_2O = 2HCO_3^- + 9H^+ + 8e^-$ (using acetate as a fuel source) **Cathode:** $O_2 + 4H^+ + 4e^- = 2H_2O$ **Overall:** $CH_3COO^- + 2O_2 = 2HCO_3^- + H^+$
	Proton exchange membrane fuel cells (PEMFCs)	Fuel cell	**Anode:** $2H_2 = 4H^+ + 2e^-$ **Cathode:** $4H^+ + O_2 + 2e^- = 2H_2O$ **Overall:** $2H_2 + O_2 = H_2O$
		Electrolyzer	**Anode:** $2H_2O = 4H^+ + O_2 + 2e^-$ **Cathode:** $4H^+ + 2e^- = 2H_2$ **Overall:** $H_2O = 2H_2 + O_2$
Water splitting systems	Alkaline water splitting	Electrolyzer	Same with electrolyzer mode of AFCs
	Neutral water splitting	Electrolyzer	Same with electrolyzer mode of AFCs
	Acidic water splitting	Electrolyzer	Same with electrolyzer mode of PEMFCs

Figure 1

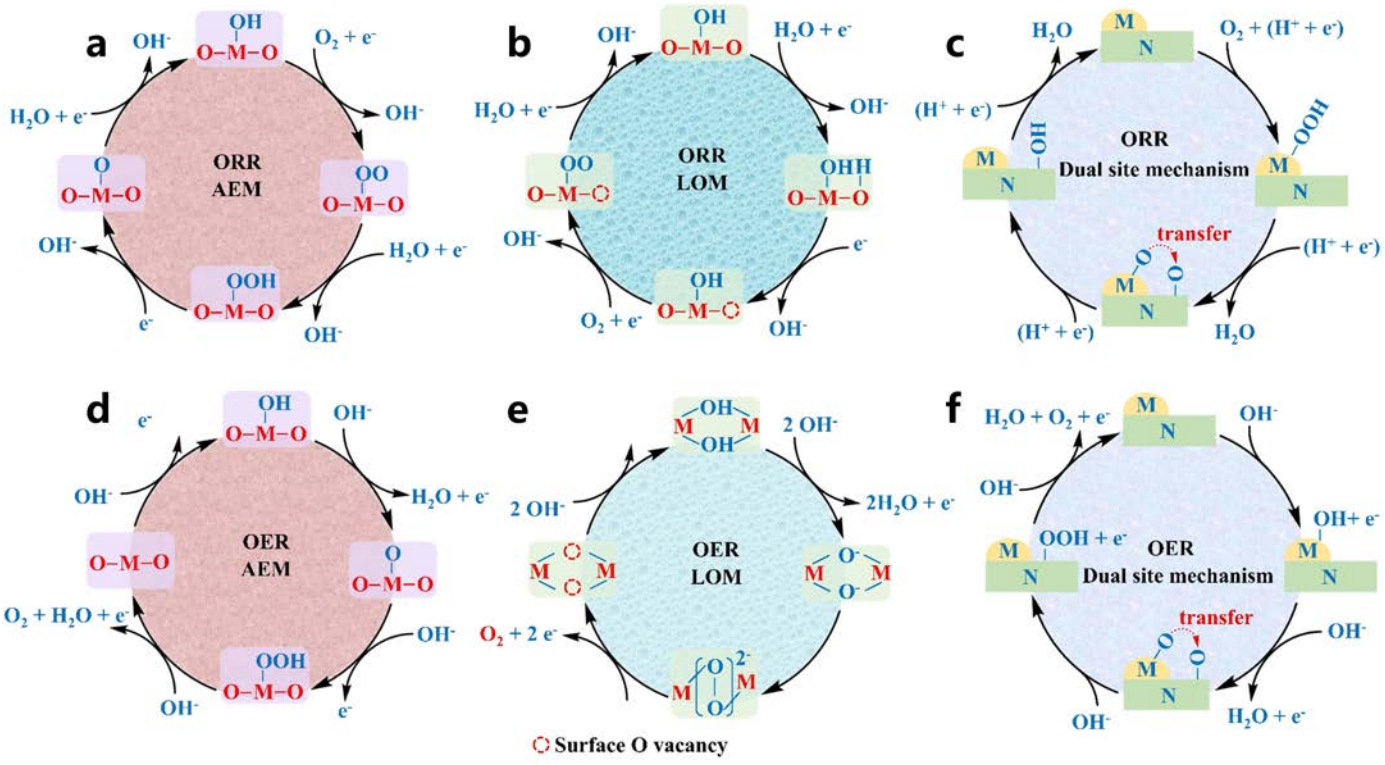

Fig. 1. Oxygen reduction reaction (ORR) mechanisms: a) the adsorbate evolution mechanism (AEM). b) the lattice-oxygen participated mechanism (LOM). Reproduced with permission [11]. Copyright 2021, Royal Society of Chemistry. c) the dual-site mechanism. Reproduced with permission [14]. Copyright 2019, American Chemical Society. Oxygen evolution reaction (OER) mechanisms: d) the adsorbate evolution mechanism (AEM). e) the lattice-oxygen participated mechanism (LOM). Reproduced with permission [18]. Copyright 2020, Royal Society of Chemistry. f) the dual-site mechanism. Reproduced with permission [19]. Copyright 2021, American Chemical Society.

Figure 2

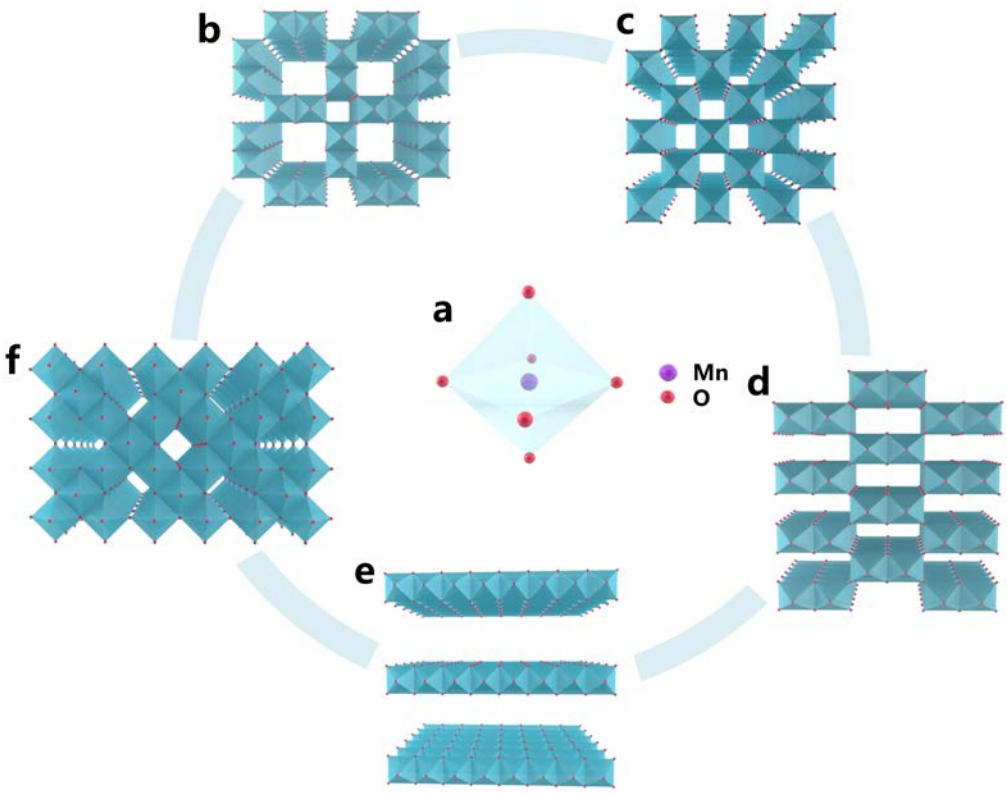

Fig. 2. Schematic diagrams of [MnO_6] octahedron and various crystal structures of MnO_2. a) [MnO_6] octahedron, b) α-MnO_2, c) β-MnO_2, d) γ-MnO_2, e) δ-MnO_2, and f) λ-MnO_2, respectively.

Figure 3

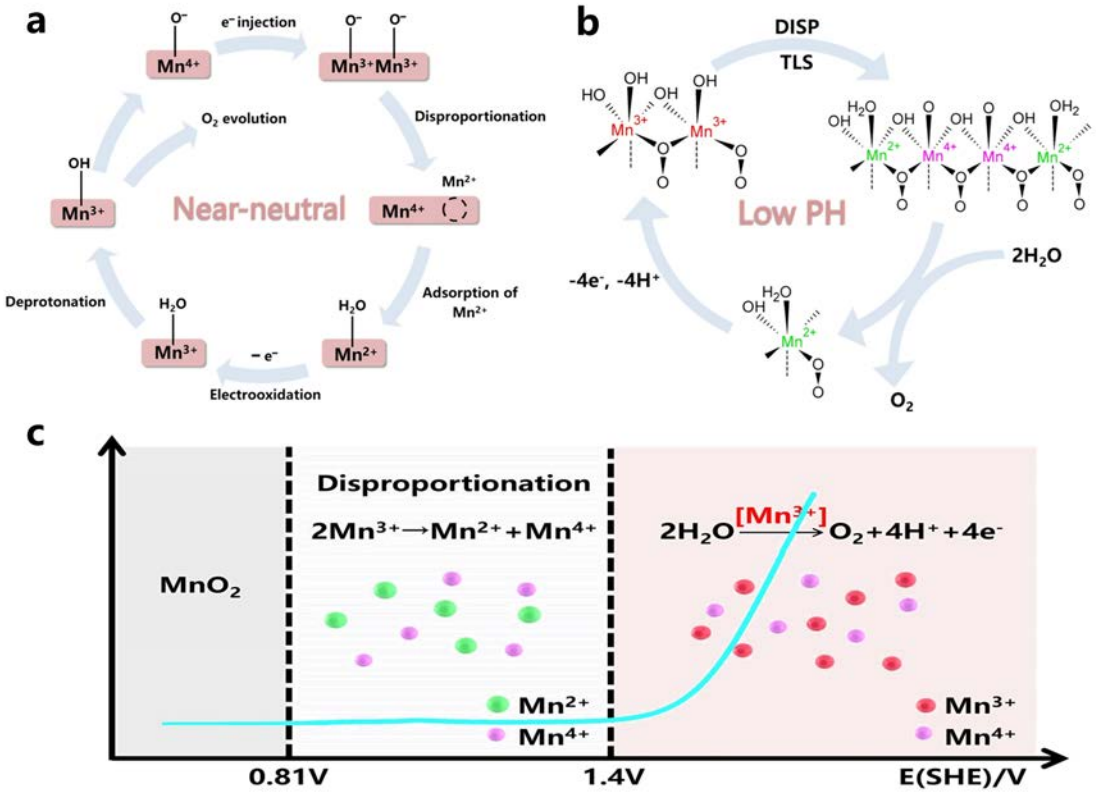

Fig. 3. a) Mechanism of OER catalyzed by MnO_2 in near-neutral media. Reproduced with permission [68]. Copyright 2020, John Wiley and Sons. b) Mechanism for the OER as mediated by manganese oxides under acidic conditions. DISP=disproportionation. c) Illustration of the current density (j) vs. potential curve for MnO_2 at neutral pH. The surface-associated disproportionation reaction of intermediate Mn^{3+} species. Reproduced with permission [69]. Copyright 2016, Royal Society of Chemistry.

Figure 4

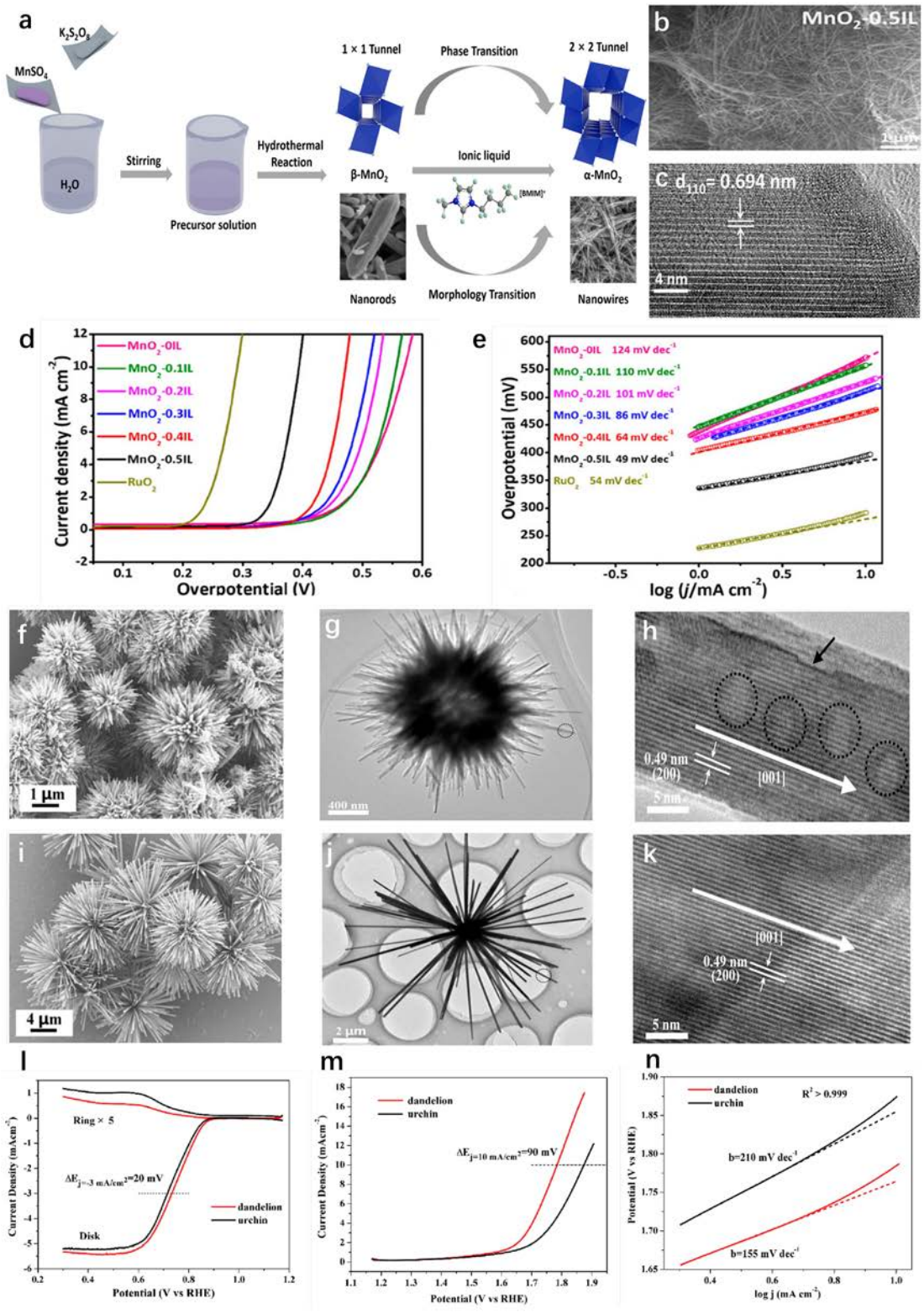

Fig. 4. a) Schematic illustration of the synthesis of the α-MnO_2 nanowires by using ionic liquid as the structure-directing agent. b) Field emission scanning electron

microscopy (FESEM) and c) high resolution transmission electron microscopy (HRTEM) of MnO_2-0.5IL. d) Linear sweep voltammetry (LSV) curves for OER at a scan rate of 5 mV s^{-1} in 1 M KOH. e) Tafel plots for OER in 1 M KOH. Reproduced with permission [79]. Copyright 2018, American Chemical Society. f) FESEM image, g) TEM image and h) HRTEM image of dandelion-like α-MnO_2. i) FESEM image, j) TEM image and k) HRTEM image of urchin-like α-MnO_2. l) ORR performances of samples in 0.1 M KOH electrolyte at a scan rate of 5 mV s^{-1} and a rotating speed of 1600 rpm. m) LSVs for OER of dandelion-like and urchin-like α-MnO_2 at a scan rate of 5 mV s^{-1} in 0.1 M KOH and n) the corresponding Tafel plots. Reproduced with permission [80]. Copyright 2017, Elsevier.

Figure 5

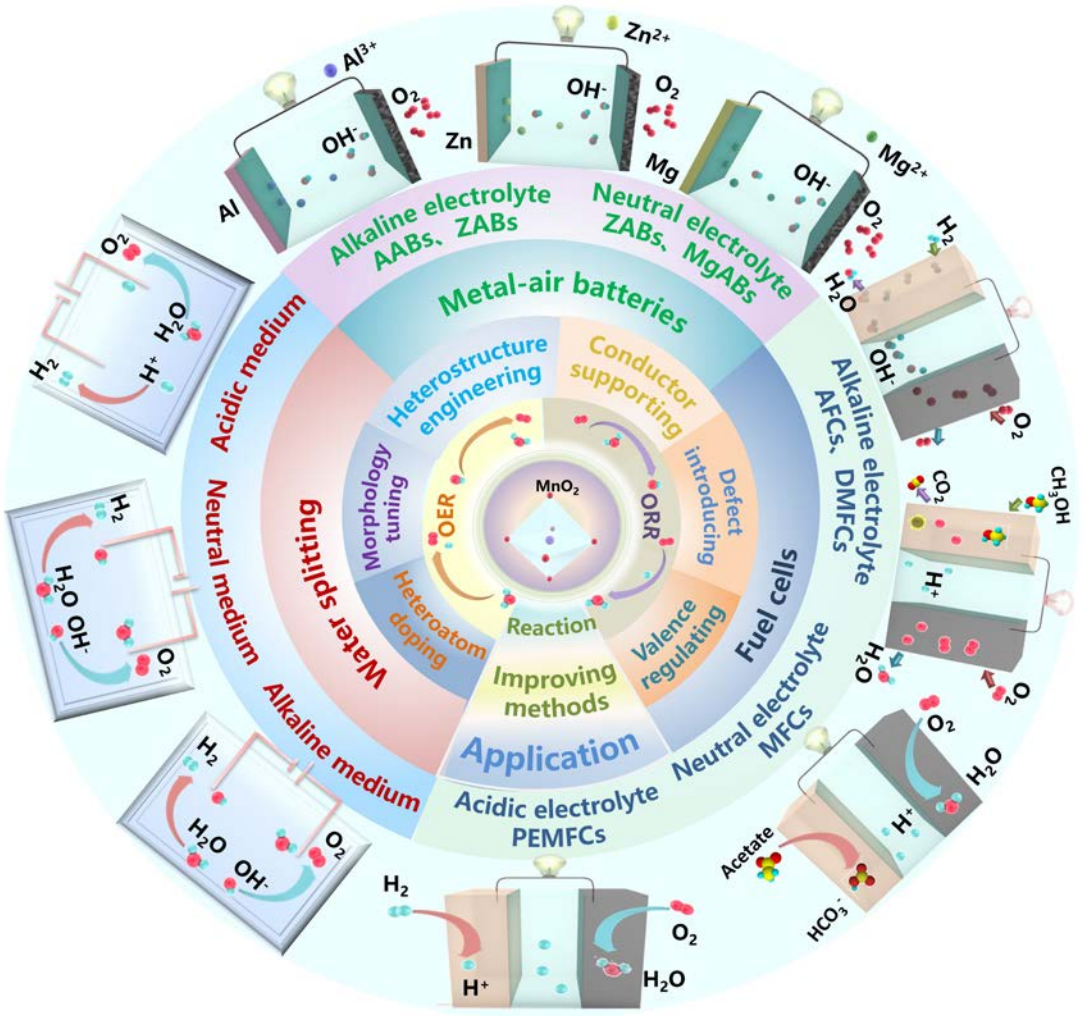

Fig. 5. The applications of MnO_2 in the various MABs, FCs and WSSs with the different electrolytes.

Figure 6

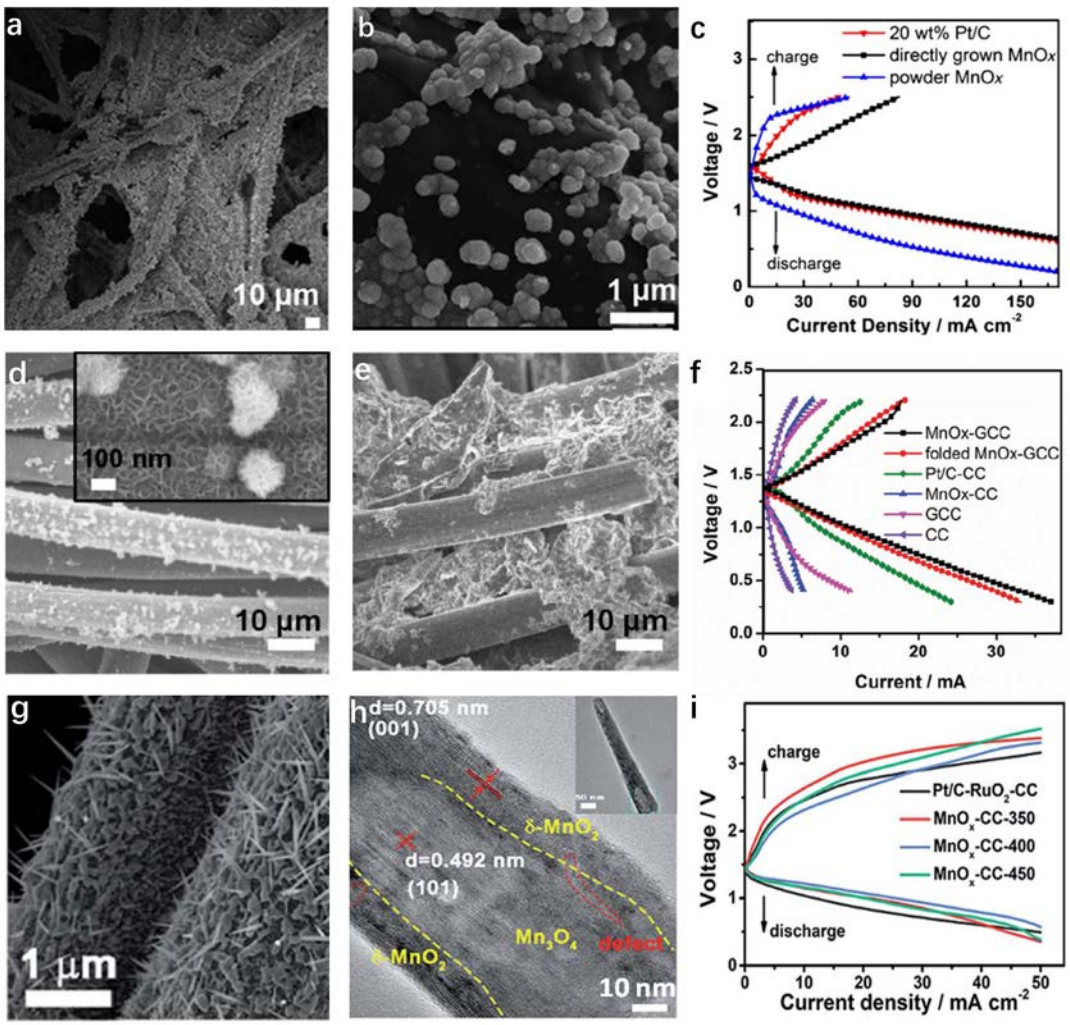

Fig. 6. a)~b) SEM images with different magnification of the manganese oxide grown on the carbon paper. c) Galvanodynamic charge and discharge polarization curves of ZAB with MnO_2 directly grown on the carbon paper. Reproduced with permission [135]. Copyright 2015, John Wiley and Sons. d)~e) SEM images of MnO_x grown on carbon cloth (MnO_x-CC) and graphene-coated on treated carbon cloth (GCC). f) Galvanodynamic discharge and charge polarization curves of ZAB with various carbon cloth-based air cathodes. Reproduced with permission [136]. Copyright 2017, John Wiley and Sons. g) SEM images of MnO_x grown on carbon cloth and subsequently

annealed at 400 ^{o}C for 1 h. h) HR-TEM images of MnO_x-CC-400. i) Galvanodynamic charge and discharge polarization curves of the ZAB with air cathodes of Pt/C-RuO_2-CC and MnO_x-CC samples. Reproduced with permission [137]. Copyright 2019, Royal Society of Chemistry.

Figure 7

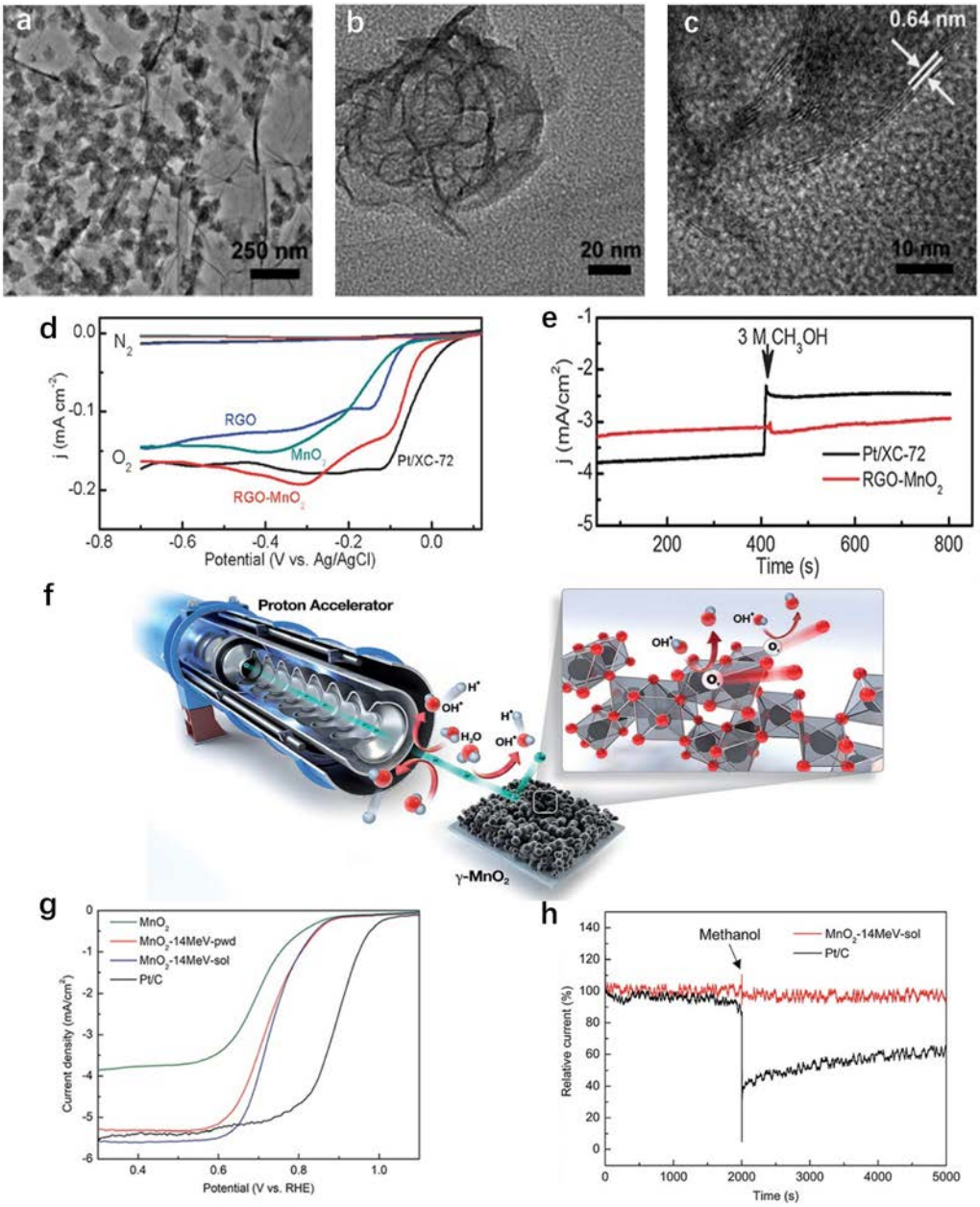

Fig. 7. a) SEM image and b)~c) TEM images of RGO-MnO_2 at various magnifications. d) Linear sweep voltammogram (LSV) curves of RGO-MnO_2 in nitrogen- and oxygen-saturated 0.1 M KOH at a scan rate of 0.5 mV s^{-1}. e) Current density-time chronoamperometric responses of Pt/XC-72 and RGO-MnO_2 electrodes at -0.3 V in oxygen-saturated 0.1M KOH. Rotating speed, 2000 rpm. The arrow indicates the addition of methanol into the electrochemical cell. Reproduced with permission [183].

Copyright 2013, Royal Society of Chemistry. f) Schematic illustration of the preparation of oxygen-deficient MnO_2 nanoparticles by proton beam irradiation. g) LSVs of MnO_2 prepared under 14 MeV proton irradiation and different experimental conditions in O_2-saturated 0.1 M KOH at 1600 rpm with a sweep rate of 5 mV s^{-1}. h) Methanol-crossover tests performed by adding methanol into the electrolyte at 2000 s. All measurements were performed at applied voltage of 0.6 V vs. RHE. Reproduced with permission [189]. Copyright 2019, Royal Society of Chemistry.

Figure 8

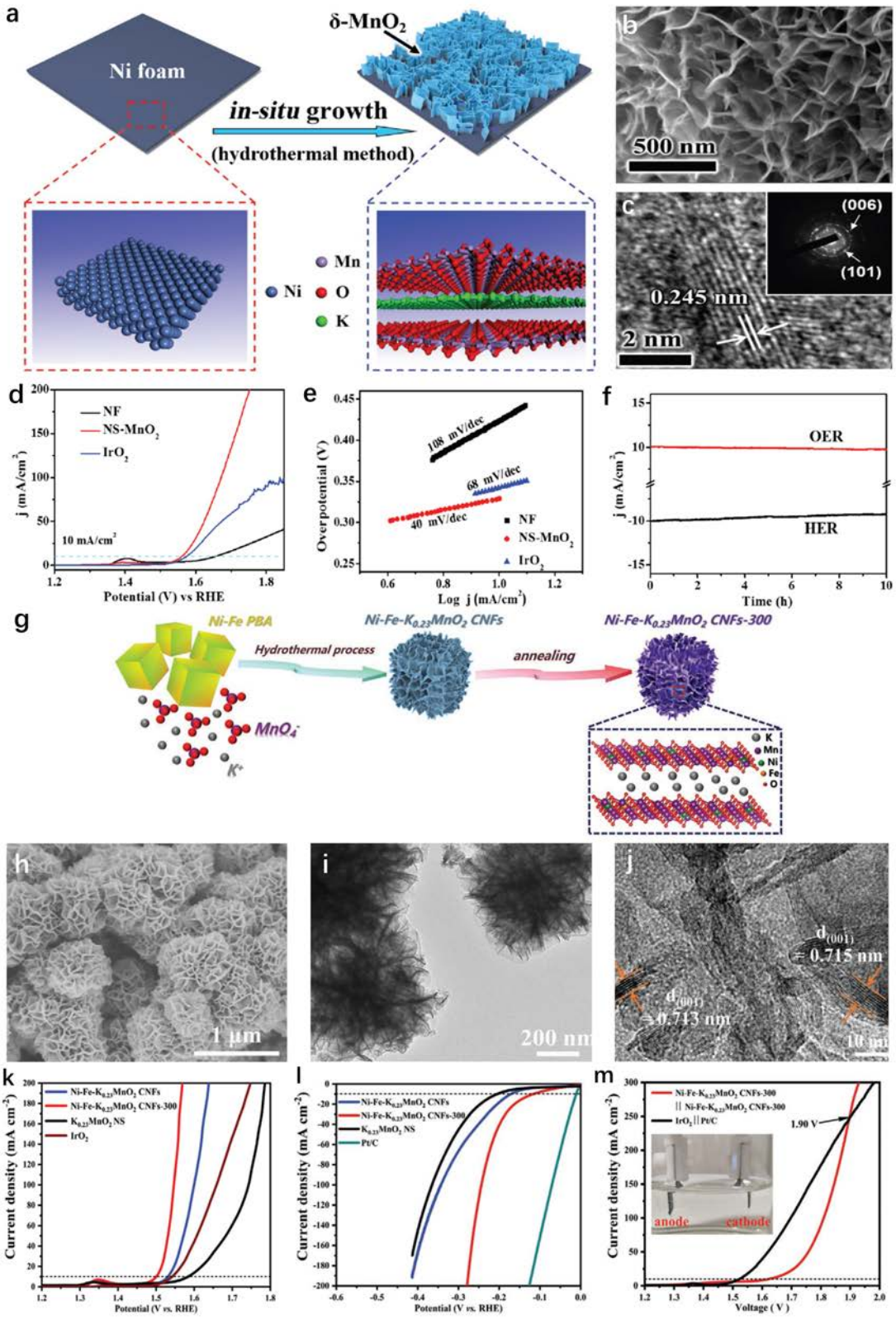

Fig. 8. a) Schematic showing the *in situ* growth of ultrathin δ-MnO_2 nanosheets on an Ni foam (NS-MnO_2). b) SEM image of NS-MnO_2. c) HRTEM image of δ-MnO_2

nanosheets (the inset shows the SAED pattern). d) Linear sweep voltammetry (LSV) curves for OER at a scan rate of 5 mV s^{-1} in 1 M KOH. e) Tafel plots for OER in 1 M KOH. f) Current density versus time (I-t) curves of HER and OER for NS-MnO_2. Reproduced with permission [89]. Copyright 2017, John Wiley and Sons. g) Schematic illustration of the synthetic process of Ni-Fe-K0.23MnO_2 CNFs-300. h) FESEM, i) TEM and j) HRTEM images of Ni-Fe-$K_{0.23}MnO_2$ CNFs-300. LSV curves of Ni-Fe-$K_{0.23}MnO_2$ CNFs-300 toward OER k) and HER l). m) Polarization curves of the Ni-Fe-$K_{0.23}MnO_2$ CNFs-300||Ni-Fe-$K_{0.23}MnO_2$ CNFs-300 cell for overall water splitting. Reproduced with permission [75]. Copyright 2020, John Wiley and Sons.